C/EBPβ-mediated PARP1 Suppression Drives Tumor Progression of Aneuploid Cells

Pan Cheng[1,2,4], Angela Mermerian-Baghdassarian[1,2], Yufeng Wang[1,2], Ze Chen[1,2], Helberth M. Quysbertf[1,2] , Joseph C. Mays[1,2], Xin Zhao[1,2], Lizabeth Katsnelson[1,2], Sally Mei[1,2], Rohini Shrivastava[1,2], Mirna Bulatovic[3], Jiehui Deng[2], Kwok-Kin Wong[2], Thomas M. Norman[4] and Teresa Davoli[1,2,5]

[1] Institute for Systems Genetics and Department of Biochemistry and Molecular Pharmacology, New York University School of Medicine, New York, NY, USA
[2] Division of Hematology & Medical Oncology, Laura and Isaac Perlmutter Cancer Center, New York University Langone Medical Center, New York, NY, USA
[3] Loxo Oncology at Lilly, Alexandria Center for Life Science, New York, NY, USA.
[4] Sloan Kettering Institute, New York, NY, USA
[5] Lead Contact and Correspondence: Pan Cheng (pan.cheng.phd@gmail.com), Teresa Davoli (teresa.davoli@nyulangone.org)

Highlights

- Aneuploidy universally confers resistance to oxidative stress independent of p53 status, karyotype and cell lineage through inhibition of PARP1 expression and activity
- Suppressed PARP1 enhances metastatic potential, while PARP1 restoration suppresses metastatic spread, revealing a novel mechanism linking aneuploidy to cancer progression.
- PARP1 suppression compromises DNA damage repair and cell death to multiple genotoxic stressors, including reactive oxygen species, alkylating agents, and UV radiation.
- A genome-wide CRISPR screen and a CRISPRa screen identifies CEBPB as the critical transcription factor mediating PARP1 regulation and ROS resistance.
- Nuclear CEBPB increases significantly after aneuplodization in experimental systems and in scRNAseq of primary human cancer patients.

Summary

Aneuploidy—defined as gains and losses of chromosomes—is frequently observed in cancer and has been implicated in promoting tumor progression and metastasis. However, the molecular mechanisms underlying this phenomenon remain poorly understood. By generating new *in vitro* and *in vivo* models of aneuploidy, we found that aneuploidy confers remarkable resistance to reactive oxygen species (ROS)-mediated cell death. This is a general consequence of aneuploidy, independent of the specific chromosomes gained or lost. Mechanistically, aneuploidy-induced resistance to cell death results from suppressed Poly(ADP-Ribose) Polymerase 1 (PARP1) in aneuploid cells, which inhibits PARP1-mediated cell death after ROS (parthanatos). We validated aneuploidy-associated PARP1 suppression across 15 cell models and human tumors, with pronounced effects in metastatic tumors. Importantly, decreased PARP1 levels in aneuploid cells promote tumor metastasis and vice versa. Through genome-wide CRISPR screen, a focused CRISPRa screen and functional validation, we identified the transcription factor CCAAT/enhancer-binding protein beta (CEBPB) as a critical mediator of PARP1 downregulation and ROS resistance in aneuploid cells. Furthermore, we found lysosomal dysfunction as the upstream mediator of CEBPB activation in aneuploid cells. We propose that during tumorigenesis, aneuploidy-driven CEBPB activation promotes PARP1 suppression fostering ROS resistance and cancer progression.

Introduction

Aneuploidy, a hallmark of cancer[1], correlates with tumor progression, poor survival, and therapeutic resistance[2–4]. The role of aneuploidy in cancer, however, remains incompletely understood. One prevailing model proposes that aneuploidy promotes tumor-associated phenotypes by altering the dosage of oncogenes and tumor suppressors located on aneuploid chromosomes (**chromosome-specific effects**)[5,6]. The role of the aneuploid state itself (**general effects**) in promoting tumorigenesis, independent of specific chromosomal changes, is more controversial. Aneuploid cells show fitness disadvantages likely due to defects in DNA replication and proteostasis[7,8], yet resist certain chemotherapies through increased genomic instability and karyotype heterogeneity or through other mechanisms[9,10]. Whether certain general effects of aneuploidy can promote other cancer-associated phenotypes remains unclear[11–13]. A better understanding of how aneuploidy impacts tumor formation and progression could contribute to the development of effective therapies and response biomarkers.

ROS are a double-edged sword in cancer. At low levels, ROS contribute to tumorigenesis and cancer development by promoting mutations, genomic instability, cell proliferation, survival, angiogenesis, and metastasis. Conversely, excessive ROS during tumor progression or anti-cancer therapy can damage DNA, proteins, and lipids, triggering cell death[14,15]. It has been recently shown

that oxidative stress in circulating cancer cells inhibits metastasis formation[16–18]. Therefore, cancer cells tend to enhance their ROS buffering capacity to reduce cell damage, or decrease their sensitivity to ROS-induced cell death, particularly during advanced tumor progression[16]. Interestingly, aneuploidy levels increase with tumor progression and metastasis[2,19]. However, whether a functional relationship between aneuploidy and ROS sensitivity exists and its implications for cancer progression has not been investigated.

Oxidative stress primarily induces DNA single-strand breaks (SSBs), resulting from oxidized phosphate-deoxyribose backbone fragmentation or base excision repair (BER) of oxidized bases[20]. PARP1 rapidly senses SSBs, transfers ADP-ribosyl moieties from nicotinamide-adenine-dinucleotide (NAD+) to various proteins, and facilitates the accumulation and stabilization of repair components at SSB sites[21]. Beyond DNA repair and genome integrity maintenance, PARP1 mediates a ROS-induced cell death mechanism termed parthanatos[22]. In this process, excessive oxidative DNA damage hyperactivates PARP1, depleting the cell of the essential NAD+ and adenosine triphosphate (ATP)[23] and triggering nuclear translocation of mitochondrial apoptosis-inducing factor (AIF)[24], ultimately leading to cell death. Parthanatos is critical in pathophysiological processes involving cellular stress and excessive DNA damage[22,25], such as ischemia–when a part of the body does not receive enough blood. During cerebral ischemia PARP1-mediated parthanatos causes neuronal cell death, which PARP1 inhibition can mitigate[26]. However, the role of parthanatos in cancer is much less well understood[27].

By studying parthanatos in the context of cancer, we observed PARP1 suppression in aneuploid cells, which enhances resistance to ROS-induced cell death while delaying DNA damage repair. This creates a 'perfect storm' benefiting cancer cells where death resistance is coupled with compromised DNA repair. Consistently, PARP1 modulation affects metastatic potential in both diploid and aneuploid cancer cells, aligning with the established role of ROS resistance in metastatic spread. Finally, a genome-wide CRISPR screen identified lysosomal gene inhibition as a mechanism suppressing PARP1 levels. We found that lysosomal dysfunction, a common feature of aneuploidy[28,29], activates transcription factor CEBPB, consequently suppressing PARP1 expression and rendering aneuploid cells survival advantages under oxidative stress.

Results

Identifying cellular stress resisted by aneuploid cells

To screen for possible benefits conferred by aneuploidy and relevant to cancer progression, we developed isogenic models of aneuploidy. We utilized a model of **acute aneuploidy** recapitulating short-term effects of aneuploidy, independent of specific chromosome alterations (**Fig. 1A**). In this model, immortalized human colon epithelial cells (hCECs) with wild-type TP53 (TP53WT) or TP53 knockout (TP53KO) were treated with MPS1 inhibitors (reversine or AZ3146; MPS1i) for 24-30 hours to induce non-specific chromosome missegregation[28], followed by a 3-day release.

Aneuploidy was confirmed by altered DNA content compared to DMSO-treated controls (**Fig. 1B**). Karyotypes inferred from single-cell RNA sequencing (see **Methods**) demonstrated that all chromosomes in MPS1i-treated TP53KO hCECs were gained or lost at similar rates without strong chromosome-specific preferences (**Fig. S1A**). On average, each chromosome arm was gained or lost in 25% of MPS1i-treated cells (±5% standard deviation (SD)) (**Fig. S1A**, **Table 1A**).

We next compared resistance to various cellular stresses between diploid and aneuploid TP53WT hCECs (DMSO versus MPS1i) (**Fig. 1C**, **Fig. S1B**). GFP-labeled diploid and unlabeled aneuploid hCECs were treated with drugs inducing various cellular stresses or disrupting specific cancer-associated genes. Treatments induced oxidative stress, proteostasis stress (by inhibiting lysosomes, proteasomes, chaperones, or protein folding in the endoplasmic reticulum), energy stress (by inhibiting mitochondria), DNA damage, and metabolic stress (by inhibiting glycolysis or cystine-glutamate transport). Additionally, inhibitors of RAC1, CDKN1A, IKBKB, and MAPKs, were included (**Fig. 1C, Fig. S1B, Table 1B**). Remarkably, compared to diploid ones, aneuploid cells were much more resistant to oxidative stress caused by hydrogen peroxide (H_2O_2) in a concentration-dependent manner (**Fig. 1C, Fig. S1B).** These findings indicate that aneuploid cells are more resistant than diploid cells to oxidative stress, a major barrier to cancer metastatic progression[16–18]. We further validated aneuploidy-associated resistance to oxidative stress using different aneuploidy models and ROS inducers (see below).

Aneuploidy confers oxidative stress resistance independent of TP53 status, altered chromosomes, or cell lineage

We next determined whether enhanced oxidative stress resistance in aneuploid cells depends on TP53 status, cell lineage, or cell cycle stage. Regardless of TP53 status (wild type or knockout), MPS1i-induced aneuploid hCECs displayed significantly higher viability after H_2O_2 treatment compared to DMSO-treated diploid controls (~55% vs 0% relative viability, **Fig. 1D-E**). To assess MPS1i off-target effects, hCECs were treated with MPS1i (or DMSO) under high confluency conditions where cell division and aneuploidy formation were suppressed, but potential MPS1i off-target effects unrelated to aneuploidy remained (**Fig. S1C)**. These MPS1i-treated non-aneuploid hCECs exhibited increased ROS-induced cell death compared to controls (30%-50% vs 14%) (**Fig. S1C**). This observation, along with similar results from different MPS1i, suggests that ROS resistance in MPS1i-treated cells depends on aneuploidy. Next, we subjected various cells to MPS1i treatment, including non-cancerous human cells (retinal pigment epithelial cells (RPE1, TP53KO), human pancreatic nestin-expressing cells (hPNE), and human mammary epithelial cells (hMEC)), and cancer cells (human colon cancer cell line DLD1 and a murine lung cancer cell line (see below)). We consistently observed enhanced resistance to oxidative stress in these aneuploid cells (**Fig. S1D-E**), indicating cell type-independent ROS resistance. Furthermore, we explored the impact of the cell cycle on oxidative stress resistance. Arresting hCECs at G1 phase (using palbociclib) or early S phase (using thymidine) augmented ROS resistance in both diploid and aneuploid cells by

146 20%-40%. However, arrested aneuploid cells maintained significantly higher resistance, with about
147 30% greater relative viability compared to diploid cells (**Fig. S1F**).
148 To validate these findings, we next generated a **chronic aneuploidy** model representing
149 longer-term effects during adaptive stages of aneuploidy[30]. Using reversine-treated TP53KO
150 hCECs, we generated 55 single cell-derived isogenic hCEC clones with varying aneuploidy levels,
151 assessed by whole-genome sequencing (**Fig. 1A, 1F**, **Table 1C**, see **Methods**). Two representative
152 near-diploid and four aneuploid clones (≥ 5 gains or losses of chromosomes or chromosome arms)
153 were selected to compare their oxidative stress resistance (**Fig. 1F**, **Fig. S1G**). Like the acute
154 aneuploidy model, the aneuploid clones showed enhanced resistance, with 20-40% higher relative
155 viability when exposed to 50 μM H_2O_2 (**Fig. 1G**). This resistance was independent of both their
156 attachment status (**Fig. S1H**) and the attachment surfaces (**Fig. S1I**).
157 Then we examined aneuploid clones of HCT116 (a human colon cancer cell line) and RPE1
158 generated through microcell-mediated chromosome transfer (MMCT)[31]. All aneuploid clones,
159 whether carrying an additional copy of chromosome 5 or chromosome 7, exhibited increased
160 resistance to oxidative stress compared to their near-diploid counterparts, with 45-65% higher
161 relative viability (**Fig. 1H**).
162 Next, we induced aneuploidy in near-diploid mouse lung cancer cells derived from the KP
163 ($Kras^{G12D}$ and $Trp53^{-/-}$) lung adenocarcinoma model[32,33]. We adapted KaryoCreate (Karyotype
164 CRISPR Engineered Aneuploidy Technology), our recently described CRISPR-based strategy to
165 induce aneuploidy in human cells[34], for mouse cells by designing a sgRNA targeting minor satellite
166 regions on mouse centromeres (sgMinSat5) (**Fig. 1I**). When combined with the dCas9-AuroraB
167 fusion protein, this sgRNA induced a significant level of aneuploidy compared to a control sgRNA
168 targeting the Rosa26 locus (sgRosa26) (average chromosome count is 48±7 for sgRosa26 and
169 74±8 for sgMinSat5, **Fig. S1J**). Importantly, when we tested their sensitivity to ROS, we found that
170 the aneuploid mouse KP cells showed significantly enhanced resistance to oxidative stress (60%
171 higher) compared to the near-diploid control (**Fig. 1I**). Notably, unlike typical aneuploidy models
172 where aneuploid cells grow slower, aneuploidy induction did not impair the proliferation of KP cells
173 *in vitro* (**Fig. 1I**). This feature further suggests that ROS resistance in aneuploid cells is not caused
174 by cell cycle alterations.
175 Finally, we compared two near-diploid human colon cancer cell lines (HCT116 and DLD1)
176 with four high-aneuploidy colon cancer cell lines (HT29, SW403, SW948, and SK-CO-1) (**Table 1D**).
177 Consistently, the high-aneuploidy lines were more resistant to oxidative stress compared to the
178 near-diploid lines (40-110% higher viability, **Fig. 1J**, **Fig. S1K**).
179 We further validated the increased resistance of aneuploid cells using lower H_2O_2
180 concentrations over extended periods, assessing both proliferation and soft-agar colony formation
181 (**Fig. S1L-M**). Furthermore, we confirmed aneuploidy-induced ROS resistance using alternative
182 ROS inducers, supplementing culture medium with xanthine oxidase and xanthine to produce both
183 O_2^- (superoxide) and H_2O_2[35] or with tert-Butyl Hydroperoxide (**Fig. S1N** and data not shown).

Collectively, our data across multiple aneuploidy models provide robust evidence that aneuploidy renders cells resistant to oxidative stress, regardless of TP53 status, cell cycle, altered chromosomes, or cell lineage.

Aneuploidy-induced ROS resistance is not due to enhancement of cellular antioxidant defenses

The aneuploidy-induced oxidative stress resistance could result from heightened antioxidant defenses. The nuclear factor erythroid 2 p45-related factor 2 (NRF2) is the first-tier defense activated under oxidative stress[16]. Upon activation, cytosolic NRF2 is protected from degradation and translocates to the nucleus to initiate antioxidant gene transcription[36]. We examined NRF2 activation in cells with acute and chronic aneuploidy compared to diploid controls. No significant increase in NRF2 nuclear translocation (**Fig. S2A**) was observed in hCECs with acute aneuploidy compared to diploid controls, except for a slight increase in AZ3146-treated TP53KO hCECs, possibly due to aneuploidy-independent effects. The aneuploid hCEC clones even displayed slightly reduced NRF2 nuclear translocation compared to the near-diploid clones. Consistently, NRF2 knockout did not abolish the survival advantage of aneuploid hCECs relative to diploid controls under oxidative stress (**Fig. S2B**). Further investigation of key antioxidant genes, GPX1 and CAT, which are crucial for direct cellular H_2O_2 elimination, revealed that even after knockdown of these genes aneuploid cells remained more resistant to ROS than diploid ones (84.8% vs 12.7% average viability) (**Fig. S2C**). Collectively, these findings suggest that the increased oxidative stress resistance in aneuploid cells is not mediated by enhancement of cellular antioxidant defenses via NRF2 or its downstream antioxidant gene GPX1 and CAT.

We then compared ROS-induced cellular damage (DNA damage and lipid peroxidation) between diploid and aneuploid hCECs, using both acute and chronic aneuploidy models (**Fig. 2A**, **Fig. S2D-E**). The alkaline comet assay was used to assess DNA double-strand and single-strand breaks, revealing that H_2O_2 exposure induced a comparable level of DNA damage in diploid and aneuploid hCECs, with 50%-65% of DNA in the comet tail due to oxidative damage **(Fig. 2A, Fig. S2D**). This result was corroborated by the similar levels of phosphorylated histone H2AX (Ser132), a DNA damage marker, between diploid and aneuploid cells after H_2O_2 exposure (see **Fig. 3M**, **Fig. S3H-K**). We also examined H_2O_2-induced lipid peroxidation using the fluorescent indicator C11-BODIPY 581/591. H_2O_2 exposure resulted in similar lipid peroxidation levels in diploid and aneuploid hCECs, with a 60%-70% decrease in the emission fluorescence ratio (**Fig. S2E**). These findings indicate that the resistance to oxidative stress of aneuploid cells is not due to enhanced antioxidant defenses, as no reduction in oxidative DNA or lipid damage was observed in aneuploid cells compared to diploid cells following H_2O_2 exposure.

PARP1, a key mediator of ROS-induced cell death, is suppressed in aneuploid cells

We investigated whether aneuploid cells better resist ROS-induced cell death despite comparable levels of cellular damage. To determine the specific cell death pathway activated by oxidative stress, we pretreated hCECs with inhibitors of apoptosis (Z-VAD-FMK), necrosis (necrostatin-7), ferroptosis (ferrostatin-1), and PARP1-mediated parthanatos (olaparib). Strikingly, only olaparib significantly rescued H_2O_2-induced cell death (H_2O_2 reduced the proliferation of olaparib-treated hCECs by 40-50% without inducing cell death, **Fig. 2B-C**). This indicates that elevated oxidative stress triggers parthanatos in our cell model, which was further confirmed using a different cell type, hMEC (**Fig. S2F**)

PARP1, the molecular target of olaparib, is crucial in parthanatos: it senses DNA damage caused by ROS or other stimuli and subsequently initiates parthanatos by exhausting NAD+ and ATP or by triggering AIF nuclear translocation[23,24]. We observed a consistent ~40-50% decrease in PARP1 RNA levels in acutely aneuploid cells compared to diploid controls across multiple cell lines (**Fig. 2D**, **Table 2A-B**), suggesting that PARP1 downregulation in aneuploid cells is independent of their transformation state, TP53 status, or cell lineage. Protein-level PARP1 downregulation in acutely aneuploid cells was confirmed, showing a ~50-60% decrease across various cells (**Fig. 2E**), aligning with reports on reversine-treated RPE1 cells[28], glioma cells[37], and mouse embryos[38], while none of these studies focused on PARP1 or parthanatos. Furthermore, we probed for PARP1 activity and we observed reduced poly(ADP-ribose) (pADPr) synthesis in MPS1i-treated aneuploid cells after H_2O_2 exposure (**Fig. S2G**). Importantly, the PARP1 protein decline cannot be attributed to caspase-mediated cleavage [39], as it persisted with a pan-caspase inhibitor (**Fig. S2H**), consistent with prior observations in reversine-treated RPE1 cells[28]. Notably, it is important to highlight that PARP1 is haploinsufficient[40] and as demonstrated below (Fig. 3H), even a modest change in gene dosage can profoundly impact cell state and function.

In the isogenic hCEC clones, we also observed a negative correlation between aneuploidy degree (aneuploidy score, AS) and PARP1 expression at both RNA and protein levels (RNA: Spearman R = -0.58, p = 0.01; protein: Spearman R = -0.49, p = 0.05; **Fig. 2F-H**, **Table 2C-D**). Other aneuploidy models also supported our findings. Aneuploid clones of HCT116 and RPE1 cells generated by MMCT to carry additional copies of chromosome 3, 5, 12, or 21 exhibited reduced PARP1 expression (**Fig. 2I**, **Fig. S2I-J**), suggesting PARP1 downregulation is independent of specific altered chromosomes. Aneuploid mouse KP lung cancer cells, generated by KaryoCreate and resistant to ROS-induced cell death (**Fig. 1I**), also showed decreased PARP1 expression (**Fig. S2K**). Notably, we also observed a substantial decrease in PARP1 levels in the high-aneuploidy colon cancer cell lines compared to the near-diploid ones (see **Fig. 4A**). Taken together, these results suggest that PARP1 downregulation is a common feature in aneuploid cells, regardless of TP53 status, altered chromosomes, cell lineage, or cancerous state.

261 **PARP1 suppression reduces aneuploid cell sensitivity to PARP1-mediated cell death induced**
262 **by ROS, alkylating agents, or UV radiation**
263
264 While PARP1 is considered a pro-survival gene that senses DNA damage and promotes DNA
265 repair[21], its hyperactivation can trigger parthanatos, the most common form of regulated necrosis
266 induced by DNA damage[25,41]. This process is relevant in pathophysiological contexts such as
267 ischemia-related tissue damage [42], and potentially in cancer progression and treatment, which
268 often involve exposure to elevated levels of ROS, alkylating agents, or UV radiation. Given our
269 findings of PARP1 downregulation in aneuploid cells (**Fig. 2**), we hypothesized that this reduction
270 contributes to aneuploid cell resistance to ROS-induced (or more generally, PARP1-mediated) cell
271 death. To test this hypothesis, we modulated PARP1 expression through knockdown/knockout or
272 overexpression and assessed corresponding changes in cell sensitivity to H_2O_2, a proven activator
273 of PARP1-mediated cell death (**Fig. 2B-C, Fig. S2F**).
274 shRNA-mediated PARP1 knockdown conferred H_2O_2 resistance to near-diploid hCEC
275 clones, increasing their viability by 20-40% compared to a non-targeting shRNA (**Fig. 3A-B**).
276 CRISPR-mediated PARP1 knockout validated this protective effect (**Fig. S3E-F**). Conversely, PARP1
277 overexpression decreased H_2O_2 resistance in both acutely and chronically aneuploid hCECs,
278 reducing relative viability by 15-40% compared to empty vector controls (**Fig. 3C-F**). Notably, the
279 resistance induced by the shRNA targeting PARP1 3'-UTR was reversed by overexpressing shRNA-
280 resistant PARP1 cDNA (**Fig. 3G**). PARP1 overexpression in the highly-aneuploid colon cancer cell
281 line (HT29) also reduced H_2O_2 resistance (see **Fig. 4D-E**, **Fig. S4A**), while PARP1 knockdown in the
282 near-diploid colon cancer cell lines (HCT116 and DLD1) enhanced resistance (see **Fig. 4F-G**, **Fig.**
283 **S4B**), consistent with observations in non-cancerous hCECs. To test whether subtle changes in
284 PARP1 expression levels could affect H_2O_2 resistance, we constructed hCECs with a Tet-On system
285 for doxycycline-inducible PARP1 expression. Notably, we found that a 20% increase in PARP1
286 expression sufficiently reduced H_2O_2 resistance, decreasing relative viability by ~20% (**Fig. 3H**).
287 Although PARP1 overexpression significantly reduced H_2O_2 resistance in aneuploid hCECs,
288 it did not completely eliminate their higher resistance compared to diploid ones, particularly at low
289 H_2O_2 concentrations (**Fig. S3A**), indicating additional factors contribute to aneuploidy-associated
290 oxidative stress resistance. Therefore, we next turned to PARP1-associated factors that have been
291 shown to promote its function. One of the most prominent is Timeless Circadian Regulator
292 (TIMELESS), which physically interacts with PARP1 and promotes its recruitment to DNA damage
293 foci and subsequent activation[43]. We found TIMELESS expression was consistently decreased at
294 RNA levels in acutely aneuploid cells compared to diploid controls (**Fig. S3B**) and inversely
295 correlated with aneuploidy degree at RNA and protein levels in the chronic aneuploidy model (**Fig.**
296 **S3C**). We found that in the highly-resistant aneuploid clone A29, PARP1 overexpression only
297 reduced H_2O_2 resistance at the lethal concentration triggering parthanatos (**Fig. 3F**, **Fig. 3I**), but not
298 at the non-lethal concentration that only decreased cell proliferation (**Fig. S3A**, **Fig. S3D**). At both
299 the lethal and the low non-lethal H_2O_2 concentration, co-overexpression of PARP1 and TIMELESS

300 in A29 reduced H_2O_2 resistance more than overexpression of either gene alone (**Fig. 3I**, **Fig S3D**),
301 suggesting TIMELESS downregulation may suppress PARP1 hyperactivation under oxidative
302 stress in aneuploid cells.
303 We next investigated the role of other parthanatos-relevant genes in aneuploid cell
304 resistance to ROS-induced cell death. While PARP1 catalyzes 85-95% of total cellular pADPr in
305 response to DNA damage, PARP2, though less abundant, has a similar function and is also targeted
306 by olaparib[44]. However, PARP2 knockout did not protect hCECs from H_2O_2 (P = 0.22; **Fig. S3E**),
307 excluding its involvement in aneuploidy resistance to parthanatos. Macrophage migration
308 inhibitory factor (MIF), a late-stage parthanatos nuclease, cleaves genomic DNA[45]. MIF knockout
309 partially protected hCECs from H_2O_2, but less effectively than PARP1 knockout (relative viability
310 increased by 20%-38% for PARP1 knockout vs 7%-14% for MIF knockout, **Fig. S3F**).
311 Furthermore, we investigated whether mitigating NAD+ depletion, a typical consequence of
312 PARP1 hyperactivation[22,46], inhibits cell death after H_2O_2 treatment. Supplementation with
313 nicotinamide mononucleotide (NMN, a NAD+ precursor) increased the viability of H_2O_2-treated
314 hCEC clones by 20% to 40% (**Fig. 3J**). Finally, we applied agents different than H_2O_2-induced ROS
315 to induce DNA damage and PARP1 activation: N-methyl-N'-nitro-N-nitrosoguanidine (MNNG), a
316 common alkylating agent, and UV radiation, both known to trigger PARP1-mediated cell death[41].
317 Remarkably, aneuploid hCEC clones were more resistant to these stimuli than the near-diploid
318 clones in a PARP1-dependent manner (**Fig. 3K-L**). Collectively, these results suggest that PARP1
319 downregulation confers resistance to PARP1-mediated cell death in aneuploid cells, whether
320 induced by ROS, alkylating agents, or UV radiation.
321
322
323 **PARP1-mediated DNA damage repair is impaired in aneuploid cells**
324
325 Beyond cell death, we investigated the impact of PARP1 downregulation on DNA damage repair in
326 aneuploid cells, given the crucial role of PARP1 in this process[21]. We transiently exposed isogenic
327 near-diploid and aneuploid hCEC clones to various genotoxic insults and collected cells before
328 stimulation (control) and at different time points after stimulation (RX: Release X hours after
329 stimulation), without observed cell death before collection. DNA damage was assessed by
330 immunofluorescence, measuring Ser-139 phosphorylation of the histone variant H2AX (γH2AX), a
331 molecular marker of DNA damage response induced shortly after DNA damage and decreases
332 during DNA repair[47] (**Fig. S3G**). Seven genotoxic agents with different DNA damaging mechanisms
333 were tested: H_2O_2 (oxidative damage), MNNG (base alkylation), camptothecin (topoisomerase I
334 inhibition), etoposide (topoisomerase II inhibition), pyridostatin (C-quadruplex stabilization),
335 doxorubicin (DNA intercalation), and bleomycin (DNA synthesis inhibition). We found that repair of
336 H_2O_2- and MNNG-induced DNA damage was significantly slower in aneuploid clones compared to
337 diploid cells given both the statistical significance and effect size (see **Methods**), while repair of
338 DNA damage from other genotoxic agents was not aneuploidy-dependent (**Fig. S3H-I**). After six

339 hours of recovery from H_2O_2 treatment, median γH2AX intensity decreased by approximately 40%
340 in the near-diploid clones but only by 15% (A29) or increased by 20% (A20) in the aneuploid clones
341 (**Fig. S3H-I**). Similarly, MNNG-induced DNA damage repair was less efficient in aneuploid clones,
342 with median γH2AX intensity increasing by 54%-103% compared to -16% to 19% in the near-diploid
343 clones after six hours of recovery (**Fig. S3H-I**). This observation may relate to the heavy reliance on
344 PARP1 for repairing H_2O_2- and MNNG-induced DNA damage, while other agents involve multiple,
345 less PARP1-dependent repair pathways [47] (see **Discussion**). The suppressive effect of PARP1
346 downregulation on oxidative DNA damage repair was further validated by analyzing PARP1-
347 overexpressing cells. PARP1 overexpression promoted oxidative DNA damage repair in both acute
348 and chronic aneuploidy models (**Fig. 3M, Fig. S3J**, **Table 3**). Importantly, we excluded the
349 possibility that γH2AX dynamics result from altered H2AX protein levels, as γH2AX changes were
350 independent of total H2AX level fluctuations (**Fig. S3K**). Additionally, γH2AX decrease in the near-
351 diploid clones 6 hours after H_2O_2 exposure is likely unrelated to programmed cell death, as previous
352 studies showed PARP1-mediated cell death (parthanatos) does not cause collateral γH2AX
353 decrease[48]. Taken together, our data indicate that aneuploid cells, besides surviving H_2O_2 or MNNG-
354 induced cell death, may be more prone to accumulating DNA damage due to suppressed PARP1-
355 mediated DNA repair. The combination of death resistance and DNA damage accumulation may
356 collectively promote tumorigenesis and cancer evolution (see **Discussion**).
357
358 **PARP1 downregulation promotes tumor progression of aneuploid cancer cells**
359
360 Given our observation of decreased PARP1 expression across different aneuploidy models (**Fig. 2**),
361 we asked whether the same was true in human cancer cell lines and in primary tumors with varying
362 aneuploidy levels. Western blot analysis of four high-aneuploidy (HT29, SW948, SK-CO-1, SW403)
363 and two near-diploid (HCT116, DLD1) colon cancer cell lines revealed reduced PARP1 expression
364 in high-aneuploidy lines (**Fig. 4A**, **Table 1D**). Analysis of pan-cancer cell lines in the CCLE dataset,
365 evenly grouped into three aneuploidy levels, revealed significant aneuploidy-dependent declines in
366 PARP1 expression at both RNA and protein levels (RNA mean log2FC = -0.3, protein mean log2FC
367 = -0.25, high vs low aneuploidy, $p<0.0001$, $p=0.0013$; **Fig. 4B**). This trend extended to colorectal
368 cancer cell lines from the CCLE dataset, which showed decreased PARP1 expression with
369 increasing aneuploidy (RNA median log2FC = -0.27, protein median log2FC = -0.45, high vs low
370 aneuploidy, p = 0.05, 0.04; **Fig. 4C**). Consistent with our findings that PARP1 expression inversely
371 correlates with cell resistance to ROS-induced death (**Fig. 3**), PARP1 overexpression attenuated
372 ROS resistance in high-aneuploidy colon cancer cells (**Fig. 4D-E**, **Fig. S4A**), while PARP1
373 knockdown enhanced ROS resistance in near-diploid colon cancer cells (**Fig. 4F-G**, **Fig. S4B**). These
374 results further support our model, indicating that PARP1 expression levels also critically determine
375 cancer cell sensitivity to ROS-induced cell death (**Fig. 3**).
376 Since metastasis requires cancer cells to withstand high oxidative stress during migration
377 and colonization[16–18,49], we investigated whether PARP1 levels influence dissemination potential of

378 diploid and aneuploid cancer cells. To this end, cancer cells expressing luciferase were
379 intravenously injected into mice, and signal intensity and distribution were monitored via
380 bioluminescence imaging. We found PARP1 suppression enhanced dissemination potential of
381 near-diploid human colon cancer cells in immunodeficient mice (**Fig. 4H-I**). DLD1 and HCT116 cells
382 transduced with PARP1 shRNA exhibited significantly increased bioluminescence signals after four
383 or six weeks post-injection compared to controls with non-targeting shRNA, respectively (n=5 mice
384 for each group; $p = 0.007$ for DLD1 at week 4, $p = 0.03$ for HCT116 at week 6; **Fig. 4H-I**). Importantly,
385 PARP1 knockdown did not affect cell proliferation *in vitro* (**Fig. S4C**). Furthermore, we assessed the
386 impact of PARP1 levels on murine aneuploid cancer cells in immune-intact mice. We intravenously
387 injected aneuploid mouse KP lung cancer cells (transduced with sgMinSat5; **Fig. 1I**) into B6 Albino
388 mice. Consistently, mouse PARP1 overexpression decreased their tumor dissemination (luciferase
389 expressing cells intravenously injected) without affecting in vitro proliferation, with 40% of mice
390 developing tumors in the PARP1 OE group compared to 80% in empty vector controls (**Fig. 4J**, **Fig.
391 S4D**). These data indicate that PARP1 downregulation may promote metastasis of aneuploid
392 cancer cells in both immune-deficient and immune-intact mice.
393 We next examined PARP1 levels in human primary tumors to determine whether it changes
394 with tumor stage and patient survival. In line with our *in vivo* findings, among The Cancer Genome
395 Atlas (TCGA) colorectal adenocarcinoma (COREAD) patients, PARP1 expression was lower in
396 tumors with high aneuploidy compared to those with low aneuploidy (**Fig. 4K**, **Table 4**), and lower
397 PARP1 expression was associated with shorter survival (**Fig. 4L**, **Table 4**). This aligns with previous
398 research showing that late-stage COREAD tumors, typically characterized by higher aneuploidy
399 degrees[50], exhibit lower PARP1 expression and activity compared to early-stage tumors[51].
400 Furthermore, we compared PARP1 levels in primary and metastatic COREAD samples. In 15 paired
401 tumors[52], 73.3% of metastases showed decreased PARP1 expression compared to their primary
402 tumors ($p < 0.01$; **Fig. 4M**). Analysis of another dataset containing unpaired tumors revealed
403 consistent decreased PARP1 levels in metastasis compared to primary tumors in both discovery
404 (333 primary tumors, 184 metastases) and validation (545 primary tumors, 72 metastases)
405 cohorts[52] (**Fig. 4N**, **Fig. S4E**). Altogether, these findings from our *in vivo* experimental models and
406 our analyses of human tumor samples support a role for PARP1 downregulation in promoting
407 metastasis.
408
409
410 **Identifying regulators of PARP1 expression through genome-wide CRISPR screen**
411
412 Next, we investigated the mechanisms of PARP1 regulation and specifically its downregulation in
413 aneuploid cells. We conducted fluorescence-activated cell sorting (FACS)-based genome-wide
414 CRISPR screens to identify genes modulating PARP1 expression, using the endogenous PARP1
415 levels as the readout (**Fig. 5A** and **Fig. S5A**). For each screen, 60 million hCEC were infected with a
416 lentiviral sgRNA library targeting 19,026 protein-coding human genes. After selection and

417 expansion, cells were fixed, immunostained for PARP1, and sorted based on its expression levels.
418 We validated the FACS-based PARP1 readout using cells with varied PARP1 expression levels (**Fig.**
419 **5B**).
420 SgRNAs were sequenced from PARP1-low, PARP1-high, and unsorted cells. We anticipated
421 sgRNAs against putative PARP1 activators to be enriched in PARP1-low cells compared to the
422 unsorted cells, while sgRNAs targeting putative PARP1 suppressors in PARP1-high cells. MAGeCK
423 algorithm calculated enrichment scores for each gene, revealing a negative correlation between
424 gene enrichment in PARP1-low and PARP1-high populations ($p < 2e-16$, rho = -0.22, **Fig. 5C**, **Table**
425 **5A**). This indicated exclusive enrichment of genes in populations with different PARP1 levels.
426 Importantly, sgRNAs targeting PARP1 were enriched in the PARP1-low population and depleted
427 from the PARP1-high population (MAGeCK beta values = 0.48 and -1.55, p-value = 0.003 and 0 for
428 PARP1-low and PARP1-high populations, respectively; **Fig. 5C-D**), confirming the screen's success.
429 The screen identified 269 PARP1 activators and 155 suppressors (FDR < 0.1, MAGeCK beta
430 value > 0.5, **Table 5B**). QIAGEN Ingenuity Pathway Analysis (IPA) revealed PARP1 activators were
431 enriched in pathways related to phagosome maturation (p-value = 1.7e-17), tRNA charging (p-value
432 = 3.7e-14) among others. PARP1 suppressors were predominantly associated with RNA
433 polymerase I complex assembly (p-value = 1.2e-6) (**Fig. 5E**, **Fig. S5B**, **Table 5C-D**).
434 To identify genes and pathways that may mediate PARP1 downregulation in aneuploid
435 cells, we then examined how the expression of these PARP1 activators and suppressors changes
436 in aneuploid compared to diploid ones (**Fig. S5C**). Aneuploidy-associated PARP1 regulators were
437 identified by finding PARP1 activators that are downregulated in aneuploid cells and PARP1
438 suppressors that are upregulated in aneuploid cells (**Fig. S5D, Table 5E**). Phagosome maturation
439 pathway (p-value = 6.4e-03), consisting of many lysosome genes, enriched in these aneuploidy-
440 associated PARP1 regulators (**Fig. S5E**, **Table 5F**), suggesting that lysosomal dysregulation in
441 aneuploid cells may cause PARP1 downregulation.
442
443
444 **Lysosomal stress is a potential mediator of PARP1 downregulation in aneuploid cells**
445
446 Lysosomal stress is characteristic of aneuploidy[28], with aneuploid cells showing transcriptional
447 profiles similar to those treated with the lysosomal V-ATPase inhibitor bafilomycin A1 (Baf A1)[29].
448 Our screen showed that knockout of lysosomal genes resulted in PARP1 downregulation
449 (phagosome maturation pathway in **Fig. 5E** and **Fig. S5E**, individual lysosomal V-ATPase genes in
450 **Fig. S5F**). Thus, we hypothesized that aneuploidy-associated lysosomal stress induces PARP1
451 downregulation and tested this hypothesis. First, principal component analysis (PCA) of RNASeq
452 data from 8 near-diploid and 11 aneuploid (≥ 5 gains or losses of chromosomes or chromosome
453 arms) hCEC clones revealed that lysosomal, but not proteasomal, genes differentiated near-diploid
454 from aneuploid cells (p-value < 0.0001 and = 0.173, respectively, **Fig. 5F**), indicating a distinct
455 lysosomal gene expression profile in aneuploid cells. Second, expression changes of these

456 lysosomal genes and the whole transcriptome in aneuploid cells correlated with those in cells
457 treated with the lysosome inhibitor Baf A1 (Spearman p-value < 0.05, **Fig. 5G-H**, **Fig. S5G**,
458 suggesting that aneuploid cells experience Baf A1-like lysosomal stress. Third, analysis of four
459 published datasets[28,53–55] revealed that lysosome inhibitor Baf A1 treatment reduced PARP1
460 expression in various cell lines (Log2FC: -0.350 to -1.112, **Fig. 5I**); this reduction in PARP1 after Baf
461 A1 treatment was further validated by western blot analysis in our hCECs (**Fig. S5H**). Conversely,
462 proteasome inhibition[28,56–58] did not affect PARP1 expression (p-value > 0.05, **Fig. S5I**), highlighting
463 the specificity of lysosome inhibition on PARP1 downregulation. Finally, we examined whether
464 lysosome inhibition enhances ROS resistance. Baf A1 treatment protected hCECs (both TP53WT
465 and TP53KO) from H_2O_2-induced cell death (91-107% increase in relative viability, **Fig. 5J**). This
466 lysosome dysfunction-induced resistance to oxidative stress was completely eliminated by PARP1
467 overexpression (p-value < 0.0001, **Fig. 5K**). These results suggest that lysosomal stress promotes
468 PARP1 downregulation and corresponding oxidative stress resistance in aneuploid cells.
469
470
471 **CEBPB is an aneuploidy-induced transcription factor that suppresses PARP1 suppression**
472
473 Decreased PARP1 RNA in aneuploid cells and cells with lysosomal dysfunction (**Fig. 2D**, **2F**, **5H**)
474 suggested that these conditions may alter PARP1 transcription. Thus, we set out to identify
475 transcription Factors (TFs) that may be responsible for PARP1 transcriptional dysregulation in
476 these settings (aneuploid and lysosome-dysfunction). To this aim, we integrated our PARP1
477 CRISPR screen results (**Fig. 5C**) with TF databases[59–61] to identify PARP1-influencing TFs (**Fig. 6A**).
478 Additionally, we examined expression changes of these TFs in aneuploid and lysosome-
479 dysfunction cells, looking for downregulation of TFs promoting PARP1 expression and upregulation
480 of those suppressing PARP1 expression (**Fig. 6A**). These analyses identified CEBPB as a potential
481 suppressive TF of PARP1, with consistently increased expression in various aneuploid and
482 lysosome-dysfunction cell models (p<0.05, **Fig. 6B-F**). CEBPB ChIP-Seq[62] confirmed its binding
483 near the PARP1 transcription start site upon activation by dexamethasone (CEBPB activator)
484 (reproducible peaks identified by the Irreproducibility Discovery Rate algorithm, **Fig. 6B**).
485 Strikingly, IF analysis of hCEC cells showed a significant **increase in nuclear CEBPB signal**
486 **in aneuploid cells compared to near-diploid cells.** This increase was observed in both the chronic
487 aneuploidy model (30-35% higher mean CEBPB intensity in A20 and A29 than D23 and D29,
488 p<0.001) and acute aneuploidy models (50% higher mean CEBPB intensity in Reversine-treated
489 versus DMSO-treated cells, p<0.001) (**Fig. 6D**). CEBPB upregulation was consistently confirmed in
490 our transcriptomic and proteomic dataset in both acute aneuploidy models (p < 0.01 for RNA, p <
491 0.05 or p = 0.07 for protein; **Fig. 6C**) and chronic aneuploid clones (R^2 = 0.14 for RNA, p = 0.03; R^2 =
492 0.21 for protein, p = 0.05; **Fig. 6E**). Lysosome-dysfunction cells induced by Baf A1 treatment also
493 exhibited increased CEBPB levels across multiple cell lines (p < 0.05 for HCT116, HEK293T, and
494 HeLa; **Fig. 6F**), suggesting CEBPB activation in response to aneuploidy and lysosomal dysfunction.

CEBPB activation was supported by transcription factor enrichment analysis using ChEA3 (ENCODE dataset)[63], showing significant overlap with CEBPB target genes among highly upregulated genes (log2FC > 1 & FDR < 0.01) in reversine-treated hCECs (24/257 upregulated genes, ranked 3rd among all TFs, FDR=6.38E-5) and Baf A1-treated RPE1 (14/79 upregulated genes, FDR=0.0185).

Our PARP1 CRISPR screen revealed enrichment of CEBPB-targeting sgRNAs in the PARP1-high population and depletion in the PARP1-low population ($p = 0.06$ for sgCEBPB-1; $p < 0.05$ for sgCEBPB-2, 3, 4; **Fig. 6G**), suggesting CEBPB's suppressive role in PARP1 expression. This was further corroborated by decreased PARP1 protein upon CEBPB overexpression in various cells ($p < 0.01$, **Fig. 6H**), and reduced PARP1 RNA in TCGA COREAD tumors with CEBPB copy number gain or amplification ($p < 0.01$, **Fig. S6A**). CRISPR activation (CRISPRa) Perturb-seq was performed to evaluate the impact of transcription factor activation from the endogenous locus in RPE1 epithelial cells and Hs27 fibroblasts[64]. Cells with CEBPB activation via CEBPB-targeting sgRNAs exhibited higher CEBPB levels and lower PARP1 levels compared to control cells with non-targeting sgRNAs (sgNC) (**Fig. 6I**). Taken together, these results suggest CEBPB activation suppresses PARP1 expression.

Furthermore, UMAP visualization of scRNAseq data obtained from primary colorectal cancer cells further confirmed the inverse relationship between CEBPB and PARP1, as well as their association with aneuploidy status and lysosomal alterations. In fact, cells showing high CEBPB expression also exhibited high aneuploidy scores, high lysosome scores, and low PARP1 expression and vice versa (**Fig. 6J, Fig. S6B**). These density plots reveal that aneuploid cells are associated with lysosomal alteration and CEBPB activation and tend to exhibit low PARP1 expression, providing additional evidence for the relationship between aneuploidy, lysosomal stress, CEBPB activation, and PARP1 downregulation in human colorectal cancer cells. Consistently, we observed strong inverse correlations between CEBPB and PARP1 RNA levels across pan-cancer cell lines (CCLE, Spearman $R = -0.4310$, $p < 0.0001$; **Fig. 6K**) and COREAD tumors (TCGA, Spearman $R = -0.3584$, $p < 0.0001$; **Fig. S6C**). These findings, combined with the effects of CEBPB knockout or overexpression on PARP1 expression (**Fig. 6G-6I**), strongly support CEBPB's role as a suppressive TF of PARP1. Beyond downregulating PARP1 expression, CEBPB overexpression also conferred resistance to oxidative stress-induced cell death ($p < 0.0001$, **Fig. 6L**), mirroring phenotypes observed in aneuploid, PARP1-downregulated, and lysosome-dysfunction cells. In conclusion, our data establish CEBPB as a critical TF activated in aneuploid and lysosome-deficient cells, suppressing PARP1 expression and contributing to oxidative stress resistance.

530 # Discussion

531 In this study, we discovered that aneuploid cells are exquisitely more resistant to ROS-induced cell
532 death than diploid cells (**Fig. 1, 2**). Mechanistically, PARP1 is suppressed across 15 aneuploidy
533 models (**Fig. 2**) and such suppression confers resistance against parthanatos, i.e. PARP1-mediated
534 cell death, which can be triggered by ROS, DNA alkylation, or UV radiation (**Fig. 3**). Concurrently, this
535 suppression compromises PARP1-mediated DNA damage repair in aneuploid cells (**Fig. 3**),
536 potentially contributing to tumorigenesis and cancer evolution. Accordingly, we found that PARP1
537 downregulation facilitates metastasis in near-diploid cancer cells, while its upregulation
538 suppresses metastasis in aneuploid cancers. Supporting the relevance of this mechanism for
539 human patients, we observed significantly lower PARP1 levels in metastatic versus primary tumor
540 samples (**Fig. 4**). These results suggest a novel pro-tumorigenic phenotype of aneuploidy in cancer
541 progression through PARP1 downregulation. Additionally, we performed a comprehensive screen
542 to identify regulators of PARP1 expression, revealing lysosomal stress and subsequent activation
543 of transcription factor CEBPB as possible mediators of PARP1 suppression in aneuploid cells (**Fig.
544 5-6**, **Fig. S6A-D**).
545

546 **Relationship between aneuploidy and ROS across different species**

547 Earlier studies in *Saccharomyces Cerevisiae* revealed that aneuploid yeasts show increased ROS
548 and hypersensitivity to H_2O_2[65], contrasting with our findings in human and mouse cells. Aneuploid
549 cell resistance to oxidative stress in our model is not mediated by increased ROS-buffering capacity
550 (**Fig. 2A, Fig. S2A-E**) but by reduced sensitivity to ROS-induced cell death due to PARP1
551 suppression (**Fig. 2-3**). Interestingly, *Saccharomyces Cerevisiae* lacks PARPs and PARP-like
552 proteins[66]. This likely explains the different phenotype observed in our model based on mammalian
553 cells compared to yeast.

554 Previous studies in *Drosophila* and mice demonstrated that chromosome instability (CIN),
555 induced by continuous disruption of the spindle assembly checkpoint, can increase intracellular
556 ROS levels, affecting ROS-buffering genes and cellular damage[67,68]. However, the ROS resistance
557 of aneuploid fly and mouse cells was not studied. Our human aneuploid cell analyses showed no
558 significant increase in ROS levels (data not shown), oxidative cellular damage (**Fig. 2A, Fig. S2D-
559 E**), or NRF2 activation (**Fig. S2A-C**). The discrepancy may reflect differences between aneuploidy
560 and CIN: previous studies used *Drosophila* and mouse cells with persistent CIN, while our chronic
561 aneuploidy model uses chromosomally stable clones with different aneuploidy levels, allowing us
562 to disentangle aneuploidy effects from CIN effects on ROS levels. Previous research in models of
563 Down Syndrome (DS, constitutive trisomy 21) suggest that the relationship between aneuploidy
564 and ROS levels may be cell type-dependent and did not examine ROS resistance in the aneuploid
565 cells[69,70]. Finally, it is important to note that the ROS-related superoxide dismutase 1 (SOD1) is
566 encoded by a gene located on chromosome 21, thus further complicating the interpretation of ROS-
567 related findings in DS in comparison with other aneuploidies.

568

569 **PARP1 is suppressed in aneuploid cells via CEBPB transcription factor**

570 Our results establish a robust association between aneuploidy and PARP1 downregulation across
571 15 cell models, regardless of TP53 status, altered chromosomes in the aneuploid cells, cell lineage,
572 and aneuploidy induction methods (**Fig. 2**). In addition to our experimental models and published
573 omics data from aneuploid cells, we confirmed these results by analyzing published western blot
574 images from multiple aneuploidy models, including reversine-treated RPE1, glioma cells, and
575 mouse embryo[28,37,38], and MMCT-generated HCT116 with an extra chromosome 3[71]. Notably,
576 chromosome 3 gain reduced both PARP1 protein levels and activity in HCT116[71], suggesting
577 aneuploidy's dual suppressive effect on PARP1. Furthermore, we observed decreased levels of
578 TIMELESS, a key PARP1 interactor, in aneuploid cells (**Fig. S3B-C**). This decrease may impair
579 PARP1's binding to DNA damage lesions and its activation, potentially explaining the reduced
580 PARP1 activity in aneuploid cells. Intriguingly, a recent study suggested that PARP1 inhibition
581 rescued survival and proliferation of aneuploid cells in developing mouse embryos[8].

582 Our data indicate that PARP1 suppression in aneuploid cells does not result from cell cycle
583 dysregulation. Although limited studies suggested that PARP1 levels typically peak during S and
584 G2/M phases and decrease during G1 arrest[72–75], our findings indicate that PARP1 downregulation
585 in aneuploid cells is not linked to G1 prolongation or arrest. First, PARP1 downregulation occurs in
586 both TP53WT and TP53KO aneuploid cells (**Fig. 2**), despite aneuploidy-induced G1 arrest being
587 p53-dependent[76,77]. Second, aneuploid cells generated by MMCT and KaryoCreate show PARP1
588 downregulation (**Fig. 2I, Fig. S2I-K**), while maintaining cell cycle profiles[78] and proliferation rates
589 similar to their diploid counterparts (**Fig. 1I**). Third, certain high-aneuploidy colon cancer cells
590 exhibit lower PARP1 levels (**Fig. 4A**) despite similar or higher S phase proportions compared to low-
591 aneuploidy cells[79,80]. Collectively, these findings indicate that PARP1 downregulation in aneuploid
592 cells is not attributable to cell cycle changes.

593 Our unbiased CRISPR screen identified PARP1 expression regulators, providing a valuable
594 resource for PARP1 research given the current limited knowledge on the regulation of PARP1
595 expression[74,81]. Integration with RNAseq data revealed that alterations in ribonucleotide reductase,
596 microRNA biogenesis, and phagosome maturation (**Fig. S5E**) may contribute to PARP1
597 downregulation in aneuploid cells. Notably, the phagosome maturation pathway, which includes
598 many lysosomal genes, particularly lysosomal V-ATPase genes (**Fig. S5F**), is noteworthy. Previous
599 studies and our data (**Fig. 5F-H**) indicate that lysosomal stress is a common feature in aneuploid
600 cells[28,29]. We demonstrated that lysosome inhibition induces PARP1 downregulation in multiple cell
601 lines (**Fig. 5I**), conferring cell resistance to ROS-induced cell death in a PARP1-dependent manner
602 (**Fig. 5J-K**). These results suggest lysosomal stress is a potential mediator of PARP1
603 downregulation in aneuploid cells.

604 Furthermore, we found that aneuploidization and lysosome dysfunction lead to a striking
605 nuclear increase in CEBPB levels (**Fig. 6**). Genetic experiments on CEBPB support its critical role in

606 mediating PARP1 regulation and ROS resistance in aneuploid cells. In addition, scRNAseq of
607 primary colon cancer cells showed a strong inverse relationship between CEBPB and PARP1, and
608 a positive correlation between aneuploidy and CEBPB. Our findings provide new mechanistic
609 insights into PARP1 suppression under aneuploidy and lysosomal stress conditions. Previous
610 studies showed that aneuploidy induces proteotoxic stress, which in turn activates autophagy and
611 lysosomal pathways as compensatory mechanisms through transcription factor EB (TFEB)[28].
612 However, the excessive demands for protein degradation in aneuploid cells impair autophagic flux
613 and cause lysosome dysfunction. While current literature lacks a direct link between aneuploidy
614 and CEBPB, several lines of evidence support a potential connection. Studies have demonstrated
615 that autophagy deficiency in macrophages activates CEBPB[82]. Additionally, C/EBP family TFs are
616 crucial for autophagy activation during amino acid starvation[83]. Finally, lysosomal dysfunction may
617 activate CEBPB through the unfolded protein response (UPR). In fact, lysosome dysfunction can
618 trigger ER stress and UPR. In turn, UPR leads to the activation of several TFs, including CEBPB[84,85].
619 Therefore, we propose that lysosome dysfunction in aneuploid cells may lead to CEBPB activation
620 possibly through the UPR pathway, leading to PARP1 repression and resistance to parthanatos.
621
622 **PARP1 suppression impacts cell death, DNA repair and metastasis: the perfect storm**
623 PARP1 downregulation emerges as the main mechanism underlying aneuploid cells' resistance to
624 ROS-induced cell death (**Fig. 2, 3**). This PARP1-mediated cell death, termed parthanatos, occurs
625 after toxic insults (e.g., ischemia-reperfusion, inflammatory, and ROS-induced injury) where cells
626 experience stresses and accumulate excessive oxidative DNA damage[22,86]. However, parthanatos
627 remains poorly understood in cancer[27]. Parthanatos relies on PARP1 hyperactivation caused by
628 profound DNA damage, leading to cell death through NAD+ and ATP[23] depletion or AIF nuclear
629 translocation[24]. Our results demonstrate that modulating PARP1 levels in diploid or aneuploid cells
630 directly affects their resistance to ROS-induced cell death (**Fig. 3**), strongly supporting PARP1
631 downregulation as the key factor in aneuploid cells' resistance. PARP1 activity may also be
632 suppressed in aneuploid cells[71], possibly related to TIMELESS downregulation (**Fig. 3I**, **Fig. S3B-**
633 **D**). The cytoprotective effect of PARP1 inhibition or downregulation has been observed in various
634 non-cancerous conditions, including neurological and neurodegenerative diseases, ischaemic
635 reperfusion, diabetes, colitis, arthritis, liver toxicity, uveitis, skeletal muscle differentiation, and aging
636 human skin[41,75,87–90]. Beyond ROS, other cancer-related DNA damaging insults, such as DNA
637 alkylation, UV radiation, ionizing radiation, may also trigger parthanatos[41], aligning with our
638 observation of aneuploid cells' increased resistance to alkylating agent MNNG and UV radiation
639 (**Fig. 3K-L**). These findings may explain previous observations of aneuploidy-induced resistance to
640 certain chemotherapy and radiation therapy[9,10,91–93].
641 In addition to conferring resistance to parthanatos, PARP1 downregulation impairs their
642 repair of both oxidative and alkylating DNA damage in aneuploid cells (**Fig. 3M**, **Fig. S3J-K**). The
643 temporal dynamics of γH2AX after H_2O_2 or MNNG exposure in diploid hCECs and PARP1-

644 overexpressing aneuploid hCECs, but not in aneuploid hCECs, indicates that efficient repair of
645 oxidative and alkylating DNA damage is impaired in aneuploid cells. Our findings align with earlier
646 research showing PARP1 depletion reduces SSB repair rates across various species[94]. Similarly,
647 PARP1 partial downregulation in senescent epithelial cells led to defective repair of oxidative DNA
648 damage, which could be rescued by PARP1 overexpression[75]. Notably, aneuploid cells did not
649 exhibit impaired repair of DNA damage induced by certain agents different than H_2O_2, MNNG or UV
650 (such as camptothecin, etoposide, pyridostatin, doxorubicin, or bleomycin). This selectivity may be
651 due to these agents inducing multiple DNA damage repair mechanisms, some independent of
652 PARP1. In fact, oxidative DNA damage is exclusively repaired by BER, which heavily relies on PARP1,
653 while other DNA repair pathways, such as classical non-homologous end-joining, remain
654 unaffected by PARP1 loss or inhibition[21,95,96]. Taken together, we propose that aneuploidy can
655 create a 'perfect storm' where resistance to cell death is coupled with decreased DNA repair under
656 oxidative stress via PARP1 downregulation, potentially promoting tumorigenesis and cancer
657 evolution. We also note that a recent study reported increased resistance of aneuploid cells to
658 etoposide and other DNA damage agents[10], due to RAF/ERK activation but this mechanism was
659 not at play in parthanatos resistance observed in our system.
660 It is seemingly counterintuitive that cells with impaired DNA damage repair can survive
661 better. While DNA damage typically triggers cell death through disrupted replication or
662 transcription[25], the close interplay between PARP1-mediated DNA repair and cell metabolism
663 (consumption of NAD+ and ATP)[46] creates a unique survival-death balance. Excessive single-
664 strand breaks overactivate PARP1, rapidly depleting NAD+ and ATP. This energetic catastrophe
665 can be more acutely lethal than the DNA damage itself, leading to parthanatos[25]. Consequently,
666 suppressing PARP1-mediated repair is pro-survival to preserve the energy homeostasis for cells
667 with high levels of single-strand breaks, which can be induced by ROS and alkylating agents.
668 Our findings support a pro-metastatic role of PARP1 downregulation (**Fig. 4**). Suppressing
669 PARP1 expression in low-aneuploidy COREAD cell lines effectively enhanced their ROS resistance
670 (**Fig. 4F-G**, **Fig. S4B**) and metastatic potential (**Fig. 4H-I**). Conversely, promoting PARP1 expression
671 in high-aneuploidy KP lung cancer cells decreased their metastatic potential (**Fig. 4J**). Furthermore,
672 PARP1 expression was found lower in metastatic tumors compared to primary tumors from
673 COREAD patients (**Fig. 4M-N**). This pro-metastatic effect of PARP1 downregulation likely stems
674 from enhanced ROS resistance, as oxidative stress is a known barrier to cancer metastasis[16–18].
675 Interestingly, conflicting results regarding PARP1 inhibition or knockdown on metastasis have been
676 described[97–99]. This discrepancy may reflect the heterogeneity in redox sensitivity among distinct
677 tumor types. Additionally, the "double-edged sword" effect of PARP1 activity may also induce
678 tissue-specific response. In tumor cells highly tolerant to PARP1-induced cell death (e.g., cells with
679 high NAD+), high PARP1 expression may be favored, enhancing DNA repair without inducing cell
680 death. Conversely, in cancer cells susceptible to PARP1-induced cell death, lower PARP1 levels may

681 prevent cell death, potentially compromising efficient DNA damage repair[16,27]. Further research into
682 cancer cell susceptibility to PARP1-mediated cell death will help clarify these discrepancies.
683
684 **Implication for cancer treatment**
685 While our study focuses on HR-proficient tumors and does not investigate HR-deficient tumors, i.e.
686 the main target of successful PARP1 inhibition in the clinic[100], our findings may provide implications
687 for current and future clinical use of PARPi as monotherapy or in combination treatments. PARP1
688 downregulation has been shown to drive PARP1i resistance[101–103], suggesting that aneuploid
689 cancer cells may possess inherent PARP1i resistance due to PARP1 downregulation, which is
690 confirmed by analysis of PARPi sensitivity in CCLE cancer cell lines (**Fig. S6E**). Combination
691 treatments of PARP1i and DNA damage-inducing agents are also under clinical evaluation[104].
692 However, our results indicate that PARPi might actually inhibit the cytotoxic effect of DNA damage-
693 inducing agents if their efficacy relies on PARP1 hyperactivation and induction of parthanatos. This
694 is supported by a recent study showing that the frontline drug combination of cytarabine and
695 idarubicin induces parthanatos in acute myeloid leukemia cells, with reduced cytotoxicity in cancer
696 cells expressing low PARP1 levels[27]. Altogether, our studies, by shedding light on a previously
697 unappreciated effect of aneuploidy in promoting ROS resistance through PARP1 suppression, pave
698 the way to future studies aimed at better characterizing the implications for these results for cancer
699 therapies and resistance.
700
701

702 STAR Methods

703
704 **Cell Culture**
705 hTERT-immortalized hCECs[105] were cultured in a 4:1 mixture of DMEM/Medium 199,
706 supplemented with 2% fetal bovine serum (FBS), 5 ng/mL epidermal growth factor (EGF), 1 μg/mL
707 hydrocortisone, 10 μg/mL insulin, 2 μg/mL transferrin, and 5 nM sodium selenite. hTERT-
708 immortalized RPE1 cells were cultured in DMEM/F-12 supplemented with 10% FBS. hTERT-
709 immortalized hPNE were cultured in RPMI 1640 supplemented with 10% FBS. hTERT-immortalized
710 hMEC were cultured in Mammary Epithelial Cell Culture Kit (Lonza, CC-2551B). Colon cancer cells
711 (HCT116, DLD1, HT29, SK-CO-1, SW403, SW948), aneuploid clones of HCT116 and RPE1 cells
712 generated through MMCT (HCT116-5/3-C1, HCT116-5/3-C2, RPE1-7/3), and their near-diploid
713 clones (HCT116-2N, RPE1-2N), were cultured in DMEM supplemented with 10% FBS. HEK-293T
714 were cultured in DMEM supplemented with 10% bovine calf serum (BCS). All media for the above
715 human cells were supplemented with 100 U/mL penicillin-streptomycin and 2 mM L-glutamine.
716 Mouse KP cancer cells were isolated from tumor nodules of the lung of KP ($Kras^{G12D}Trp53^{-/-}$)
717 genetically engineered mouse models (GEMMs) from C57BL/6 as described previously [32,33], and

718 cultured in RPMI 1640 supplemented with 10% FBS, 1X antibiotic-antimycotic, and 1X GlutaMax.
719 All cells were cultured in a humidified environment at 37°C and 5% CO_2 and were tested free of
720 mycoplasma contamination.
721
722 **Plasmid construction**
723 TP53 was knocked out in hCECs by transfection with a Cas9-containing plasmid (Addgene #42230)
724 and pLentiGuide-Puro expressing the following sgRNA: 5'gcatgggcggcatgaaccgg3'. Clones were
725 derived and the effect on TP53 level was confirmed using western blot.
726
727 For the generation of aneuploid mouse KP cancer cells by KaryoCreate (see description below), KP
728 cells were lentivirally transduced with pINDUCER20-AuroraB-dCas9 and sgRosa26 or sgMinSat5.
729
730 To clone AuroraB-dCas9 fusion protein, dCas9 without ATG and without stop codon (for N-terminal
731 and C-terminal tagging respectively) were cloned into the pENTR vector using the D-TOPO cloning
732 kit (Thermo Scientific, K240020). AuroraB was PCR amplified from a template vector from the
733 ultimate ORF collection[106] using the forward primer
734 (5'tccgcggccccccttcacccatggcccagaaggagaactcc3') and the reverse primer
735 (5'gctgtacttcttgtcctcgagcgaccctccgccggaaccgccggcgacagattgaa3'), and fused to dCas9 into
736 pENTR-dCas9-noATG including the GGSGGGS linker. The fusion protein was then cloned into a
737 tetracycline response element (TRE)-included donor vector, pINDUCER20 (or pIND20, neomycin
738 resistance, doxycycline inducible promoter)[107].
739
740 The sgRosa26 (the target sequence: 5'aacggctccaccacgctcgg3') and sgMinSat5 (the target
741 sequence: 5'aaaacacattcgttggaaac3') were cloned into pLRCherry V2.1 as reported previously[34]. In
742 brief, to be suitable for cloning into BbsI-digested vectors, sense oligos were designed with a
743 CACCG 5' overhang and antisense oligos were designed with an AAAC 5' overhang and an 3' end
744 C. The sense and anti- sense oligos were annealed, phosphorylated, and ligated into BbsI-digested
745 pLentiGuide-Puro-FE.
746
747 For introduction of PARP1, GFP-NLS into cells, human PARP1 cDNA was PCR amplified from the
748 pBABE-puro-Halo-PARP1[108] plasmid using the forward primer (5'caccatggcggagtcttcggataagct3')
749 and the reverse primer (5'ttaccacagggaggtcttaaaattg3'). GFP-NLS cDNA was PCR amplified from
750 a template plasmid using the forward primer (5'ttacaccttgcgtttttttcttgggcttgtacagctcgtccatg3') and
751 the reverse primer (5'ttaccacagggaggtcttaaaattg3'). After gel purification using the Nucleospin Gel
752 and PCR Clean-UP kit (Macherey-Nagel, 740609), the DNA fragment was inserted into the pENTR
753 vector using the D-TOPO cloning kit (Thermo Scientific, K240020), following the manufacturer's
754 instructions. Then the PARP1 or GFP-NLS sequence was integrated into the pHAGE-CMV-blast or
755 pHAGE-TRE-hygro donor vectors via the LR reaction using the Gateway cloning kit (Thermo

Scientific, 11791020), following the manufacturer's protocol. For the control plasmid, the same vector was used with a short random sequence (5'GACATAGTACAG3') replacing the PARP1 or GFP-NLS sequence.

For introduction of human TIMELESS or mouse PARP1 into cells, human TIMELESS cDNA was PCR amplified from a DNA template (a gift from Dr. Jef Boeke) using the forward primer (5'tacaaaaaagcaggctccgcggccgcccccttcaccatggacttgcacatgatgaa3') and the reverse primer (5'gtacaagaaagctgggtcggcgcgcccaccttctagtcatcctcatcatcct3'). Mouse PARP1 cDNA was PCR amplified from ZS-pEGFP-n-mPARP1 (a gift from Dr. Zha Shan Lab) using the forward primer (5'tacaaaaaagcaggctccgcggccgcccccttcaccatggcggaggcctc3') and the reverse primer (5'aagaaagctgggtcggcgcgcccaccttctaccacagggatgtcttaaaattgaacttg3'). The gel-purified DNA fragment was assembled with AscI/NotI-linearized pENTR vector using Gibson Assembly. The mouse PARP1 sequence was then recombined into the pHAGE-CMV-blast destination vector via LR Clonase reaction.

For PARP1, GPX1, CAT knockdown, two shRNAs targeting each gene (shPARP1-1: cttcgttagaatgtctgcctt, shPARP1-2: gcagcttcataaccgaagatt, shGPX1-1: gcaaggtactacttatcgaga, shGPX1-2: gcatcaggagaacgccaagaa, shCAT-1: gccacatgaatggatatggat, shCAT-2: cggagattcaacactgccaat) in MISSION® TRC1 lentiviral vector were purchased from Sigma-Aldrich (TRCN0000007928 and TRCN0000007929). The MISSION® pLKO.1-puro non-mammalian shRNA plasmid targeting no known mammalian genes was used as the control (Sigma-Aldrich, SHC002).

For PARP1, PARP2, and MIF knockout, sgRNA sequences (sgPARP1: 5'-TAACGATGTCCACCAGGCCA-3', sgPARP2: 5'-CGGCGGCGACGGAGCACCGG-3', sgMIF: 5'-GAGGAACCCGTCCGGCACGG-3') were cloned into the LentiCRISPR-V2-FE-puro vector (Addgene #186746). The sgRNA sequences with flanking homology regions were synthesized as oligonucleotides (IDT) and inserted into BsmBI-linearized LentiCRISPR-V2-FE-puro using Gibson assembly. For NRF2 knockout, LentiCRISPR-V2-NRF2 were obtained from Addgene (186838, 186839).

Lentivirus production and infection

For transduction of cells, lentiviral particles were generated as follows: 15 million 293T cells per 10-cm dish were plated 24 hours before transfection. The cells were transfected with a mixture of gene transfer plasmid (6 μg) and packaging plasmids including 10 μg psPAX2 (addgene, 12260) and 5 μg pMD2.G (VSV-G; addgene, 12259), using Lipofectamine 3000 (ThermoFisher, L3000075). The medium was changed 6 hours later and virus was collected every 24 hours after transfection (three times in total) by filtering the medium through a 0.45-μm filter. Polybrene (4 μg/mL, company,

793 cat number) was added to the filtered media before infection. The media containing lentivirus was
794 replaced with fresh media with appropriate antibiotic selection 24 hours after infection.
795
796 **Aneuploidy models**
797 *MPS1i-induced acute aneuploidy*
798 To study the short-term effects of aneuploidy, irrespective of specific chromosome gains or losses,
799 we utilized a model of **acute aneuploidy** in which near-diploid cells were treated with MPS1i
800 (reversine or AZ3146) to induce chromosome missegregation. TP53WT or TP53KO hCECs, RPE1,
801 DLD1, and mouse KP cancer cells were seeded at 30% confluency and treated with either 0.5 μM
802 reversine or 5 μM AZ3146 for 24-30 hours. hMECs were treated under similar conditions but with
803 an extended 48-hour exposure to the inhibitors. Subsequently, the cells were trypsinized and
804 cultured in the regular medium for 3 days (the release phase). Over-confluence was avoided both
805 during MPS1i treatment and the release phase. The control group was treated with an equivalent
806 amount of DMSO (0.1% v/v) for an identical duration and was then released for the same time
807 period. Both the diploid control (treated with DMSO) and the aneuploid cells (treated with reversine
808 or AZ3146) were plated on new culture dishes or plates to achieve comparable confluency on the
809 second day for downstream comparisons. To assess the potential side effects of MPS1i, confluent
810 hCECs with temporarily suppressed proliferation were treated with 0.1% DMSO or MPS1i (0.5 μM
811 reversine or 5 μM AZ3146) for 24-30 hours, followed by a 3-day release and replating for
812 downstream experiments. Over-confluence was only avoided during the release phase. The
813 induction of aneuploidy was confirmed through flow cytometric analysis of DNA content and
814 scRNAseq-based CNA quantification (see description below).
815
816 *Isogenic clones containing different aneuploidy levels*
817 To study the longer-term effects during adaptive stages of aneuploidy, irrespective of specific
818 chromosome gains or losses, a model of **chronic aneuploidy** was developed. Near-diploid TP53KO
819 hCECs were exposed to 0.2 μM reversine for 24 hours. Then they were plated at a low density and
820 allowed to grow until colonies formed. Single-cell-derived clones were isolated using glass
821 cylinders and transferred to separate wells in multiwell plates for further expansion. To identify
822 chromosomal gains and losses, the DNA of a cohort of 56 isogenic hCEC clones was extracted and
823 subjected to shallow whole-genome sequencing (see description below). The clones were
824 categorized as near-diploid, exhibiting 0-2 gains or losses of chromosomes or chromosome arms
825 (designated as D followed by numbers), or as aneuploid, with ≥ 5 gains or losses of chromosomes
826 or chromosome arms (designated as A followed by numbers).
827
828 *Aneuploid mouse KP cancer cells induced by KaryoCreate targeting pan chromosomes*
829 Independently of MPS1i, we generated aneuploid mouse KP cancer cells using our recently
830 developed KaryoCreate method[34] to validate the findings derived from MPS1i-induced aneuploid

831 cells. The mouse KP cancer cells were transduced to express an sgRNA targeting the minor
832 satellite regions of all mouse centromeres (sgMinSat5) and TRE-driven AuroraB-dCas9. sgMinSat5
833 directed the AuroraB-dCas9 proteins to the targeted centromeres, interfering with normal mitotic
834 function and leading to chromosome missegregation and aneuploidy. The near-diploid control cells
835 were infected with lentivirus carrying an identical DNA construct but with a non-centromeric sgRNA
836 targeting the Rosa26 locus in the mouse genome (sgRosa26). Then the cells were treated with 1
837 μg/mL doxycycline for two weeks to induce the expression of AuroraB-dCas9 and the generation
838 of aneuploidy, which was confirmed through flow cytometric analysis of DNA content and
839 chromosome counting in metaphase spreads (see description below).
840
841 *Previously published Aneuploidy models generated by MMCT*
842 Microcell-mediated chromosome transfer (MMCT) is a common method for generating aneuploid
843 clones with one or two extra chromosomes[109]. Aneuploid clones of HCT116 with an extra
844 chromosome 5 and RPE1 with an extra chromosome 7, along with their diploid control clones[31],
845 generously provided by Dr. Zuzana Storchová and Dr. Jason M. Sheltzer, served as an independent
846 aneuploidy model to test our hypotheses.
847
848 **Flow cytometry-based measurement of DNA content**
849 One million cells were collected and resuspended in 300 μL of cold phosphate buffered saline
850 (PBS). Then 700 μL of ice-cold 100% ethanol was added dropwise as cell suspensions were
851 vortexed at medium speed to ensure complete fixation. The cell suspensions were stored at 4℃
852 overnight. On the following day, the cells were resuspended in 500 μL of staining buffer (PBS
853 supplemented with 2 mM EDTA, 0.1 mg/mL RNAse A, 0.01 mg/mL propidium iodide (PI), and 0.5%
854 bovine serum albumin (BSA)), and then incubated for 1-3 hours at room temperature in the dark.
855 Then 200 μL of cell suspensions were transferred to round-bottom 96-well plates for flow
856 cytometric measurement of cellular PI intensity. Flow cytometry acquisition was performed using
857 the SONY SA3800 spectral cell analyzer. PI was excited by a 561 nm laser and its fluorescence was
858 measured through the total signal of two consecutive channels centered around 617 nm. Data
859 analysis was performed using FlowJo with consecutive gating to exclude cell debris and doublets.
860
861 **Metaphase spreading for chromosome counting**
862 Cells were plated in 10 cm dishes to reach 70% confluency at the time of harvest. Before harvesting,
863 the cells were treated with 0.1 μg/mL colcemid at 37℃ for 4 hours. Then cells were trypsinized and
864 washed once with PBS. The cell pellet was then resuspended in 0.5 mL of PBS by tapping, followed
865 by the addition of 10 mL 0.075 M potassium chloride (KCl), pre-warmed to 37℃. After thorough
866 mixing by gently inverting, cells were incubated for 7 minutes at 37℃. Then 1 mL of methanol-acetic
867 acid (3:1) was added to the cell solution, followed by thorough mixing and a 10-minute incubation
868 at room temperature. Then cells were resuspended in 0.5 mL of 0.075 M KCl, and 9 mL of methanol-

acetic acid (3:1) was added dropwise while vortexing the cell suspensions at medium speed to ensure complete fixation. The fixed cells were resuspended in 0.5 mL of fresh methanol-acetic acid (3:1) and dropped from a couple of inches above the end of cold slides tilted at a 45° angle. After overnight air drying, the slides were stained with Vectashield antifade mounting media containing DAPI (H-1200-10). The mounted slides were imaged using the Invitrogen EVOS M7000 imaging system or the Nikon spinning disk confocal microscope.

Single-cell RNA sequencing

Single-cell RNA sequencing (scRNA-seq) was employed to infer somatic copy number alterations (SCNA) in TP53KO hCECs treated with either DMSO or MPS1i, as previously described[34]. scRNA-seq libraries were constructed using the 10X Chromium Single-Cell 3' v3 Gene Expression kit in accordance with the manufacturer's instructions, which also included the manufacturer's protocol for cell surface protein (hashtag antibody) feature barcoding for samples multiplexing. The CellRanger v6.1 pipeline (10X Genomics) was used to process raw scRNA-seq data, generating gene expression matrices. To identify the sample of origin for each cell barcode, HTO count data from each 10X Chromium experiment were demultiplexed using the Seurat package (v4.0.3).

After the removal of low-quality cells and potential cell doublets, a modified version of the CopyKat (v1.0.5) pipeline was used to generate a SCNA score for each chromosome arm in each cell. Hashtagged samples from the same treatment in each 10X Chromium dataset were grouped together for analysis. In each analysis, genes expressed in fewer than 5% of the cells, HLA genes, and cell-cycle genes were excluded. The log-Freeman-Tukey transformation was employed to stabilize variance, and dlmSmooth was used to smooth outliers. The DMSO-treated diploid control sample was used to calculate a baseline expression level for each gene. This value was subtracted from the samples in the set, thereby centering the expression of the control sample around 0. Genes expressed in fewer than 10% of cells were subsequently excluded from further analysis. Then a SCNA value was generated for each chromosome arm by calculating the mean gene expression for the genes on that arm. To account for its relatively small size, a single SCNA value for the entire chromosome 18 was calculated using genes from both the p and q arms. SCNA values for chromosomes 13, 14, 15, 21, and 22 were calculated only using genes on their respective q arms. Gains or losses of a chromosome arm relative to the control sample (diploid) were called based on a threshold calculated from the control sample for each chromosome arm using the following formula:

$$threshold = median \pm (2.5 \times MAD)$$

where the median is calculated from the SCNA values for each arm in the control sample, and the median absolute deviation (MAD) is calculated by the mad function from the stats R package. A chromosome arm was recognized as gained (or lost) if its SCNA value was above (or below) the threshold for its sample set. The heatmap of arm-level SCNA was visualized using R package ComplexHeatmap (v2.6.2).

908

909 **Shallow whole-genome sequencing (WGS)**

910 The genomic DNA of hCEC clones was extracted from trypsinized cells using 0.3 µg/µL Proteinase
911 K in 10 mM Tris pH 8.0 for 1 hr at 55°C, followed by heat inactivation at 70°C for 10 minutes.
912 Genomic DNA was then enzymatically digested using NEBNext dsDNA Fragmentase for 25
913 minutes at 37°C, followed by magnetic DNA bead cleanup using Sera-Mag Select Beads at a beas-
914 to-lysate ratio of 2:1 by volume. Subsequently, DNA libraries were prepared with an average
915 fragment size of 320 bp using the NEBNext Ultra II DNA Library Prep Kit for Illumina, following the
916 manufacturer's instructions. In brief, after phosphorylation, dA-Tailing and adaptor ligation of
917 fragmented DNA, unique barcodes were added to each sample and PCR amplification was
918 performed, followed by a bead cleanup. Quantification was performed using a Qubit 2.0 fluorometer
919 and the Qubit dsDNA HS kit. The libraries were then sequenced on an Illumina NextSeq 500 at a
920 target depth of 4 million reads in either paired-end mode (2 X 36 cycles) or single-end mode (1 X
921 75 cycles). Low-pass (~0.1-0.5X) WGS reads of hCEC were aligned to reference human genome
922 hg38 using BWA-mem (v0.7.17) and the duplicates was removed using GATK (Genome Analysis
923 Toolkit, v4.1.7.0) to generate analysis-ready BAM files. The resulting BAM files were processed
924 using the R package CopywriteR (v1.18.0) to determine the arm-level copy numbers. The heatmap
925 of arm-level SCNA was visualized using R package ComplexHeatmap (v2.6.2).

926

927 **Aneuploidy score**

928 Aneuploidy was quantified by estimating the total number of arm-level gains and losses for each
929 hCEC clone, cancer cell line, or tumor sample. For hCEC clones, the arm-level copy number
930 alterations were calculated based on the copy number package[110]. We considered a log2-
931 transformed copy number ratio > 0.3 as a gain and <(−0.3) as a loss. The aneuploidy scores of
932 CCLE cancer cell lines were downloaded from Depmap portal[111]. For Fig. 4B and 4C, cell lines were
933 stratified into three groups based on aneuploid scores (low, medium, and high aneuploidy) with the
934 same number of cells in each group (pan-cancer: 314 cell lines per group; COREAD: 18 cell lines per
935 group). For TCGA COREAD samples, the arm and gene level somatic copy number alteration data
936 were obtained from the TCGA dataset. The log2-transformed copy number ratios for each
937 chromosomal region were adjusted by tumor purity and ploidy using ABSOLUTE method [112].
938 Sample-related purity and ploidy were downloaded from TCGA Firehose Legacy. The detailed
939 method for copy number adjustment based on purity and ploidy was described before[113]. After the
940 adjustment, we considered a log2-transformed copy number ratio > 0.3 as a gain and < (−0.3) as a
941 loss.

942

943 **Assessing cellular sensitivity to different types of cellular perturbations**

944 Cell sensitivity to different cellular stress between diploid and aneuploid hCECs was compared.
945 First, TP53WT diploid hCECs were labeled with nuclear-localized GFP using lentiviral transduction,

946 followed by fluorescence-activated cell sorting (FACS). Then the unlabeled hCECs were treated with
947 MPS1i to induce aneuploidy, while the labeled hCECs were treated with DMSO as a diploid control.
948 One day before the addition of the stress-inducing drugs, DMSO-treated diploid hCECs (labeled with
949 GFP) and MPS1i-treated aneuploid hCECs (unlabeled) were plated into individual 96-well plates at
950 a density that allowed cells to reach a comparable confluent level of 60% when cells were treated
951 with drugs. On the second day, the culture media was replaced with fresh media containing one of
952 the following drugs: 30-50 μM H_2O_2, 100 nM bafilomycin A1, 50 μM chloroquine, 100 nM MG132,
953 100 nM bortezomib, 10 μM 17AAG, 5 μg/mL tunicamycin, 1.5 μM oliomycin, 50 nM rotenone, 100
954 μg/mL chloramphenicol, 50 or 200 μM bleomycin, 50 or 200 μM etoposide, 10 or 50 μM
955 camptothecin, 20 or 100 μM pyridostatin, 250 or 1000 μM temozolomide, 500 nM erastin, 20 mM
956 2DG, 50 μM EHT1864, 100 μM NSC23766, 10 μM UC2288, 5 μM TPCA1, or 1 μM JNK-IN-8. The
957 cells were grown in the presence of the drugs for 24 hours. Following this, the cells were harvested
958 and the labeled diploid hCECs were mixed with the unlabeled aneuploid hCECs under identical
959 conditions. The cell mixture was stained with 2 μg/mL PI for 10 minutes in the dark, and then
960 analyzed using flow cytometry to assess the cell number ratios between viable diploid (PI- and
961 GFP+) and aneuploid (PI- and GFP-) hCECs under varying conditions.
962
963 **Assessing cellular sensitivity to oxidative stress**
964 To compare H_2O_2 sensitivity, cells were cultured on multiwell plates to achieve a comparable
965 confluence at the time of H_2O_2 addition. On the second day, the culture medium was replaced with
966 fresh medium containing H_2O_2. Cells were subjected to a gradient of H_2O_2 concentrations to
967 determine the concentrations at which a portion of cells died, while avoiding high concentrations
968 that resulted in complete cell death for all cells. Following a 24-hour treatment in a humidified
969 environment at 37℃ with 5% CO_2, the relative cell viability was examined (see description below).
970 In some cases, cells were treated with H_2O_2 for one hour and then released for 24 hours before the
971 detection of the relative viability. The brief H_2O_2 exposure aimed to mitigate the influence of altered
972 cell cycles and varying proliferation rates in diploid and aneuploid cells. The figure legends specify
973 the concentration and duration of H_2O_2 treatment.
974
975 To assess cell sensitivity to oxidative stress induced by lower concentrations of H_2O_2 over an
976 extended duration, we used two independent assays to compare near-diploid and aneuploid hCEC
977 clones. First, three GFP-labeled near-diploid hCEC clones and three unlabeled aneuploid hCEC
978 clones were mixed in equal numbers. These mixed cells were cultured in the presence of low
979 concentrations of H_2O_2 for three days (2-20 μM), without being confluent. The ratio of live cell
980 numbers between GFP-labeled near-diploid and unlabeled aneuploid hCECs were measured using
981 flow cytometry. Second, 10,000 near-diploid and aneuploid hCECs, with each group consisting of
982 three hCEC clones with different karyotypes in equal cell numbers, were mixed with 2 mL of 37℃
983 0.45% low melting temperature agarose, with or without 10 μM H_2O_2, and added to 6-well plates

984 pre-coated with 0.9% low melting temperature agarose. After the gel solidified, the cells were grown
985 in a humidified environment at 37℃ with 5% CO_2, and fresh medium with or without 10 μM H_2O_2
986 were added to the top of the agarose daily. After ten days of growth, the colonies were stained with
987 150 μL of 2 mg/mL nitro blue tetrazolium and imaged with the Microtek scanner (TMA 1600-III,
988 ScanMaker 9800XL plus). The number of colonies for near-diploid and aneuploid hCECs were
989 quantified using Fiji software and compared.
990
991 To evaluate cell sensitivity to oxidative stress induced by alternative methods, we compared the
992 relative viability between near-diploid and aneuploid hCEC clones after treatment with 100 μM
993 xanthine and 20 mU/mL xanthine oxidase for 24 hours. Control cells were treated with 100 μM
994 xanthine alone for the same duration. In the presence of the xanthine and xanthine oxidase, both
995 superoxide and H_2O_2 are generated. Cells were subjected to varying concentrations of xanthine and
996 xanthine oxidase to determine the concentrations at which a portion of cells died, while avoiding
997 high concentrations that resulted in complete cell death for all cells.
998
999 To compare the H_2O_2 sensitivity of unattached cells (Fig. S1H), 100 μL of medium with or without
1000 45 μM H_2O_2 was pre-added to 48-well plates. Then 35,000 hCECs in 200 μL of medium were added
1001 into the 48-well plates, followed by thorough mixing. Cell viability was examined after a 24-hour
1002 culture in a humidified environment at 37℃ and 5% CO_2. To compare the H_2O_2 sensitivity of cells
1003 attached to different surfaces (Fig. S1I), multiwell plates were coated with cold DMEM containing
1004 1% GelTrex (LDEV-free reduced growth factor basement membrane matrix) in a humidified
1005 environment at 37℃ and 5% CO_2 for at least one hour. After removing the coating solution, cells
1006 were plated on the multiwell plates to achieve a comparable confluence at the time of H_2O_2
1007 addition. 50 μM H_2O_2 were added into plates on the second day and cell viability was examined 24
1008 hours after H_2O_2 treatment.
1009
1010 **Sensitivity to other drugs or UV treatment**
1011 To arrest diploid cells at the G1 or S phase, TP53KO diploid hCECs were treated with 0.5 μM
1012 palbociclib (a CD4/6 inhibitor, Selleck Chemicals, S1116) or 2 mM thymidine (a DNA synthesis
1013 inhibitor, Sigma-Aldrich, T1895) for 24 hours. Following this treatment, the culture medium was
1014 replaced with a fresh medium containing 100 μM H_2O_2 in addition to 0.5 μM palbociclib or 2 mM
1015 thymidine for another 24 hours to compare the ROS resistance of the arrested cells.
1016
1017 To determine the specific form of cell death activated under oxidative stress, we treated the cells
1018 with inhibitors of distinct cell death pathways, including apoptosis (10 μM Z-VAD-FMK, Selleck
1019 Chemicals, S7023), necrosis (20 μM necrostatin-7, Cayman Chemical, 10528), ferroptosis (20 μM
1020 ferrostatin-1, Sigma-Aldrich, SML0583), and parthanatos (10 μM olaparib, Cell Signaling, 93852S),
1021 before and after H_2O_2 treatment to test if any of them was able to rescue the effects of H_2O_2

1022 treatment on diploid clones. The diploid hCEC clone or hMEC cells was pretreated with the cell
1023 death inhibitors for 2 hours, followed by a one-hour exposure to 50 μM H_2O_2 without the inhibitors.
1024 Then the cells were released from H_2O_2 and incubated with cell death inhibitors for 24 hours before
1025 the detection of cell viability.
1026
1027 To examine the role of NAD+ depletion during PARP1-mediated cell death, the hCEC clones were
1028 pre-cultured in medium with and without the supplementation of 180 μM NMN (Sigma-Aldrich,
1029 N3501) for 24 hours before H_2O_2 treatment.
1030
1031 To compare cell resistance to alkylating agents, near-diploid and aneuploid hCEC clones, either with
1032 or without PARP1 overexpression, were treated with 62.5 μM MNNG (Selleck Chemicals, E0157)
1033 for 24 hours before the detection of cell viability.
1034
1035 To compare cell resistance to UV radiation, the hCEC clones were plated on 6-well plates to reach
1036 a comparable confluent level of 60% when cells were irradiated with UV. On the second day, the
1037 cells were washed with PBS, followed by UV irradiation (50 J/m2, cells were in PBS) with the lid
1038 removed (UV Stratalinker 2400). Then PBS was replaced with fresh media and cells were cultured
1039 in a humidified environment at 37℃ and 5% CO_2 for 5 days. The confluent cells were split during
1040 this period. After the 5-day release, the cell number ratios of UV-treated cells to untreated cells (the
1041 relative viability) for each clone were compared.
1042
1043 To assess DNA damage repair in diploid and aneuploid cells, two near-diploid (D23 and D29) and
1044 two high-aneuploidy (A20 and A29) hCEC clones were transiently exposed to various genotoxic
1045 agents to induce DNA damage through distinct mechanisms, including H_2O_2 (50 μM, 1 hour), MNNG
1046 (125 μM, 1 hour), camptothecin (Selleck Chemicals, S1288, 10 μM, 2 hours), etoposide (Selleck
1047 Chemicals, S1225, 200 μM, 1 hour), pyridostatin (Selleck Chemicals, S7444, 20 μM, 2 hours),
1048 doxorubicin (Selleck Chemicals, S1208, 10 μM, 2 hours) and bleomycin (Selleck Chemicals, S1214,
1049 50 μM, 1 hour).
1050
1051 To examine the effect of lysosome inhibitor Baf A1 on PARP1 expression and cell resistance to
1052 H_2O_2, hCECs (TP53WT and TP53KO) were incubated with 5 nM Baf A1 for 1 to 24 hours and then
1053 collected for western blot, or treated with 200 μM H_2O_2 for 24 hours to compare their resistance to
1054 H_2O_2.
1055
1056 **Brightfield and widefield fluorescence imaging**
1057 The brightfield images of cells before and after H_2O_2 treatment were acquired using the EVOS
1058 M5000 imaging system. To distinguish between live and dead cells using fluorescence imaging,
1059 the cells were first stained with 2.5 μM SYTO 13 (or 1 μg/mL Hoechst 33342) and 3 μg/mL PI for

15 minutes in the dark. Then they were imaged using the Incucyte S3 system (for SYTO 13 and PI) or the Cytation Cell Imaging Reader (for Hoechst 33342 and PI). In the case of the Incucyte S3 system, the signal from SYTO 13 and PI was acquired using the Green cube (441-481 nm Ex; 503-544 nm Em) and the Red cube (567-607 nm Ex; 622-704 nm Em), respectively. For the Cytation Cell Imaging Reader, the signal from Hoechst 33342 and PI was acquired using the DAPI cube (377 nm Ex; 447 nm Em) and the Texas Red cube (586 nm Ex; 647 nm Em), respectively. Live cells were identified as being SYTO 13 (or Hoechst 33342) positive and PI negative, while dead cells were identified as being SYTO 13 (or Hoechst 33342) positive and PI positive. The brightness, contrast and size of the images were adjusted using Fiji software.

Measurement of relative cellular viability

To assess the relative viability of cells under drug treatment, two independent methods based on fluorescence imaging or flow cytometry were used. The relative viability (%) was calculated using the formula:

$$relative\ viability\ (\%) = \frac{Number\ of\ live\ cells\ under\ treatment}{Number\ of\ live\ cells\ without\ treatment} \times 100$$

To measure relative viability through fluorescence imaging, cells with and without treatment were stained with 1 μg/mL PI and 2.5 μM SYTO 13 for 15 minutes in the dark. The brightfield and fluorescence images of cells under different conditions were acquired using the Incucyte S3 system (brightfield channel, GFP channel for SYTO 13, and RFP channel for PI). Live cells were identified as being SYTO 13 positive and PI negative (GFP+ and RFP-), while dead cells were identified as being SYTO 13 positive and PI positive (GFP+ and RFP-). The counting of GFP+ and RFP+ cells for each image was performed using CellProfiler software. The number of live cells was determined by subtracting the count of RFP+ cells from the count of GFP+ cells. For mouse KP cancer cells, the cell confluence in the brightfield channel calculated by Incucyte S3 software was used as a representation of the number of live cells because the cells were too close to each other to accurately count the number of stained cells.

To measure relative viability through flow cytometry, cells with and without treatment were harvested by trypsinization. A known number of GFP+ cells were spiked into each sample as a reference, and cells were subsequently stained with 1 μg/mL PI for 10 minutes in the dark. The cell mixture was then analyzed using flow cytometry (SONY SA3800) to determine the cell number ratio of GFP- and GFP+ cells with exclusion of PI positive dead cells. The number of live cells for each condition was calculated using the following formula:

$$N\ of\ live\ cells = \frac{\%\ of\ GFP^{-}\ sample\ cells\ detected\ by\ flow\ cytometry}{\%\ of\ GFP^{+}\ reference\ cells\ detected\ by\ flow\ cytometry} \times N\ of\ GFP^{+} reference\ cells\ spiked\ in$$

1097 In Fig. S1C and S1D, the percentage of dead cells was used to represent the cell sensitivity to the
1098 treatment. To achieve this, cells were stained with 1 μg/mL PI and 1 μg/mL Hoechst 33342 for 15
1099 minutes in the dark. Then the counting of live cells (Hoechst 33342 positive and PI negative) and
1100 dead cells (Hoechst 33342 positive and PI positive) was based on flow cytometry using SONY
1101 SA3800 or fluorescence imaging using Cytation Cell Imaging Reader.
1102
1103 **Cell proliferation assay**
1104 To assess cell proliferation rate, cells were plated in multiwell plates to reach a confluent level of
1105 20% on the second day. The second day, the cells were provided with extra fresh medium, followed
1106 by the acquisition of brightfield images at regular intervals (every 4-6 hours) from multiple non-
1107 overlapping planes of view for each well using Incucyte S3 (10x objective) until the cells reached
1108 complete confluence. Cell confluence was quantified using the Incucyte basic quantification
1109 function. The confluence data was further processed using R studio to exclude confluence values
1110 below 20% or above 80%. The resulting confluence data was fitted using the GraphPad Exponential
1111 (Malthusian) growth model as follows:
1112 $$Y = Y_0 \times e^{k \times t}$$
1113 Doubling time, calculated as $ln(2)/k$, is the time needed for the cell population to double.
1114
1115 **Alkaline comet assay**
1116 DNA damage at the single-cell level, both before and after H_2O_2 treatment, including single-strand
1117 and double-strand DNA breaks, and apurinic and apyrimidinic sites, was detected by the alkaline
1118 comet assay. The assay principle relies on the ability of denatured cleaved DNA fragments to
1119 migrate out of the cell under the impact of an electric potential, while undamaged supercoiled DNA
1120 remains confined within the cell membrane when a current is applied. To perform this assay, cells,
1121 both with and without one-hour exposure to 50 μM H_2O_2, were collected by trypsinization, washed
1122 with cold PBS, and resuspended in cold PBS at a concentration of 100,000 cells/mL. Then 40 μL of
1123 the cell suspensions were mixed with 400 μL of molten 1% low melting temperature agarose (at
1124 37°C), and 40 μL of this mixture was immediately dropped onto 8-well hydrophobic printed slides
1125 (Electron Microscopy Sciences, 63422-11) which were pre-coated with 1% normal melting
1126 temperature agarose. The slides were left for 10 minutes at 4°C in the dark to allow the gel to
1127 solidify. Then the slides were immersed in pre-chilled lysis buffer (comprising 2.5 M NaCl, 100 mM
1128 EDTA, 10 mM Tris Base, 1% sodium lauryl sarcosinate, and 1% Triton X-100) for 45 minutes at 4°C
1129 in the dark, followed by immersion in a fresh alkaline solution, pH > 13, (consisting of 300 mM NaOH
1130 and 1 mM EDTA) for 45 minutes at room temperature in the dark. The slides were then transferred
1131 to a horizontal electrophoresis apparatus with the cold alkaline solution covering them.
1132 Electrophoresis was performed for 30 minutes at 4°C with a voltage set at about 1 V/cm x distance
1133 between electrodes (buffer volume was adjusted until the current was approximately 300 mA).
1134 Then the slides were immersed in 70% ethanol for 5 minutes. After overnight air drying, the slides
1135 were stained with SYBR Gold nucleic acid gel stain, rinsed with PBS, followed by confocal imaging

1136 (using a x4 objective and GFP channel of a Nikon spinning disk confocal microscope). The relative
1137 DNA contents in comet tails compared to the whole comets, quantified using CellProfiler software,
1138 was used to represent the degree of DNA damage.
1139
1140 **Detection of lipid peroxidation**
1141 To detect degrees of lipid peroxidation with or without H_2O_2 treatment, C11-BODIPY 581/591
1142 (Thermo Fisher, D3861), a lipid-soluble ratiometric fluorescent probe of lipid oxidation, was used to
1143 stain hCECs (5 μM for 45 minutes at 37℃ in the dark). The probes were integrated into the cellular
1144 membranes, mimicking the properties of natural lipids. Oxidation of the polyunsaturated butadienyl
1145 portion of the probes lead to a shift of the fluorescence emission peak from ~590 nm to ~510 nm,
1146 providing a method to measure cell antioxidant activity in lipid environments. After staining, the
1147 cells were washed with PBS and exposed to 50 μM H_2O_2 (or blank control) in fresh media for 30
1148 minutes. Then the cells were collected by trypsinization and the fluorescence emission ratio of 591
1149 nm to 510 nm emitted by the probes was measured using flow cytometry.
1150
1151 **Immunofluorescence**
1152 Coverslips were coated with cold DMEM containing 1% GelTrex (LDEV-free reduced growth factor
1153 basement membrane matrix) in a humidified environment at 37℃ with 5% CO_2 for at least one hour.
1154 Then the cells were plated on these pre-coated coverslips in 24-well plates. On the second day, the
1155 cells were treated with drugs indicated in the results and legends. After the treatment, the cells
1156 were washed with PBS, and then fixed in 4% paraformaldehyde solution in PBS for 10 minutes at
1157 room temperature and washed with PBS for 10 minutes. Fixed cells were permeabilized with 0.5%
1158 Triton X-100 in PBS for 20 minutes at room temperature and washed with PBS for 10 minutes. The
1159 cells were then blocked with the blocking solution (1 mg/mL BSA, 3% goat serum, 0.1% Triton X-
1160 100, and 1mM EDTA at pH 8.0, in PBS) for 1 hour at room temperature and washed with PBS twice.
1161 Then the cells were incubated with primary antibodies (see below) diluted in the blocking solution
1162 at 4℃ overnight, followed by three washes with PBS. Negative controls, used to assess nonspecific
1163 background, underwent a similar process but were incubated with the blocking solution without
1164 primary antibodies. Next, the cells were incubated with secondary antibodies (see below) diluted in
1165 the blocking solution for two hours at room temperature, followed by three washes with PBS. In
1166 case of Phalloidin staining, the cells were next incubated with DyLight 554 Phalloidin (Cell Signaling
1167 Technology, 13054) diluted 1:400 in PBS for 15 minutes, followed by PBS washing. The coverslips
1168 were mounted with Vectashield antifade mounting media containing DAPI (H-1200-10). Images
1169 were acquired using the Nikon spinning disk confocal microscope at a 100x objective, ensuring
1170 overexposure was prevented during imaging. The ratio of area-normalized NRF2 fluorescence
1171 intensity in the nuclei to that in the cytoplasm, the area-normalized γH2AX fluorescence intensity
1172 in the nuclei, and the area-normalized CEBPB fluorescence intensity in the nuclei (ratio of the total
1173 intensity to the area for each nucleus) were quantified using CellProfiler software. The NRF2

1174 primary antibody (Proteintech, 16396-1-AP) was diluted at 1:200, γH2AX primary antibody (Sigma,
1175 05-636) was diluted at 1:1000, and CEBPB primary antibody (Abcam, ab32358) was diluted 1:100.
1176 Invitrogen goat anti-rabbit (A11034) IgG secondary antibody conjugated with Alexa Fluor 488 was
1177 used for NRF2 and CEBPB primary antibodies and anti-mouse (A28175) IgG secondary antibody
1178 conjugated with Alexa Fluor 488 was used for γH2AX primary antibody, at a dilution of 1:1000.
1179
1180 **Western blot**
1181 A total of 1,000,000 cells were harvested by trypsinization, washed with cold PBS, and lysed in 100
1182 μL of RIPA lysis buffer (Abcam, ab156034) supplemented with the protease and phosphatase
1183 inhibitor cocktail (Thermo Scientific, 78441). To detect pADPr, the cells were treated with 2 μM PDD
1184 00017273 (a cell-permeable inhibitor of Poly(ADP-ribose) Glycohydrolase) for 1 hour before and
1185 during H_2O_2 treatment to suppress pADPr degradation. Then an equivalent number of cells were
1186 directly lysed in plates on ice using a specialized lysis buffer containing the inhibitors of PARP and
1187 PARG due to the rapid dynamic of PARP1 synthesis and degradation even after cell lysis [114]. This
1188 lysis buffer consisted of 50 mM Tris-HCl, pH 8.0, 100 mM NaCl, 1% Triton X-100, 5 mM MgCl2, 5
1189 mM Bond-Breaker TCEP solution, 1x protease and phosphatase inhibitor cocktail (Thermo
1190 Scientific, 78441), 1.6 μM ADP-HPD (Sigma-Aldrich, 118415), 1 μM olaparib (Cell Signaling, 93852),
1191 and 125 U/mL benzonase (Sigma-Aldrich, E1014).
1192
1193 The lysates were agitated for 30 minutes at 4℃, followed by high-level sonication for 5 minutes at
1194 4℃ (Diagenode Bioruptor Standard Sonication System, UCD-200). Then the lysates were
1195 centrifuged at 4°C and the supernatants were collected. Subsequently, the Pierce LDS buffer
1196 (Thermo Scientific, 84788) and the Bond-Breaker TCEP solution (Thermo Scientific, 77720) were
1197 added into the supernatants to reach concentrations as recommended by the manufacturers. The
1198 lysates were then boiled for 10 minutes at 80°C. After returning to room temperature, 15 uL of the
1199 lysates were loaded into wells of NuPAGE 4-12% Bis-Tris mini gels (Thermo Scientific, NP0323BOX)
1200 for electrophoresis, followed by transfer to either PVDF membranes (Bio-Rad, 1704274) using a
1201 semi-dry system (Trans-Blot Turbo transfer system, Bio-Rad, 1704150), or to nitrocellulose
1202 membranes (Bio-Rad, 1620212) using a tank transfer system (Mini Trans-Blot Cell, Bio-Rad,
1203 1703930), following the manufacturer's protocols. The membranes were then blocked with 5% non-
1204 fat milk in Tris-buffered saline (TBS) with 0.1% Tween-20 (TBST) for 1 hour at room temperature,
1205 followed by an overnight incubation with primary antibodies diluted in 2.5% BSA in TBS (see below)
1206 at 4°C. Subsequently, the membranes were washed three times with TBST and incubated with
1207 either fluorophore- or horseradish peroxidase (HRP)-conjugated secondary antibodies diluted in
1208 2.5% BSA in TBST for 2 hours at room temperature. Then the membranes were washed three times
1209 with TBST before signal detection. For fluorophore-conjugated secondary antibodies, the signal
1210 was directly detected using the Li-Cor Odyssey DLx imaging system. For HRP-conjugated
1211 secondary antibodies, the membranes were incubated with Pierce ECL Western Blotting Substrate

1212 (Thermo Scientific, 32106) in the dark for three minutes and then imaged using the Bio-Rad Gel Dox
1213 XR imaging system. Quantification of WB images was performed using Image J by calculating the
1214 signal derived from the indicated WB bands and subtracting the relative background. Normalization
1215 was performed relative to the indicate internal control protein. In the case of Reversine or AZ3146
1216 treated cells, normalization to the total percentage of aneuploid cells was performed.
1217
1218 The following antibodies and dilutions were used: TP53 (Santa Cruz, sc-126) at a dilution of 1:100,
1219 NRF2 (Cell Signaling Technology, D1Z9C) at a dilution of 1:1000, PARP1 (Proteintech, 13371-1-AP
1220 or Cell Signaling, 9542T) at a dilution of 1:1000, pADPr (Sigma-Aldrich, MABE1031) at a dilution of
1221 1:1000, γH2AX (Sigma-Aldrich, 05-636) at a dilution of 1:1000, H2AX (Cell Signaling Technology,
1222 2595) at a dilution of 1:1000, GAPDH (Santa Cruz, sc-47724) at a dilution of 1:10,000, vinculin
1223 (Sigma-Aldrich, V9131) at a dilution of 1:20,000, IRDye 680RD goat anti-mouse IgG secondary
1224 antibody (926-68070) at a dilution of 1:20,000, IRDye 800CW goat anti-rabbit IgG secondary
1225 antibody (926-32211) at a dilution of 1:20,000, HRP-conjugated goat anti-mouse IgG secondary
1226 antibody (ab205719) at 1:10,000, HRP-conjugated goat anti-rabbit IgG secondary antibody
1227 (ab205718) at 1:10,000.
1228
1229 **RNA sequencing and data processing**
1230 Cells were plated on 6-well plates one day before the collection. On the second day, the cells were
1231 examined to ensure their confluency level between 70% to 90%, with normal morphological
1232 characteristics. Then the cells were washed twice with PBS and promptly stored at –80°C. Total
1233 RNA was extracted using the PicoPure RNA Isolation kit (Life Technologies, Frederick, MD), which
1234 included an on-column RNase-free DNase I treatment (QIAGEN, Hilden, Germany), following the
1235 manufacturer's recommendations. To further purify the RNA for sequencing, the QIAGEN RNeasy
1236 Mini Kit (QIAGEN, 74106) was used. The concentration and integrity of the RNA were assessed
1237 using a 2100 BioAnalyzer (Agilent, Santa Clara, CA). Subsequently, sequencing libraries were
1238 constructed using the TruSeq Stranded Total RNA Library Prep Gold mRNA kit (Illumina, San Diego,
1239 CA) with an input of 250 ng RNA and a 13-cycle final amplification. The resulting libraries were
1240 quantified using High Sensitivity D1000 ScreenTape on a 2200 TapeStation (Agilent) and the Qubit
1241 1x dsDNA HS Assay Kit (Invitrogen, Waltham, MA). The samples were equimolarity pooled, and
1242 sequencing was carried out on an Illumina NovaSeq6000 SP 100 Cycle Flow Cell v1.5 in paired-end
1243 50 reads mode.
1244
1245 The total RNA-sequencing reads were mapped to the human genome hg38 using STAR (v2.7.7a)[115]
1246 with a 2-pass model. The hg38 reference sequence and RefSeq annotation were obtained from the
1247 UCSC table browser. The quantification of gene and transcript expression levels was performed
1248 using RSEM (v1.3.1)[116], which generated gene-level raw counts and fragments per kilobase of
1249 transcript per million mapped reads (FPKM) results in table format. The RNA RSEM data was

filtered to include genes with a median FPKM > 1 for downstream analyses. The expression change (Log2FC) of reversine- and AZ3146-treated hCECs compared to DMSO-treated hCECs were calculated using DESeqDataSetFromMatrix and DESeq functions in the R package DESeq2 (v1.34.0)[117], which was used in Fig. 2D, 6D, and Fig. S3B, with the mean for the control being set to zero. For hCEC clones with different degrees of aneuploidy, the raw counts table was normalized using DESeqDataSetFromMatrix, estimateSizeFactors and counts functions in the R package DESeq2, followed by Log2 transformed. The log2-transformed normalized RNA levels were fitted by aneuploidy degrees of hCEC clones with a linear model as the following formula:

$$RNA\ log2FC \sim \beta_0 + \beta_1 \times aneuploidy\ score$$

The t-value of aneuploidy coefficient β_1 was used to represent the association between RNA level and aneuploidy degree, as shown in Fig. 2F, 6E and Fig. S3C. A positive (negative) t-value represented the RNA expression of the certain gene increased (decreased) in hCEC clones with higher degree of aneuploidy.

The Log2FC of reversine/AZ3146-treated hCECs and the t-value of aneuploidy coefficient of hCEC clones were used in Fig. 5G, 6B and Fig. S5B-D. For PCA of RNA expression levels for lysosome or proteasome genes in hCEC clones shown in Fig. 5F, the raw count table of all genes obtained from RNAseq was pre-processed using the variance stabilizing transformation function in the DESeq2 package. Then 121 lysosome genes or 46 proteasome genes, as defined by the Kyoto Encyclopedia of Genes and Genomes (KEGG), were used to generate the PCA plot using the plotPCA function in the DESeq2 package. To assess the statistical significance of group separation in PCA plots, we performed permutation tests with 10,000 permutations. For each permutation, we calculated the mean Euclidean distance between groups in PC1-PC2 space as the test statistic. The p-value was determined as the fraction of permuted statistics that exceeded the observed test statistic. This analysis was implemented using custom R scripts with the vegan package (v2.6-4). The separation between diploid and aneuploid groups was considered significant when the permutation test p-value < 0.05.

Analysis of published transcriptome data

The RNA-sequencing reads for TP53WT RPE1 cells treated with DMSO, reversine, Baf A1 or MG132 were downloaded from the Gene Expression Omnibus (GSE60570). The RNA-sequencing reads for TP53KO RPE1 cells treated with DMSO or reversine were downloaded from GSE188644. These raw sequencing reads were aligned using STAR, quantification using RSEM, and differential expression analysis using DESeq2, as described in the preceding section. The gene expression changes (Log2FC) were used to calculate the correlation in Fig. 5G and generate the heatmap in Fig. 6A and Fig. S5B-C. The raw counts table was normalized using the DESeq2, followed by Log2 transformed. The log2-transformed normalized PARP1 levels were compared in cells treated with different drugs, with the mean for the control being set to zero (Fig. 2D, Fig. 5H, Fig. S5H).

The Log2-transformed normalized PARP1, TIMELESS, or CEBPB RNA levels in HCT116 treated with DMSO and reversine were obtained from the supplementary table 7 of Cohen-Sharir et al., 2021[111], which were used in Fig. 2D, 6D and Fig. S3B, with the mean for the control being set to zero. The Log2FC of PARP1 RNA levels in aneuploid clones generated using MMCT, compared to their near-diploid controls, were obtained from supplementary table 2 of Dürrbaum et al., 2014[29], which were used in Fig. S2I. The Log2-transformed transcript per million (TPM) of PARP1 and CEBPB in CCLE cancer cell lines were obtained from Depmap portal[118,119] (Expression public 21Q4), which were used in Fig. 4B-C, Fig. S6C, Fig. 6K. The FPKM of PARP1 in TCGA COREAD samples (n = 597) were obtained from the Human Protein Atlas, which were used in Fig. 4K. For CCLE cell lines, the PARP1 SCNA (Log2, obtained from Depmap portal, 21Q4) was substrate from the PARP1 RNA levels (Log2) to normalize the copy number change. For TCGA COREAD samples, the patients with PARP1 DNA gain or loss were removed from the analysis (absolute SCNA value ≥ 0.05). To study the impact of CEBPB copy number change on PARP1 expression changes, TCGA COREAD samples without PARP1 copy alterations were classified based on CEBPB copy number status (diploid, gain, or amp, defined by cBioPortal). The PARP1 expression profile of each group is shown in Fig. S6A.

The PARP1 RNA levels of paired and unpaired primary and metastatic tumors were downloaded from Gene Expression Omnibus (GSE131418)[52]. For the unpaired tumors, COREAD patients were separated into a discovery cohort (MCC dataset with 333 primary tumors and 184 metastases) and a validation cohort (Consortium dataset with 545 primary tumors and 72 metastases). The probe-level raw data generated via Rosetta/Merck human RSTA custom Affymetrix 2.0 microarray was read using ReadAffy function and the robust multichip average (RMA) expression was calculated using rma function in the affy package (v1.72.0)[120], including background correction, normalization, and expression calculation (Log2). Five probes for PARP1 were selected and their normalized levels in different samples were shown in Fig. S4E. The normalized levels of probe AK225654at in different samples were shown in Fig. 4N. For the paired tumors, the metastases profiles were normalized to the paired primary as processed by Zhang et al.[121]. In brief, the probe with the highest variability across patients for each gene (by SD applied to log2-transformed expression values) was selected to represent the gene in the dataset. Then the log2-transformed expression values for each metastasis expression profile were centered on its primary pair, with the values for the primary pair being set to zero. Then, the centered expression values were divided by the SD across the centered metastasis and primary profiles. The normalized expression values of PARP1 were used in Fig. 4M.

The following datasets from Gene Expression Omnibus were used to compare PARP1 or CEBPB RNA expression change in Baf A1-treated cells compared with that in DMSO-treated controls: RPE1 treated with 0.1 μM Baf A1 for 6 hours (n = 3; data from GSE60570, see above)[28], HCT116 treated with 5 nM Baf A1 for 48 hours (n = 2; data from GSE150523) [53]. HEK293T treated with 10 nM Baf

1327 A1 for 24 hours (n = 3; data from GSE141507)[54]. HeLa cells were treated with 15 nM Baf A1 for 24
1328 hours (n = 2; data from GSE16870)[55]. The following datasets from Gene Expression Omnibus were
1329 used to compare PARP1 RNA expression change in Bortezomib- or MG132-treated cells compared
1330 with that in DMSO-treated controls: RPE1 cells treated with 1 μM MG132 for 24 hours (n = 3, data
1331 from GSE60570, see above)[28]. HCT116 treated with 5 nM bortezomib for 6 hours (n = 2, data from
1332 GSE95513)[56], 100 nM bortezomib for 3 hours, or 20 μM MG132 for 3 hours (n = 4, data from
1333 GSE165325)[58]. iPSC-derived endothelial cells (SCVI-100 and SCVI-114) or primary human aortic
1334 endothelial cells treated with 2 nM bortezomib for 72 hours (n = 1, data from GSE217898)[57]. The
1335 log2-transformed normalized PARP1 levels were directly obtained using the online analysis tool
1336 (GEO2R) of Gene Expression Omnibus, with the mean for the controls being set to zero.
1337
1338 **Liquid-chromatography mass spectrometry and data processing**
1339 The cell pellets were lysed using the following buffer: 8 M urea, 100 mM Tris, pH = 8.5, 10 mM TCEP,
1340 and 40 mM CAA (150 μL per sample) and sonicated in a probe sonicator for 1 × 5 s cycle at
1341 amplitude of 50%. After sonication, the lysates were incubated for 30 min at 56°C in a thermoshaker
1342 at 1000 rpm. Insoluble debris was removed by centrifugation for 5 minutes at 16,000 × g. Protein
1343 concentrations were measured using the A280 method, and the proteins were subsequently
1344 digested with trypsin at 50:1 (w/w) ratio at 37°C (lysates were diluted sixfold with 20 mM Tris, pH
1345 = 8 prior to digestion). After digestion, the samples were acidified with 10% FA to a final
1346 concentration of 0.5% FA and centrifuged to remove undigested material. The resulting peptides
1347 were desalted using tC18 Waters SepPak cartridges, and eluates were dried on a speedvac.

1348 50 μg of the digest from each sample were solubilized in 20 μL of 50 mM HEPES buffer pH = 8.5.
1349 Then 8 μL of 12.5 mg/mL TMTPro reagent were added, and the labeling reaction was allowed to
1350 proceed for 30 min at room temperature. Excess label was quenched by adding 40 μL of 500 mM
1351 ABC buffer for 30 min at 37°C. Labeled peptides from different samples were mixed to create two
1352 16-plex TMT batches, which were then desalted using tC18 SepPak cartridges, concentrated using
1353 a speedvac, and fractionated offline.

1354 500 μg of peptides were fractionated using a Waters XBridge BEH 130A C18 column (3.5 μm, 4.63
1355 × 250 mm) on an Agilent 1260 Infinity series HPLC system operating at a flow rate of 1 mL/min
1356 with three buffer lines: buffer A consisting of water, buffer B of acetonitrile, and buffer C of 100 mM
1357 ammonium bicarbonate. Peptides were separated by a linear gradient from 5% B to 35% B in 62
1358 min followed by a linear increase to 60% B in 5 min, and ramped to 70% B in 3 min. Buffer C was
1359 constantly introduced throughout the gradient at 10%. Fractions were collected every 60 seconds.
1360 Fractions from 30 to 64 were used for LC-MS/MS analysis.

The LC separation was performed online on EvosepOne LC (Bache et al., 2018) utilizing Dr Maisch C18 AQ analytical column (1.9 µm, 0.15 x 15 mm, Cat# EV-1106). Peptides were gradiently eluted from the column directly to an Orbitrap HFX mass spectrometer using a 44-minute evosep method (30SPD) at a flow rate of 220 nL/min. The mass spectrometer was operated in a data-dependent acquisition mode (DDA). High-resolution full MS spectra were acquired with a resolution of 120,000, an AGC target of 3e6, a maximum ion injection time of 100 ms, and scan range of 400–1600 m/z. Following each full MS scan, 20 data-dependent HCD MS/MS scans were acquired at the resolution of 60,000, AGC target of 5e5, maximum ion time of 100 ms, one microscan, 0.4 m/z isolation window, normalized collision energy of 30, fixed first mass 100 m/z, and dynamic exclusion for 45 s. Both MS and MS2 spectra were recorded in profile mode.

The MS data were analyzed using MaxQuant software (v1.6.15.0)[122] and searched against the SwissProt subset of the human UniProt database containing 20,430 entries. Database search was performed in Andromeda[123] integrated in the MaxQuant environment. A list of 248 common laboratory contaminants included in MaxQuant was also added to the database as well as reversed versions of all sequences. For searching, the enzyme specificity was set to trypsin with the maximum number of missed cleavages set to 2. The precursor mass tolerance was set to 20 ppm for the first search used for nonlinear mass recalibration and then to 6 ppm for the main search. Oxidation of methionine was searched as variable modification; carbamidomethylation of cysteines was searched as a fixed modification. TMT labeling was set to lysine residues and N-terminal amino groups, and corresponding batch-specific isotopic correction factors were accounted for. The FDR for peptide, protein, and site identification was set to 1%, and the minimum peptide length was set to 6. To transfer identifications across different runs, the 'match between runs' option in MaxQuant was disabled. Only precursors with minimum precursor ion fraction (PIF) of 75% were used for protein quantification. Match between runs option was enabled and RAW TMT reporter ion intensities of peptide features were used for subsequent data analysis in MSstatsTMT[124]. Subsequent data analysis was performed in either Perseus[125] or R for statistical computing and graphics.

The log2-transformed normalized protein levels were fitted by aneuploidy degrees of hCEC clones with a linear model as the following formula:

$$protein\ log2FC \sim \beta_0 + \beta_1 \times aneuploidy\ score$$

The t-value of aneuploidy coefficient β_1 was used to represent the association between protein level and aneuploidy degree, as shown in Fig. 2G. A positive (negative) t-value represented the protein expression of the certain gene increased (decreased) in hCEC clones with higher degree of aneuploidy.

Analysis of published proteome data

The proteome changes of the aneuploid clones, generated via MMCT, compared to their near-diploid controls, were obtained from supplementary table 1 of Stingele et al., 2012[31]. To compare the protein levels of these clones, stable isotope labeling with amino acids in cell culture (SILAC) was used, followed by high-resolution mass spectrometry and quantified the proteome to a depth of ~6000 proteins. This data was used in Fig. 2I and Fig. S2I. The proteome data of CCLE cancer cell lines were obtained from Depmap portal[118,119] (Expression public 21Q4), which was used in Fig. 4B-C.

Resistance of cancer cell lines to olaparib

The data of cancer cell sensitivity to the PARP1 inhibitor Olaparib were obtained from Depmap portal. The following three independent drug screening datasets were used: PRISM repurposing primary screen[126] (olaparib ID: BRD-BRD-K02113016-001-15-4, n = 547 cell lines), GDSC dataset[127] (olaparib ID: GDSC21017, n = 506 cell lines) and CTD2 dataset[128] (olaparib ID: CTRP411867, n = 756 cell lines). For the PRISM dataset, the drug effect log2FC data was downloaded, while the AUC values of olaparib in the GDSC and CTD2 datasets were used. The Z-values of these values (Log2FC or ACU) in each dataset were calculated and used to generate the box plot in Fig. S6B. A higher Z-value represents an increased level of resistance to olaparib.

Patients' survival analysis using TCGA

The TCGA survival data of COREAD patients was downloaded from the Human Protein Atlas. Based on the FPKM value of PARP1, patients were classified into two expression groups (PARP1-Low and PARP1-High) to yield maximal difference with regard to survival between the two groups at the lowest log-rank p-value (n = 124 patients with low PARP1 and n = 473 patients with high PARP1). The prognosis of each group of patients was examined by Kaplan-Meier survival estimators, and the survival outcomes of the two groups were compared by log-rank tests.

Knockdown, knockout, and overexpression

The PARP1 overexpression and PARP1, GPX1, CAT knockdown plasmids, along with their respective controls, were used to generate lentivirus with packaging and envelope plasmids. hCECs and COREAD cancer cells were transduced with the lentivirus, followed by selection using puromycin (1.5 μg/mL for hCECs and 3 μg/mL for COREAD cancer cells with shRNA) or blastomycin (10 μg/ml for hCECs and COREAD cancer cells with pHAGE-CMV-blast) until the uninfected control cells died. For the co-expression of the shRNA targeting the 3'-UTR region of PARP1 transcripts and shRNA-resistant PARP1 cDNA, the PARP1-overexpressing cells were transduced with shPARP1-1, followed by puromycin selection. To get rid of unspecific impacts of lentiviral infection and selection, all cells in Fig. 3G, including those lacking shPARP1-1 or PARP1 OE, and those exclusively expressing shPARP1-1 or PARP1 OE, were additionally infected with the control virus for a total of two rounds of infection and selection. For example, the cells without

1436 shPARP1-1 or PARP1 OE were subsequently infected and selected for pHAGE-EV and shNC. The
1437 effects of PARP1 overexpression and knockdown were confirmed using western blot. To achieve
1438 physiological levels of PARP1 expression, TP53WT or TP53KO hCECs were transduced with a
1439 lentiviral Tet-On system for doxycycline-inducible PARP1. Following hygromycin selection, cells
1440 were treated with 1 μg/mL doxycycline for 1-2 days to induce PARP1 expression before validation
1441 by Western blot or assessment of H2O2 sensitivity. To establish stable co-expression of PARP1
1442 and TIMELESS in hCEC A29 clones, cells were first transduced with pHAGE-PARP1-puro or pHAGE-
1443 EV-puro lentivirus and selected with puromycin. The stable cells were then transduced with pHAGE-
1444 TIMELESS-blast or pHAGE-EV-blast lentivirus, followed by blasticidin selection. For CEBPB
1445 overexpression, cells were transduced with lentivirus generated from pBABE-puro LAP2 (Addgene
1446 #15712) or pBABE-puro empty vector. For NRF2, PARP1, PARP2, and MIF knockout, lentiviral
1447 particles were produced by co-transfecting HEK293T cells with LentiCRISPR-V2-FE-puro plasmids
1448 carrying target-specific sgRNAs or non-targeting control (sgNC), along with lentiviral packaging and
1449 envelope plasmids. Target cells were transduced with the lentivirus and selected with puromycin.
1450
1451 **Cancer cells expressing luciferase and GFP or mCherry**
1452 For the comparison of ROS sensitivity of near-diploid and high-aneuploidy colon cancer cell lines
1453 using the multicolor competition assay, as well as the observation of intravenously injected cancer
1454 cells in living mice (see below), we lentivirally transduced two near-diploid colon cancer cells (DLD1
1455 and HCT116) and one high-aneuploid colon cancer cells (HT29) with either pCDH-EF1a-eFFly-eGFP
1456 (Addgene, 104834) or pCDH-EF1a-eFFly-mCherry (Addgene, 104833). After infection, the GFP-
1457 positive or mCherry-positive cells were sorted using flow cytometry-based cell sorting (FACS) on
1458 the SONY SH800 cell sorter with a 130 μm sorting chip.
1459
1460 **Multicolor competition assay**
1461 To investigate the impact of PARP1 knockdown or overexpression on the sensitivity of colon cell
1462 lines to H_2O_2, control cancer cells, labeled with either GFP or mCherry, were mixed with PARP1-
1463 knockdown or PARP1-overexpressing cells labeled with the complementary fluorescent marker
1464 (i.e., mCherry or GFP) in equal cell numbers. The six combinations examined were as follows:
1465 HCT116-GFP with shNC and HCT116-mCherry with shPARP1-1, HCT116-mCherry with shNC and
1466 HCT116-GFP with shPARP1-1, DLD1-GFP with shNC and DLD1-mCherry with shPARP1-1, DLD1-
1467 mCherry with shNC and DLD1-GFP with shPARP1-1, HT29-GFP with pHAGE-EV and HT29-mCherry
1468 with pHAGE-PARP1, HT29-mCherry with pHAGE-EV and HT29-mCherry with pHAGE-PARP1. The
1469 mixed cells were cultured in the regular medium, with and without the addition of 2mM H_2O_2, for a
1470 24-hour incubation period. Then the ratios of GFP-labeled and mCherry-labeled cells within each
1471 combination were quantified using flow cytometry (SONY, SA3800). To assess the impact of H_2O_2
1472 treatment, these ratios were normalized to those obtained from control groups that were not
1473 exposed to H_2O_2.

1474

1475 **Assessing metastatic potential through in vivo assay**

1476 The animal procedures were approved by the New York University Grossman School of Medicine's
1477 Institutional Animal Care and Use Committee (IACUC). All the procedures are conducted in facilities
1478 approved by the Association for Assessment and Accreditation of Laboratory Animal Care
1479 International (AAALAC).

1480

1481 To assess dissemination potential, luciferase-expressing human colon cancer cells (DLD1 and
1482 HCT116 with shNC or shPARP1-1, HT29-EV, and SW498) were intravenously injected into
1483 immunodeficient NOD.Cg-Prkdc^{scid} Il2rg^{tm1Wjl}/SzJ (NSG) mice. For immune-competent studies,
1484 luciferase-expressing KaryoCreate-induced aneuploid mouse KP lung cancer cells (sgMinSat5)
1485 with empty expression or PARP1 overexpression vectors were injected into B6 Albino mice. Tumor
1486 progression was monitored by bioluminescence imaging every two weeks until the pre-established
1487 endpoint.

1488

1489 For the intravenous injection, cancer cells were collected through trypsinization, followed by two
1490 washes with cold PBS and suspension in cold PBS at a concentration of 1,000,000 cells/mL. Then
1491 200,000 cancer cells in 200 μL PBS were intravenously injected (via tail vein) into female NSG or B6
1492 Albino mice aged 7-9 weeks, using a 1 mL syringe with a 30G, 0.3 x 13mm needle. Each type of
1493 cancer cell was introduced into at least five mice. Continuous monitoring of the mice's condition
1494 was performed throughout the procedures and up to 1-2 hours after the injection.

1495

1496 For in vivo bioluminescence imaging, the mice were anesthetized via inhalation with the oxygen
1497 level regulator set between 1-2 L/min and the isoflurane vaporizer set at 2.5-5% for induction and
1498 1.5–3% for maintenance. The D-luciferin substrate (150 mg/kg) was administered to mice via
1499 intravitreal injection using a 0.5 mL insulin syringe, 28 G needle. Then the imaging was performed
1500 using a bioluminescence imaging (BLI) scanner (IVIS Lumina XRMS In Vivo Imaging System). For
1501 data analysis, regions of positive signal were defined for each mouse while carefully excluding the
1502 ears and nose. The total luminescent flux (p/sec) within the regions of positive signal was
1503 quantified and normalized to the initial levels immediately following intravenous injection. For mice
1504 which reached the pre-established endpoint in the middle of the observation window (10 weeks),
1505 they are labeled by crosses in the figure and their last total flux signals were used for statistical
1506 analysis for the later time points.

1507

1508 To compare tumor growth between aneuploidy states in immune-competent environments, KP
1509 lung cancer cells were transduced with sgMinSat5 (high-aneuploidy) or sgRosa26 (low-aneuploidy)
1510 KaryoCreate vectors. Cells were harvested at subconfluency, washed with PBS, and resuspended
1511 at 1×10^6 cells/mL. Each mouse received 2×10^5 cells via tail vein injection. Tumor volumes were

quantified using MRI. For MRI quantification, mice were anesthetized with isoflurane, and lung fields were scanned using a BioSpec USR70/30 horizontal bore system (Bruker) to obtain 16 consecutive sections. MRI signal acquisition was gated to cardiac and respiratory cycles to minimize motion artifacts. Whole lung tumor volumes were quantified from volumetric measurements using 3D Slicer software.

Fluorescence-activated cell sorting based on PARP1 levels

To sort cells based on their PARP1 expression levels, 60,000,000 cells were collected through trypsinization, followed by a wash with cold PBS and fixation with 10 mL of 2% paraformaldehyde solution in PBS for 7 minutes at room temperature. After a wash with cold PBS, the cells were suspended in 10 mL of 90% cold methanol and incubated for 10 minutes at 4℃. Then the cells were washed with 10 mL of cold 1% BSA in PBS and blocked with 10 mL of 3% BSA in PBS for 45 minutes at 4°C in the dark. Subsequently, the cells were incubated with 6 mL of CoraLite 488-conjugated PARP1 monoclonal antibody (Proteintech, CL488-66520) at a concentration of 2 μg/mL in 1% BSA in PBS for 60 minutes at 4°C in the dark. Then the cells were washed three times with cold 1% BSA in PBS and resuspended in cold 1% BSA in PBS at a concentration of 5,000,000 cells/mL for sorting.

For the fluorescence-activated cell sorting, the SONY SH800 cell sorter with a 100 μm sorting chip was used. After excluding debris (gate 1: X-axis: FSC-A, Y-axis: BSC-A) and doublets (gate 2: X-axis: FSC-A, Y-axis: FSC-H), two gates above and below the diagonal line of the main populations on the plot of PARP1 intensity (FITC-A) versus cell size (BSC-A), representing PARP1-low and PARP1-high populations, respectively, were chosen, with each selected population comprising ~10% of the total cell count. After collection of the PARP1-low and PARP1-high cells, they were centrifuged to remove the supernatant. The cell pellets were stored at -80°C.

Genome-wide CRISPR screen

To unbiasedly identify genes that modulate PARP1 expression, we conducted two independent, fluorescence-activated cell sorting (FACS)-based genome-wide CRISPR screens. The cellular level of PARP1 served as the readout in these screens. The sensitivity of PARP1 antibody was validated using PARP1-overexpressed cells, PARP1-knockdown cells, and hCEC clones with known different levels of PARP1 expression. For each screen replicate, 60,000,000 hCEC cells were infected with a library of lentiviruses harboring 94,335 sgRNAs targeting 19,026 protein-coding human genes at a multiplicity of infection (MOI) lower than 1 (maintaining a representation ~450 per gRNA). After puromycin selection and a brief expansion, the cells were divided into two or three technical replicates (60,000,000 cells for each technical replicates), fixed and immunostained with the fluorophore-conjugated PARP1 antibody, and sorted based on PARP1 protein expression levels (see above). The sorting process resulted in approximately 4 million cells per group (two groups: PARP1-high or PARP1-low) in each technical replicate (two or three technical replicates for each

1550 biological replicate, two biological replicates in total), accounting for approximately 10% of all cells.
1551 To ensure that the FACS-based readout of PARP1 level was highly specific and sensitive, we
1552 validated the antibody using PARP1-overexpressed cells, PARP1-knockdown cells, and hCEC
1553 clones with known different levels of PARP1 expression (Fig. 5B).
1554
1555 The genomic DNA was then extracted from the sorted cells with low or high PARP1, and the
1556 unsorted cells as control. The following procedure shared by Neville Sanjana Lab was used for
1557 genomic DNA extraction from 40,000,000 cells. For different amounts of cells, the quantities were
1558 scaled proportionally. In a 15 mL conical tube, 6 mL of NK Lysis Buffer (50 mM Tris, 50 mM EDTA,
1559 1% SDS, pH 8) and 30 µL of 20 mg/mL Proteinase K (Qiagen, 19131) were added to the cell sample
1560 and incubated at 55 °C for 24 hours. Then 30 µL of 10 mg/mL RNAse A (Qiagen, 19101) was added
1561 to the lysed sample, which was then inverted 25 times and incubated at 37 °C for 30 minutes.
1562 Samples were cooled on ice before addition of 2 mL of pre-chilled 7.5 M ammonium acetate
1563 (Sigma-Aldrich, A1542) to precipitate proteins. subsequently, the samples were vortexed at high
1564 speed for 20 seconds and then centrifuged at ≥ 4,000 x g for 10 minutes. After the spin, a tight
1565 pellet was visible in each tube and the supernatant was carefully decanted into a new 15 mL conical
1566 tube. Then 6 mL of 100% isopropanol was added to the tube, inverted 50 times and centrifuged at
1567 ≥4,000 x g for 10 minutes. Genomic DNA was visible as a small white pellet in each tube. The
1568 supernatant was discarded, 6 mL of freshly prepared 70% ethanol was added, the tube was inverted
1569 10 times, and then centrifuged at ≥4,000 x g for 1 minute. The supernatant was discarded by
1570 pouring; the tube was briefly spun, and remaining ethanol was removed using a P200 pipette. After
1571 air drying for 10-30 minutes, the DNA changed appearance from a milky white pellet to slightly
1572 translucent. At this stage, 500 µL of TE buffer was added, the tube was incubated at 65 °C for 1
1573 hour and at room temperature overnight to fully resuspend the DNA. The next day, the gDNA
1574 samples were vortexed briefly. The gDNA concentration was measured using a Nanodrop (Thermo
1575 Scientific).
1576
1577 The DNA of sgRNAs was extracted from the genomic DNA using a 26-cycle PCR reaction. Each
1578 PCR reaction consisted of 4 µg genomic DNA, 0.5 µM primers and 1 unit of Q5 DNA polymerase
1579 (NEB, M0491L) in a 100 µL PCR reaction volume. All extracted genomic DNA from the sorted cells
1580 and the same amount of genomic DNA from the unsorted cells were used for this round of PCR.
1581 Then all the PCR products from the same sample were pooled together, and 100 µL of PCR product
1582 for each sample was gel purified and eluted in 35 µL of the elution buffer. The concentration of the
1583 purified PCR product was determined using the Qubit dsDNA quantification assay kit (Thermo
1584 Scientific, Q32854), and 400 ng of the purified PCR products were used in a 5-cycle PCR reaction
1585 to add adaptors. Next, 5 µL of PCR product for each sample was used in a 7-cycle PCR reaction to
1586 introduce the standard Illumina sequencing primers and unique sample barcodes. The
1587 concentrations of PCR products were determined by analyzing the band intensities after gel

electrophoresis. Equimolar PCR products from the sorted samples and two-fold PCR products from the control samples were mixed together, followed by the gel electrophoresis purification using the Nucleospin Gel and PCR Clean-UP kit. The sequence of all the primers is included in Table 6.

The prepared library was sequenced on an Illumina NextSeq 500 in single-end mode (1 X 75 cycles). Approximately 10 million reads were obtained for each sorted sample and about 20 million reads were obtained for each control sample. The raw reads were trimmed using cutadapt [129] with the adaptor sequence ACGAAACACC. Subsequently, the trimmed reads were processed to generate a count table using the count function of the MAGeCK package [130] and calculate the enrichment scores (MAGeCK values) at the gene level using the mle function of the MAGeCK package. The sgRNAs targeting positive regulators of PARP1 expression (PARP1 activators) were enriched in the PARP1-low cells compared to the unsorted cells, while sgRNAs targeting negative regulators of PARP1 expression (PARP1 suppressors) were enriched in the PARP1-high cells. To plot the relation of MAGeCK scores in the PARP1-low and these in the PARP1-high population (Fig. 5C), genes exclusively enriched in the PARP1-high population (the 2nd quadrant) and in the PARP1-low population (the 4th quadrant) are depicted in red and green, respectively. The intensity of the dots represents gene-level FDR-adjusted p-values within their respective populations (-Log10). For genes located in the other two quadrants, their p-values were set to one.

Enrichment analysis using Ingenuity Pathway Analysis (IPA)

The CRISPR screen identified 269 PARP1 activators (genes whose knockout decreased PARP1 expression) and 155 PARP1 suppressors (genes whose knockout increased PARP1 expression) using a false discovery rate (FDR) cutoff of < 0.1 and a MAGeCK beta value cutoff of > 0.5. The two sets of the filtered genes were used as the input for the pathway analysis performed using QIAGEN IPA (Expression analysis of the IPA core analysis with the measurement type being expr other). Enriched pathways with B-H p-values smaller than 0.1 are shown.

To identify the genes whose expression change in aneuploid cells may contribute to PARP1 downregulation, we searched for the PARP1 activators downregulated in aneuploid cells and the PARP1 suppressors upregulated in aneuploid cells (referred to as aneuploid-associated PARP1 regulators). For the MPS1i-induced aneuploid cells, RNA log2FC was used, while the t-values of aneuploidy coefficient was used for hCEC clones (see above). Genes with an FDR larger than 0.1 or the absolute Z-scores ≤ 0.5 were considered unchanged. Only the genes that exhibited expected expression changes in at least two aneuploidy models, without conflicted changes in different models were considered as aneuploid-associated PARP1 regulators, which were used as the input for the pathway analysis as described above.

Identification of potential PARP1 regulators contributing to its downregulation in aneuploid cells

Decreased PARP1 RNA in aneuploid cells and cells with lysosomal dysfunction suggested altered PARP1 transcription. We aimed to identify transcription factors (TFs) responsible for PARP1 transcriptional dysregulation in these settings. We integrated our PARP1 CRISPR screen results with TF databases[59–61] to identify PARP1-regulating TFs. We used three published databases: the GeneHancer database from GeneCards, TFLink, and AnimalTFDB[59–61]. All potential PARP1 TFs from these databases were merged for further analysis.

The TFs were filtered based on our PARP1 screen results into two groups: TFs promoting PARP1 expression (promoters, enriched in PARP1-low cells or depleted in PARP1-high cells, $p<0.05$) and TFs suppressing PARP1 expression (suppressors, depleted in PARP1-low cells or enriched in PARP1-high cells, $p<0.05$). We then examined TF expression changes in aneuploid and lysosome-dysfunction cells, identifying downregulated promoters and upregulated suppressors ($p<0.05$). This analysis identified CEBPB as a potential PARP1 suppressor, showing consistent upregulation across aneuploid and lysosome-dysfunction models.

ENCODE CEBPB ChIP-Seq data

The CEBPB ChIP-Seq data (bigWig files for signal p-values and bigBed narrowPeak files for IDR thresholded peaks) for A549 cells treated with or without CEBPB agonist dexamethasone (1 hour) were downloaded from ENCODE database (ENCSR625DZB). The signal p-values and IDR thresholded peaks near PARP1 TSS were visualized using IGV software (V2.17.4).

cGAMP detection

We quantified cGAMP in conditioned media from D23, D29, A20, and A21 hCEC clones using an immunoassay kit (Arbor Assays, Michigan, USA). Standard curves were generated using the kit's recombinant cGAMP standard. 1×10^6 cells were plated, and positive controls were transfected with 1 µg cGAS agonist G3-YSD (InvivoGen, San Diego, CA) using Lipofectamine 2000. Conditioned media were collected 48 hours after seeding. Samples (50 µL conditioned medium), standards, and positive controls were added to pre-coated assay plates. Detect X 2',3'-cGAMP conjugate and antibody (25 µL each) were added to sample wells and incubated with rotation for 2 hours at room temperature. Wells were washed three times with 1X wash buffer. TMB substrate (100 µL) was added and incubated for 30 minutes at room temperature in darkness. Stop solution (50 µL) was added, and absorbance was measured at 450 nm using a plate reader.

Analysis of published scRNA-Seq and CRISPRa Perturb-Seq data

The raw unique molecular identifier (UMI) counts, cellular annotations, and inferred copy number alterations (CNVs) for GSE178341 were obtained from the Curated Cancer Cell Atlas (https://www.weizmann.ac.il/sites/3CA/)[131,132]. To ensure high-quality scRNA-seq data, we applied

rigorous quality control (QC) criteria: first, cells with fewer than 500 or more than 8000 detected genes were removed to eliminate low-quality and potential multiplet cells. Second, cells with mitochondrial gene content exceeding 20% were excluded, as high mitochondrial RNA expression is often indicative of apoptotic or stressed cells. Third, malignant cells were subset for downstream analysis to focus on tumor-specific transcriptomic and genomic alterations.

Data preprocessing was conducted using Seurat v4 in R[133]. SCTransform v1 was applied to normalize raw UMI counts[134]. Harmony was used to correct batch effects across samples, ensuring effective dataset integration while maintaining cellular identity[135]. The average inferred CNV signal across chromosomes was computed to estimate chromosomal instability. Aneuploidy Score (AS) was calculated based on the defined formula for quantifying genomic instability[11]. To investigate the functional relevance of lysosomal activity in malignant cells: the KEGG lysosome gene set (MSigDB, M11266) was used to compute the Seurat module score.

Due to the zero-inflation characteristic of scRNA-seq data, additional filtering was applied before performing correlation analysis and UMAP Visualization: Cells with a combined expression of PARP1 and CEBPB below 4 were excluded from correlation and UMAP analyses to improve signal reliability. In the correlation analysis, log1p transformation is applied on SCTransform corrected UMI counts of CEBPB and PARP1, and Pearson correlation is applied to reveal the negative correlation. UMAP projections were aestheticized using Kernel Density Estimation (KDE), showing cells above the threshold on gene expression, lysosome module score (top 30% of all malignant cells) and aneuploidy score (>5), with density weights based on gene expression, aneuploidy score, and lysosome module score, improving interpretability in visualizations.

The CRISPRa Perturb-Seq data relevant to cells with CEBPB activation and non-targeting control was provided by Dr. Thomas Norman. The CEBPB and PARP1 read counts after total UMI count normalization were used in Fig. 6I (left panel). The PARP1 expression z-scores relative to expression levels in control cells were used in Fig. 6I (right panel).

Replicates and statistical analyses

For each experiment we reported the sample size, the number of replicates and the statistical methods in the figure legends. All statistical analyses are two-sided. The test statistics with confidence intervals, effect sizes, degrees of freedom and P value are detailed in Table 6.

Material Resource

The source and identifier for all materials used in this study are listed in Table 6.

Code availability

The code used to generate and/or analyze the data is available upon request.

Data availability

All datasets are available within the article and its supplementary information, or from the corresponding Author upon request.

1707 # References

1708 1. Weaver, B.A., and Cleveland, D.W. (2008). The aneuploidy paradox in cell growth and
1709 tumorigenesis. Cancer Cell 14, 431–433. https://doi.org/10.1016/j.ccr.2008.11.011.

1710 2. Ben-David, U., and Amon, A. (2020). Context is everything: aneuploidy in cancer. Nat. Rev.
1711 Genet. 21, 44–62. https://doi.org/10.1038/s41576-019-0171-x.

1712 3. Knouse, K.A., Davoli, T., Elledge, S.J., and Amon, A. (2017). Aneuploidy in Cancer: Seq-ing
1713 Answers to Old Questions. Annu. Rev. Cancer Biol. 1, 335–354.
1714 https://doi.org/10.1146/annurev-cancerbio-042616-072231.

1715 4. Lukow, D.A., and Sheltzer, J.M. (2021). Chromosomal instability and aneuploidy as causes of
1716 cancer drug resistance. Trends Cancer. https://doi.org/10.1016/j.trecan.2021.09.002.

1717 5. Davoli, T., Xu, A.W., Mengwasser, K.E., Sack, L.M., Yoon, J.C., Park, P.J., and Elledge, S.J.
1718 (2013). Cumulative haploinsufficiency and triplosensitivity drive aneuploidy patterns and
1719 shape the cancer genome. Cell 155, 948–962. https://doi.org/10.1016/j.cell.2013.10.011.

1720 6. William, W.N., Zhao, X., Bianchi, J.J., Lin, H.Y., Cheng, P., Lee, J.J., Carter, H., Alexandrov, L.B.,
1721 Abraham, J.P., Spetzler, D.B., et al. (2021). Immune evasion in HPV- head and neck
1722 precancer-cancer transition is driven by an aneuploid switch involving chromosome 9p loss.
1723 Proc. Natl. Acad. Sci. U. S. A. 118, e2022655118. https://doi.org/10.1073/pnas.2022655118.

1724 7. Santaguida, S., and Amon, A. (2015). Short- and long-term effects of chromosome mis-
1725 segregation and aneuploidy. Nat. Rev. Mol. Cell Biol. 16, 473–485.
1726 https://doi.org/10.1038/nrm4025.

1727 8. Zhu, J., Tsai, H.-J., Gordon, M.R., and Li, R. (2018). Cellular Stress Associated with
1728 Aneuploidy. Dev. Cell 44, 420–431. https://doi.org/10.1016/j.devcel.2018.02.002.

1729 9. Replogle, J.M., Zhou, W., Amaro, A.E., McFarland, J.M., Villalobos-Ortiz, M., Ryan, J., Letai, A.,
1730 Yilmaz, O., Sheltzer, J., Lippard, S.J., et al. (2020). Aneuploidy increases resistance to
1731 chemotherapeutics by antagonizing cell division. Proc. Natl. Acad. Sci. 117, 30566–30576.
1732 https://doi.org/10.1073/pnas.2009506117.

1733 10. Zerbib, J., Ippolito, M.R., Eliezer, Y., De Feudis, G., Reuveni, E., Savir Kadmon, A., Martin, S.,
1734 Viganò, S., Leor, G., Berstler, J., et al. (2024). Human aneuploid cells depend on the
1735 RAF/MEK/ERK pathway for overcoming increased DNA damage. Nat. Commun. 15, 7772.
1736 https://doi.org/10.1038/s41467-024-52176-x.

1737 11. Taylor, A.M., Shih, J., Ha, G., Gao, G.F., Zhang, X., Berger, A.C., Schumacher, S.E., Wang, C.,
1738 Hu, H., Liu, J., et al. (2018). Genomic and Functional Approaches to Understanding Cancer
1739 Aneuploidy. Cancer Cell 33, 676-689.e3. https://doi.org/10.1016/j.ccell.2018.03.007.

1740 12. Girish, V., Lakhani, A.A., Thompson, S.L., Scaduto, C.M., Brown, L.M., Hagenson, R.A.,
1741 Sausville, E.L., Mendelson, B.E., Kandikuppa, P.K., Lukow, D.A., et al. (2023). Oncogene-like
1742 addiction to aneuploidy in human cancers. Science 381, eadg4521.
1743 https://doi.org/10.1126/science.adg4521.

1744 13. Shih, J., Sarmashghi, S., Zhakula-Kostadinova, N., Zhang, S., Georgis, Y., Hoyt, S.H., Cuoco,
1745 M.S., Gao, G.F., Spurr, L.F., Berger, A.C., et al. (2023). Cancer aneuploidies are shaped
1746 primarily by effects on tumour fitness. Nature 619, 793–800.
1747 https://doi.org/10.1038/s41586-023-06266-3.

1748 14. Reczek, C.R., and Chandel, N.S. (2017). The Two Faces of Reactive Oxygen Species in
1749 Cancer. Annu. Rev. Cancer Biol. 1, 79–98. https://doi.org/10.1146/annurev-cancerbio-
1750 041916-065808.

1751 15. Gorrini, C., Harris, I.S., and Mak, T.W. (2013). Modulation of oxidative stress as an anticancer
1752 strategy. Nat. Rev. Drug Discov. 12, 931–947. https://doi.org/10.1038/nrd4002.

1753 16. Hayes, J.D., Dinkova-Kostova, A.T., and Tew, K.D. (2020). Oxidative Stress in Cancer. Cancer
1754 Cell 38, 167–197. https://doi.org/10.1016/j.ccell.2020.06.001.

1755 17. Piskounova, E., Agathocleous, M., Murphy, M.M., Hu, Z., Huddlestun, S.E., Zhao, Z., Leitch,
1756 A.M., Johnson, T.M., DeBerardinis, R.J., and Morrison, S.J. (2015). Oxidative stress inhibits
1757 distant metastasis by human melanoma cells. Nature 527, 186–191.
1758 https://doi.org/10.1038/nature15726.

1759 18. Crist, S.B., Nemkov, T., Dumpit, R.F., Dai, J., Tapscott, S.J., True, L.D., Swarbrick, A., Sullivan,
1760 L.B., Nelson, P.S., Hansen, K.C., et al. (2022). Unchecked oxidative stress in skeletal muscle
1761 prevents outgrowth of disseminated tumour cells. Nat. Cell Biol. 24, 538–553.
1762 https://doi.org/10.1038/s41556-022-00881-4.

1763 19. Nguyen, B., Fong, C., Luthra, A., Smith, S.A., DiNatale, R.G., Nandakumar, S., Walch, H.,
1764 Chatila, W.K., Madupuri, R., Kundra, R., et al. (2022). Genomic characterization of metastatic
1765 patterns from prospective clinical sequencing of 25,000 patients. Cell 185, 563-575.e11.
1766 https://doi.org/10.1016/j.cell.2022.01.003.

1767 20. Caldecott, K.W. (2008). Single-strand break repair and genetic disease. Nat. Rev. Genet. 9,
1768 619–631. https://doi.org/10.1038/nrg2380.

1769 21. Ray Chaudhuri, A., and Nussenzweig, A. (2017). The multifaceted roles of PARP1 in DNA
1770 repair and chromatin remodelling. Nat. Rev. Mol. Cell Biol. 18, 610–621.
1771 https://doi.org/10.1038/nrm.2017.53.

1772 22. David, K.K., Andrabi, S.A., Dawson, T.M., and Dawson, V.L. (2009). Parthanatos, a messenger
1773 of death. Front. Biosci. Landmark Ed. 14, 1116–1128.

1774 23. Ha, H.C., and Snyder, S.H. (1999). Poly(ADP-ribose) polymerase is a mediator of necrotic cell

1775 death by ATP depletion. Proc. Natl. Acad. Sci. 96, 13978–13982.
1776 https://doi.org/10.1073/pnas.96.24.13978.

1777 24. Andrabi, S.A., Dawson, T.M., and Dawson, V.L. (2008). Mitochondrial and Nuclear Cross Talk
1778 in Cell Death. Ann. N. Y. Acad. Sci. 1147, 233–241. https://doi.org/10.1196/annals.1427.014.

1779 25. Roos, W.P., Thomas, A.D., and Kaina, B. (2016). DNA damage and the balance between
1780 survival and death in cancer biology. Nat. Rev. Cancer 16, 20–33.
1781 https://doi.org/10.1038/nrc.2015.2.

1782 26. Eliasson, M.J., Sampei, K., Mandir, A.S., Hurn, P.D., Traystman, R.J., Bao, J., Pieper, A., Wang,
1783 Z.Q., Dawson, T.M., Snyder, S.H., et al. (1997). Poly(ADP-ribose) polymerase gene disruption
1784 renders mice resistant to cerebral ischemia. Nat. Med. 3, 1089–1095.
1785 https://doi.org/10.1038/nm1097-1089.

1786 27. Maru, B., Messikommer, A., Huang, L., Seipel, K., Kovecses, O., Valk, P.J.M., Theocharides,
1787 A.P.A., Mercier, F.E., Pabst, T., McKeague, M., et al. (2023). PARP-1 improves leukemia
1788 outcomes by inducing parthanatos during chemotherapy. Cell Rep. Med. 4, 101191.
1789 https://doi.org/10.1016/j.xcrm.2023.101191.

1790 28. Santaguida, S., Vasile, E., White, E., and Amon, A. (2015). Aneuploidy-induced cellular
1791 stresses limit autophagic degradation. Genes Dev. 29, 2010–2021.
1792 https://doi.org/10.1101/gad.269118.115.

1793 29. Dürrbaum, M., Kuznetsova, A.Y., Passerini, V., Stingele, S., Stoehr, G., and Storchová, Z.
1794 (2014). Unique features of the transcriptional response to model aneuploidy in human cells.
1795 BMC Genomics 15, 139. https://doi.org/10.1186/1471-2164-15-139.

1796 30. Cheng, P., Zhao, X., Katsnelson, L., Camacho-Hernandez, E.M., Mermerian, A., Mays, J.C.,
1797 Lippman, S.M., Rosales-Alvarez, R.E., Moya, R., Shwetar, J., et al. (2022). Proteogenomic
1798 analysis of cancer aneuploidy and normal tissues reveals divergent modes of gene
1799 regulation across cellular pathways. eLife 11, e75227. https://doi.org/10.7554/eLife.75227.

1800 31. Stingele, S., Stoehr, G., Peplowska, K., Cox, J., Mann, M., and Storchova, Z. (2012). Global
1801 analysis of genome, transcriptome and proteome reveals the response to aneuploidy in
1802 human cells. Mol. Syst. Biol. 8, 608. https://doi.org/10.1038/msb.2012.40.

1803 32. Liu, Y., Marks, K., Cowley, G.S., Carretero, J., Liu, Q., Nieland, T.J.F., Xu, C., Cohoon, T.J., Gao,
1804 P., Zhang, Y., et al. (2013). Metabolic and functional genomic studies identify
1805 deoxythymidylate kinase as a target in LKB1-mutant lung cancer. Cancer Discov. 3, 870–
1806 879. https://doi.org/10.1158/2159-8290.CD-13-0015.

1807 33. Chen, Z., Cheng, K., Walton, Z., Wang, Y., Ebi, H., Shimamura, T., Liu, Y., Tupper, T., Ouyang, J.,
1808 Li, J., et al. (2012). A murine lung cancer co-clinical trial identifies genetic modifiers of
1809 therapeutic response. Nature 483, 613–617. https://doi.org/10.1038/nature10937.

34. Bosco, N., Goldberg, A., Zhao, X., Mays, J.C., Cheng, P., Johnson, A.F., Bianchi, J.J., Toscani, C., Di Tommaso, E., Katsnelson, L., et al. (2023). KaryoCreate: A CRISPR-based technology to study chromosome-specific aneuploidy by targeting human centromeres. Cell 186, 1985-2001.e19. https://doi.org/10.1016/j.cell.2023.03.029.

35. Jacobi, J., Kristal, B., Chezar, J., Shaul, S.M., and Sela, S. (2005). Exogenous superoxide mediates pro-oxidative, proinflammatory, and procoagulatory changes in primary endothelial cell cultures. Free Radic. Biol. Med. 39, 1238–1248. https://doi.org/10.1016/j.freeradbiomed.2005.06.010.

36. Ma, Q. (2013). Role of Nrf2 in Oxidative Stress and Toxicity. Annu. Rev. Pharmacol. Toxicol. 53, 401–426. https://doi.org/10.1146/annurev-pharmtox-011112-140320.

37. Hirakata, C., Lima, K., De Almeida, B.O., De Miranda, L.B.L., Florêncio, K.G.D., Furtado, L.C., Costa-Lotufo, L.V., and Machado-Neto, J.A. (2021). Targeting glioma cells by antineoplastic activity of reversine. Oncol. Lett. 22, 610. https://doi.org/10.3892/ol.2021.12871.

38. Sanchez-Vasquez, E., Bronner, M.E., and Zernicka-Goetz, M. (2023). HIF1A contributes to the survival of aneuploid and mosaic pre-implantation embryos. Preprint at bioRxiv, https://doi.org/10.1101/2023.09.04.556218 https://doi.org/10.1101/2023.09.04.556218.

39. Kaufmann, S.H., Desnoyers, S., Ottaviano, Y., Davidson, N.E., and Poirier, G.G. (1993). Specific Proteolytic Cleavage of Poly(ADP-ribose) Polymerase: An Early Marker of Chemotherapy-induced Apoptosis1. Cancer Res. 53, 3976–3985.

40. Wang, X., Liu, L., Montagna, C., Ried, T., and Deng, C.-X. (2007). Haploinsufficiency of Parp1 accelerates Brca1-associated centrosome amplification, telomere shortening, genetic instability, apoptosis, and embryonic lethality. Cell Death Differ. 14, 924–931. https://doi.org/10.1038/sj.cdd.4402105.

41. Fatokun, A.A., Dawson, V.L., and Dawson, T.M. (2014). Parthanatos: mitochondrial-linked mechanisms and therapeutic opportunities. Br. J. Pharmacol. 171, 2000–2016. https://doi.org/10.1111/bph.12416.

42. Liu, S., Luo, W., and Wang, Y. (2022). Emerging role of PARP-1 and PARthanatos in ischemic stroke. J. Neurochem. 160, 74–87. https://doi.org/10.1111/jnc.15464.

43. Young, L.M., Marzio, A., Perez-Duran, P., Reid, D.A., Meredith, D.N., Roberti, D., Star, A., Rothenberg, E., Ueberheide, B., and Pagano, M. (2015). TIMELESS Forms a Complex with PARP1 Distinct from Its Complex with TIPIN and Plays a Role in the DNA Damage Response. Cell Rep. 13, 451–459. https://doi.org/10.1016/j.celrep.2015.09.017.

44. Amé, J.C., Rolli, V., Schreiber, V., Niedergang, C., Apiou, F., Decker, P., Muller, S., Höger, T., Ménissier-de Murcia, J., and de Murcia, G. (1999). PARP-2, A novel mammalian DNA damage-dependent poly(ADP-ribose) polymerase. J. Biol. Chem. 274, 17860–17868. https://doi.org/10.1074/jbc.274.25.17860.

1846 45. Wang, Y., An, R., Umanah, G.K., Park, H., Nambiar, K., Eacker, S.M., Kim, B., Bao, L., Harraz,
1847 M.M., Chang, C., et al. (2016). A nuclease that mediates cell death induced by DNA damage
1848 and poly(ADP-ribose) polymerase-1. Science 354, aad6872.
1849 https://doi.org/10.1126/science.aad6872.

1850 46. Hurtado-Bagès, S., Knobloch, G., Ladurner, A.G., and Buschbeck, M. (2020). The taming of
1851 PARP1 and its impact on NAD+ metabolism. Mol. Metab. 38, 100950.
1852 https://doi.org/10.1016/j.molmet.2020.01.014.

1853 47. Ciccia, A., and Elledge, S.J. (2010). The DNA Damage Response: Making It Safe to Play with
1854 Knives. Mol. Cell 40, 179–204. https://doi.org/10.1016/j.molcel.2010.09.019.

1855 48. Artus, C., Boujrad, H., Bouharrour, A., Brunelle, M.-N., Hoos, S., Yuste, V.J., Lenormand, P.,
1856 Rousselle, J.-C., Namane, A., England, P., et al. (2010). AIF promotes chromatinolysis and
1857 caspase-independent programmed necrosis by interacting with histone H2AX. EMBO J. 29,
1858 1585–1599. https://doi.org/10.1038/emboj.2010.43.

1859 49. Sayin, V.I., Ibrahim, M.X., Larsson, E., Nilsson, J.A., Lindahl, P., and Bergo, M.O. (2014).
1860 Antioxidants accelerate lung cancer progression in mice. Sci. Transl. Med. 6, 221ra15.
1861 https://doi.org/10.1126/scitranslmed.3007653.

1862 50. Laubert, T., Freitag-Wolf, S., Linnebacher, M., König, A., Vollmar, B., Habermann, J.K., and on
1863 behalf of the North German Tumorbank of Colorectal Cancer (ColoNet) consortium (2015).
1864 Stage-specific frequency and prognostic significance of aneuploidy in patients with sporadic
1865 colorectal cancer—a meta-analysis and current overview. Int. J. Colorectal Dis. 30, 1015–
1866 1028. https://doi.org/10.1007/s00384-015-2259-x.

1867 51. Dörsam, B., Seiwert, N., Foersch, S., Stroh, S., Nagel, G., Begaliew, D., Diehl, E., Kraus, A.,
1868 McKeague, M., Minneker, V., et al. (2018). PARP-1 protects against colorectal tumor
1869 induction, but promotes inflammation-driven colorectal tumor progression. Proc. Natl. Acad.
1870 Sci. 115, E4061–E4070. https://doi.org/10.1073/pnas.1712345115.

1871 52. Kamal, Y., Schmit, S.L., Hoehn, H.J., Amos, C.I., and Frost, H.R. (2019). Transcriptomic
1872 Differences between Primary Colorectal Adenocarcinomas and Distant Metastases Reveal
1873 Metastatic Colorectal Cancer Subtypes. Cancer Res. 79, 4227–4241.
1874 https://doi.org/10.1158/0008-5472.CAN-18-3945.

1875 53. Zhu, X., Zhang, H., and Mendell, J.T. (2020). Ribosome Recycling by ABCE1 Links Lysosomal
1876 Function and Iron Homeostasis to 3' UTR-Directed Regulation and Nonsense-Mediated
1877 Decay. Cell Rep. 32, 107895. https://doi.org/10.1016/j.celrep.2020.107895.

1878 54. Weber, R.A., Yen, F.S., Nicholson, S.P.V., Alwaseem, H., Bayraktar, E.C., Alam, M., Timson,
1879 R.C., La, K., Abu-Remaileh, M., Molina, H., et al. (2020). Maintaining Iron Homeostasis Is the
1880 Key Role of Lysosomal Acidity for Cell Proliferation. Mol. Cell 77, 645-655.e7.
1881 https://doi.org/10.1016/j.molcel.2020.01.003.

1882 55. S, S., I, Z., Jk, D.B., and Mg, R. (2010). Inhibition of iron uptake is responsible for differential
1883 sensitivity to V-ATPase inhibitors in several cancer cell lines. PloS One 5.
1884 https://doi.org/10.1371/journal.pone.0011629.

1885 56. Wu, T., Wang, G., Chen, W., Zhu, Z., Liu, Y., Huang, Z., Huang, Y., Du, P., Yang, Y., Liu, C.-Y., et
1886 al. (2018). Co-inhibition of BET proteins and NF-κB as a potential therapy for colorectal
1887 cancer through synergistic inhibiting MYC and FOXM1 expressions. Cell Death Dis. 9, 315.
1888 https://doi.org/10.1038/s41419-018-0354-y.

1889 57. Tu, C., Liu, Y., Williams, D.R., and Wu, J.C. (2022). A transcriptomic atlas of drug-induced
1890 endothelial dysfunction in human endothelial cells. J. Mol. Cell. Cardiol. 173, 115–117.
1891 https://doi.org/10.1016/j.yjmcc.2022.10.002.

1892 58. Cáceres-Gutiérrez, R.E., Andonegui, M.A., Oliva-Rico, D.A., González-Barrios, R., Luna, F.,
1893 Arriaga-Canon, C., López-Saavedra, A., Prada, D., Castro, C., Parmentier, L., et al. (2022).
1894 Proteasome inhibition alters mitotic progression through the upregulation of centromeric α-
1895 Satellite RNAs. FEBS J. 289, 1858–1875. https://doi.org/10.1111/febs.16261.

1896 59. Shen, W.-K., Chen, S.-Y., Gan, Z.-Q., Zhang, Y.-Z., Yue, T., Chen, M.-M., Xue, Y., Hu, H., and Guo,
1897 A.-Y. (2023). AnimalTFDB 4.0: a comprehensive animal transcription factor database
1898 updated with variation and expression annotations. Nucleic Acids Res. 51, D39–D45.
1899 https://doi.org/10.1093/nar/gkac907.

1900 60. Liska, O., Bohár, B., Hidas, A., Korcsmáros, T., Papp, B., Fazekas, D., and Ari, E. (2022). TFLink:
1901 an integrated gateway to access transcription factor-target gene interactions for multiple
1902 species. Database J. Biol. Databases Curation 2022, baac083.
1903 https://doi.org/10.1093/database/baac083.

1904 61. Fishilevich, S., Nudel, R., Rappaport, N., Hadar, R., Plaschkes, I., Iny Stein, T., Rosen, N., Kohn,
1905 A., Twik, M., Safran, M., et al. (2017). GeneHancer: genome-wide integration of enhancers
1906 and target genes in GeneCards. Database J. Biol. Databases Curation 2017, bax028.
1907 https://doi.org/10.1093/database/bax028.

1908 62. Hitz, B.C., Jin-Wook, L., Jolanki, O., Kagda, M.S., Graham, K., Sud, P., Gabdank, I., Strattan,
1909 J.S., Sloan, C.A., Dreszer, T., et al. (2023). The ENCODE Uniform Analysis Pipelines. BioRxiv
1910 Prepr. Serv. Biol., 2023.04.04.535623. https://doi.org/10.1101/2023.04.04.535623.

1911 63. Keenan, A.B., Torre, D., Lachmann, A., Leong, A.K., Wojciechowicz, M.L., Utti, V., Jagodnik,
1912 K.M., Kropiwnicki, E., Wang, Z., and Ma'ayan, A. (2019). ChEA3: transcription factor
1913 enrichment analysis by orthogonal omics integration. Nucleic Acids Res. 47, W212–W224.
1914 https://doi.org/10.1093/nar/gkz446.

1915 64. Southard, K.M., Ardy, R.C., Tang, A., O'Sullivan, D.D., Metzner, E., Guruvayurappan, K., and
1916 Norman, T.M. (2024). Comprehensive transcription factor perturbations recapitulate
1917 fibroblast transcriptional states. Preprint at bioRxiv,
1918 https://doi.org/10.1101/2024.07.31.606073 https://doi.org/10.1101/2024.07.31.606073.

1919 65. Dephoure, N., Hwang, S., O'Sullivan, C., Dodgson, S.E., Gygi, S.P., Amon, A., and Torres, E.M.
1920 (2014). Quantitative proteomic analysis reveals posttranslational responses to aneuploidy in
1921 yeast. eLife 3, e03023. https://doi.org/10.7554/eLife.03023.

1922 66. Citarelli, M., Teotia, S., and Lamb, R.S. (2010). Evolutionary history of the poly(ADP-ribose)
1923 polymerase gene family in eukaryotes. BMC Evol. Biol. 10, 308.
1924 https://doi.org/10.1186/1471-2148-10-308.

1925 67. Clemente-Ruiz, M., Murillo-Maldonado, J.M., Benhra, N., Barrio, L., Pérez, L., Quiroga, G.,
1926 Nebreda, A.R., and Milán, M. (2016). Gene Dosage Imbalance Contributes to Chromosomal
1927 Instability-Induced Tumorigenesis. Dev. Cell 36, 290–302.
1928 https://doi.org/10.1016/j.devcel.2016.01.008.

1929 68. Li, M., Fang, X., Baker, D.J., Guo, L., Gao, X., Wei, Z., Han, S., van Deursen, J.M., and Zhang, P.
1930 (2010). The ATM-p53 pathway suppresses aneuploidy-induced tumorigenesis. Proc. Natl.
1931 Acad. Sci. U. S. A. 107, 14188–14193. https://doi.org/10.1073/pnas.1005960107.

1932 69. Marderstein, A.R., De Zuani, M., Moeller, R., Bezney, J., Padhi, E.M., Wong, S., Coorens, T.H.H.,
1933 Xie, Y., Xue, H., Montgomery, S.B., et al. (2024). Single-cell multi-omics map of human fetal
1934 blood in Down syndrome. Nature 634, 104–112. https://doi.org/10.1038/s41586-024-
1935 07946-4.

1936 70. Weick, J.P., Held, D.L., Bonadurer, G.F., Doers, M.E., Liu, Y., Maguire, C., Clark, A., Knackert,
1937 J.A., Molinarolo, K., Musser, M., et al. (2013). Deficits in human trisomy 21 iPSCs and
1938 neurons. Proc. Natl. Acad. Sci. 110, 9962–9967. https://doi.org/10.1073/pnas.1216575110.

1939 71. Tentori, L., Leonetti, C., Scarsella, M., Muzi, A., Mazzon, E., Vergati, M., Forini, O., Lapidus, R.,
1940 Xu, W., Dorio, A.S., et al. (2006). Inhibition of poly(ADP-ribose) polymerase prevents
1941 irinotecan-induced intestinal damage and enhances irinotecan/temozolomide efficacy
1942 against colon carcinoma. FASEB J. Off. Publ. Fed. Am. Soc. Exp. Biol. 20, 1709–1711.
1943 https://doi.org/10.1096/fj.06-5916fje.

1944 72. Yamanaka, H., Penning, C.A., Willis, E.H., Wasson, D.B., and Carson, D.A. (1988).
1945 Characterization of human poly(ADP-ribose) polymerase with autoantibodies. J. Biol. Chem.
1946 263, 3879–3883.

1947 73. Santos, A., Wernersson, R., and Jensen, L.J. (2015). Cyclebase 3.0: a multi-organism
1948 database on cell-cycle regulation and phenotypes. Nucleic Acids Res. 43, D1140–D1144.
1949 https://doi.org/10.1093/nar/gku1092.

1950 74. Wiśnik, E., Płoszaj, T., and Robaszkiewicz, A. (2017). Downregulation of PARP1 transcription
1951 by promoter-associated E2F4-RBL2-HDAC1-BRM complex contributes to repression of
1952 pluripotency stem cell factors in human monocytes. Sci. Rep. 7, 9483.
1953 https://doi.org/10.1038/s41598-017-10307-z.

1954 75. Nassour, J., Martien, S., Martin, N., Deruy, E., Tomellini, E., Malaquin, N., Bouali, F., Sabatier, L.,

Wernert, N., Pinte, S., et al. (2016). Defective DNA single-strand break repair is responsible for senescence and neoplastic escape of epithelial cells. Nat. Commun. 7, 10399. https://doi.org/10.1038/ncomms10399.

76. Thompson, S.L., and Compton, D.A. (2010). Proliferation of aneuploid human cells is limited by a p53-dependent mechanism. J. Cell Biol. 188, 369–381. https://doi.org/10.1083/jcb.200905057.

77. Santaguida, S., Richardson, A., Iyer, D.R., M'Saad, O., Zasadil, L., Knouse, K.A., Wong, Y.L., Rhind, N., Desai, A., and Amon, A. (2017). Chromosome Mis-segregation Generates Cell-Cycle-Arrested Cells with Complex Karyotypes that Are Eliminated by the Immune System. Dev. Cell 41, 638-651.e5. https://doi.org/10.1016/j.devcel.2017.05.022.

78. Passerini, V., Ozeri-Galai, E., de Pagter, M.S., Donnelly, N., Schmalbrock, S., Kloosterman, W.P., Kerem, B., and Storchová, Z. (2016). The presence of extra chromosomes leads to genomic instability. Nat. Commun. 7, 10754. https://doi.org/10.1038/ncomms10754.

79. Jacob, S., Aguado, M., Fallik, D., and Praz, F. (2001). The Role of the DNA Mismatch Repair System in the Cytotoxicity of the Topoisomerase Inhibitors Camptothecin and Etoposide to Human Colorectal Cancer Cells1. Cancer Res. 61, 6555–6562.

80. Bazzocco, S., Dopeso, H., Carton-Garcia, F., Macaya, I., Andretta, E., Chionh, F., Rodrigues, P., Garrido, M., Alazzouzi, H., Nieto, R., et al. (2015). Highly Expressed Genes in Rapidly Proliferating Tumor Cells as New Targets for Colorectal Cancer Treatment. Clin. Cancer Res. 21, 3695–3704. https://doi.org/10.1158/1078-0432.CCR-14-2457.

81. Soldatenkov, V.A., Albor, A., Patel, B.K., Dreszer, R., Dritschilo, A., and Notario, V. (1999). Regulation of the human poly(ADP-ribose) polymerase promoter by the ETS transcription factor. Oncogene 18, 3954–3962. https://doi.org/10.1038/sj.onc.1202778.

82. Zhu, Y., Liu, Y., Ma, Y., Chen, L., Huang, H., Huang, S., Zhang, H., He, Y., Tan, C., He, Y., et al. (2023). Macrophage autophagy deficiency-induced CEBPB accumulation alleviates atopic dermatitis via impairing M2 polarization. Cell Rep. 42, 113430. https://doi.org/10.1016/j.celrep.2023.113430.

83. Kim, D., Kim, J., Yu, Y.S., Kim, Y.R., Baek, S.H., and Won, K.-J. (2022). Systemic approaches using single cell transcriptome reveal that C/EBPγ regulates autophagy under amino acid starved condition. Nucleic Acids Res. 50, 7298–7309. https://doi.org/10.1093/nar/gkac593.

84. Podust, L.M., Krezel, A.M., and Kim, Y. (2001). Crystal Structure of the CCAAT Box/Enhancer-binding Protein β Activating Transcription Factor-4 Basic Leucine Zipper Heterodimer in the Absence of DNA*. J. Biol. Chem. 276, 505–513. https://doi.org/10.1074/jbc.M005594200.

85. Wadgaonkar, P., Bi, Z., Wan, J., Fu, Y., Zhang, Q., Almutairy, B., Zhang, W., Qiu, Y., Thakur, C., Hüttemann, M., et al. (2022). Arsenic Activates the ER Stress-Associated Unfolded Protein Response via the Activating Transcription Factor 6 in Human Bronchial Epithelial Cells.

1991 Biomedicines 10, 967. https://doi.org/10.3390/biomedicines10050967.

1992 86. Pacher, P., and Szabo, C. (2008). Role of the peroxynitrite-poly(ADP-ribose) polymerase
1993 pathway in human disease. Am. J. Pathol. 173, 2–13.
1994 https://doi.org/10.2353/ajpath.2008.080019.

1995 87. Oláh, G., Szczesny, B., Brunyánszki, A., López-García, I.A., Gerö, D., Radák, Z., and Szabo, C.
1996 (2015). Differentiation-Associated Downregulation of Poly(ADP-Ribose) Polymerase-1
1997 Expression in Myoblasts Serves to Increase Their Resistance to Oxidative Stress. PLOS ONE
1998 10, e0134227. https://doi.org/10.1371/journal.pone.0134227.

1999 88. Yu, S.-W., Wang, H., Poitras, M.F., Coombs, C., Bowers, W.J., Federoff, H.J., Poirier, G.G.,
2000 Dawson, T.M., and Dawson, V.L. (2002). Mediation of Poly(ADP-Ribose) Polymerase-1-
2001 Dependent Cell Death by Apoptosis-Inducing Factor. Science 297, 259–263.
2002 https://doi.org/10.1126/science.1072221.

2003 89. Dawson, T.M., and Dawson, V.L. (2017). Mitochondrial Mechanisms of Neuronal Cell Death:
2004 Potential Therapeutics. Annu. Rev. Pharmacol. Toxicol. 57, 437–454.
2005 https://doi.org/10.1146/annurev-pharmtox-010716-105001.

2006 90. Zheng, J., Devalaraja-Narashimha, K., Singaravelu, K., and Padanilam, B.J. (2005). Poly(ADP-
2007 ribose) polymerase-1 gene ablation protects mice from ischemic renal injury. Am. J.
2008 Physiol.-Ren. Physiol. 288, F387–F398. https://doi.org/10.1152/ajprenal.00436.2003.

2009 91. Lukow, D.A., Sausville, E.L., Suri, P., Chunduri, N.K., Wieland, A., Leu, J., Smith, J.C., Girish, V.,
2010 Kumar, A.A., Kendall, J., et al. (2021). Chromosomal instability accelerates the evolution of
2011 resistance to anti-cancer therapies. Dev. Cell 56, 2427-2439.e4.
2012 https://doi.org/10.1016/j.devcel.2021.07.009.

2013 92. Ippolito, M.R., Martis, V., Martin, S., Tijhuis, A.E., Hong, C., Wardenaar, R., Dumont, M., Zerbib,
2014 J., Spierings, D.C.J., Fachinetti, D., et al. (2021). Gene copy-number changes and
2015 chromosomal instability induced by aneuploidy confer resistance to chemotherapy. Dev. Cell
2016 56, 2440-2454.e6. https://doi.org/10.1016/j.devcel.2021.07.006.

2017 93. Lee, A.J.X., Endesfelder, D., Rowan, A.J., Walther, A., Birkbak, N.J., Futreal, P.A., Downward, J.,
2018 Szallasi, Z., Tomlinson, I.P.M., Howell, M., et al. (2011). Chromosomal instability confers
2019 intrinsic multidrug resistance. Cancer Res. 71, 1858–1870. https://doi.org/10.1158/0008-
2020 5472.CAN-10-3604.

2021 94. Fisher, A.E.O., Hochegger, H., Takeda, S., and Caldecott, K.W. (2007). Poly(ADP-Ribose)
2022 Polymerase 1 Accelerates Single-Strand Break Repair in Concert with Poly(ADP-Ribose)
2023 Glycohydrolase. Mol. Cell. Biol. 27, 5597–5605. https://doi.org/10.1128/MCB.02248-06.

2024 95. Patel, A.G., Sarkaria, J.N., and Kaufmann, S.H. (2011). Nonhomologous end joining drives
2025 poly(ADP-ribose) polymerase (PARP) inhibitor lethality in homologous recombination-
2026 deficient cells. Proc. Natl. Acad. Sci. 108, 3406–3411.

https://doi.org/10.1073/pnas.1013715108.

96. Huang, D., and Kraus, W.L. (2022). The expanding universe of PARP1-mediated molecular and therapeutic mechanisms. Mol. Cell 82, 2315–2334. https://doi.org/10.1016/j.molcel.2022.02.021.

97. Li, F., Wu, X., Fu, X., Liu, J., Song, W., Xiao, G.G., Lu, A., and Zhang, G. (2022). Poly (ADP-ribose) polymerase 1 (PARP1) inhibition promotes pulmonary metastasis of osteosarcoma by boosting ezrin phosphorylation. Int. J. Biol. Sci. 18, 1238–1253. https://doi.org/10.7150/ijbs.58784.

98. Choi, E.-B., Yang, A.-Y., Kim, S.C., Lee, J., Choi, J.K., Choi, C., and Kim, M.-Y. (2016). PARP1 enhances lung adenocarcinoma metastasis by novel mechanisms independent of DNA repair. Oncogene 35, 4569–4579. https://doi.org/10.1038/onc.2016.3.

99. Zuo, H., Yang, D., Yang, Q., Tang, H., Fu, Y.-X., and Wan, Y. (2020). Differential regulation of breast cancer bone metastasis by PARP1 and PARP2. Nat. Commun. 11, 1578. https://doi.org/10.1038/s41467-020-15429-z.

100. Lord, C.J., and Ashworth, A. (2017). PARP Inhibitors: The First Synthetic Lethal Targeted Therapy. Science 355, 1152–1158. https://doi.org/10.1126/science.aam7344.

101. Murai, J., Huang, S.N., Das, B.B., Renaud, A., Zhang, Y., Doroshow, J.H., Ji, J., Takeda, S., and Pommier, Y. (2012). Trapping of PARP1 and PARP2 by Clinical PARP Inhibitors. Cancer Res. 72, 5588–5599. https://doi.org/10.1158/0008-5472.CAN-12-2753.

102. Byers, L.A., Wang, J., Nilsson, M.B., Fujimoto, J., Saintigny, P., Yordy, J., Giri, U., Peyton, M., Fan, Y.H., Diao, L., et al. (2012). Proteomic Profiling Identifies Dysregulated Pathways in Small Cell Lung Cancer and Novel Therapeutic Targets Including PARP1. Cancer Discov. 2, 798–811. https://doi.org/10.1158/2159-8290.CD-12-0112.

103. França, G.S., Baron, M., King, B.R., Bossowski, J.P., Bjornberg, A., Pour, M., Rao, A., Patel, A.S., Misirlioglu, S., Barkley, D., et al. (2024). Cellular adaptation to cancer therapy along a resistance continuum. Nature 631, 876–883. https://doi.org/10.1038/s41586-024-07690-9.

104. Rouleau, M., Patel, A., Hendzel, M.J., Kaufmann, S.H., and Poirier, G.G. (2010). PARP inhibition: PARP1 and beyond. Nat. Rev. Cancer 10, 293–301. https://doi.org/10.1038/nrc2812.

105. Roig, A.I., Eskiocak, U., Hight, S.K., Kim, S.B., Delgado, O., Souza, R.F., Spechler, S.J., Wright, W.E., and Shay, J.W. (2010). Immortalized Epithelial Cells Derived From Human Colon Biopsies Express Stem Cell Markers and Differentiate In Vitro. Gastroenterology 138, 1012-1021.e5. https://doi.org/10.1053/j.gastro.2009.11.052.

106. Sack, L.M., Davoli, T., Li, M.Z., Li, Y., Xu, Q., Naxerova, K., Wooten, E.C., Bernardi, R.J., Martin, T.D., Chen, T., et al. (2018). Profound Tissue Specificity in Proliferation Control Underlies

2062 Cancer Drivers and Aneuploidy Patterns. Cell 173, 499-514.e23.
2063 https://doi.org/10.1016/j.cell.2018.02.037.

2064 107. Meerbrey, K.L., Hu, G., Kessler, J.D., Roarty, K., Li, M.Z., Fang, J.E., Herschkowitz, J.I.,
2065 Burrows, A.E., Ciccia, A., Sun, T., et al. (2011). The pINDUCER lentiviral toolkit for inducible
2066 RNA interference in vitro and in vivo. Proc. Natl. Acad. Sci. U. S. A. 108, 3665–3670.
2067 https://doi.org/10.1073/pnas.1019736108.

2068 108. Young, L.M., Marzio, A., Perez-Duran, P., Reid, D.A., Meredith, D.N., Roberti, D., Star, A.,
2069 Rothenberg, E., Ueberheide, B., and Pagano, M. (2015). TIMELESS Forms a Complex with
2070 PARP1 Distinct from Its Complex with TIPIN and Plays a Role in the DNA Damage
2071 Response. Cell Rep. 13, 451–459. https://doi.org/10.1016/j.celrep.2015.09.017.

2072 109. Chunduri, N.K., and Storchová, Z. (2019). The diverse consequences of aneuploidy. Nat. Cell
2073 Biol. 21, 54–62. https://doi.org/10.1038/s41556-018-0243-8.

2074 110. Nilsen, G., Liestøl, K., Van Loo, P., Moen Vollan, H.K., Eide, M.B., Rueda, O.M., Chin, S.-F.,
2075 Russell, R., Baumbusch, L.O., Caldas, C., et al. (2012). Copynumber: Efficient algorithms for
2076 single- and multi-track copy number segmentation. BMC Genomics 13, 591.
2077 https://doi.org/10.1186/1471-2164-13-591.

2078 111. Cohen-Sharir, Y., McFarland, J.M., Abdusamad, M., Marquis, C., Bernhard, S.V., Kazachkova,
2079 M., Tang, H., Ippolito, M.R., Laue, K., Zerbib, J., et al. (2021). Aneuploidy renders cancer cells
2080 vulnerable to mitotic checkpoint inhibition. Nature 590, 486–491.
2081 https://doi.org/10.1038/s41586-020-03114-6.

2082 112. Carter, S.L., Cibulskis, K., Helman, E., McKenna, A., Shen, H., Zack, T., Laird, P.W., Onofrio,
2083 R.C., Winckler, W., Weir, B.A., et al. (2012). Absolute quantification of somatic DNA
2084 alterations in human cancer. Nat. Biotechnol. 30, 413–421.
2085 https://doi.org/10.1038/nbt.2203.

2086 113. Zhao, X., Cohen, E.E.W., William, W.N., Bianchi, J.J., Abraham, J.P., Magee, D., Spetzler, D.B.,
2087 Gutkind, J.S., Alexandrov, L.B., Cavenee, W.K., et al. (2022). Somatic 9p24.1 alterations in
2088 HPV- head and neck squamous cancer dictate immune microenvironment and anti-PD-1
2089 checkpoint inhibitor activity. Proc. Natl. Acad. Sci. U. S. A. 119, e2213835119.
2090 https://doi.org/10.1073/pnas.2213835119.

2091 114. Fontana, P., Bonfiglio, J.J., Palazzo, L., Bartlett, E., Matic, I., and Ahel, I. (2017). Serine ADP-
2092 ribosylation reversal by the hydrolase ARH3. eLife 6, e28533.
2093 https://doi.org/10.7554/eLife.28533.

2094 115. Dobin, A., Davis, C.A., Schlesinger, F., Drenkow, J., Zaleski, C., Jha, S., Batut, P., Chaisson, M.,
2095 and Gingeras, T.R. (2013). STAR: ultrafast universal RNA-seq aligner. Bioinforma. Oxf. Engl.
2096 29, 15–21. https://doi.org/10.1093/bioinformatics/bts635.

2097 116. Li, B., and Dewey, C.N. (2011). RSEM: accurate transcript quantification from RNA-Seq data

with or without a reference genome. BMC Bioinformatics 12, 323. https://doi.org/10.1186/1471-2105-12-323.

117. Love, M.I., Huber, W., and Anders, S. (2014). Moderated estimation of fold change and dispersion for RNA-seq data with DESeq2. Genome Biol. 15, 550. https://doi.org/10.1186/s13059-014-0550-8.

118. Ghandi, M., Huang, F.W., Jané-Valbuena, J., Kryukov, G.V., Lo, C.C., McDonald, E.R., Barretina, J., Gelfand, E.T., Bielski, C.M., Li, H., et al. (2019). Next-generation characterization of the Cancer Cell Line Encyclopedia. Nature 569, 503–508. https://doi.org/10.1038/s41586-019-1186-3.

119. Barretina, J., Caponigro, G., Stransky, N., Venkatesan, K., Margolin, A.A., Kim, S., Wilson, C.J., Lehár, J., Kryukov, G.V., Sonkin, D., et al. (2012). The Cancer Cell Line Encyclopedia enables predictive modelling of anticancer drug sensitivity. Nature 483, 603–607. https://doi.org/10.1038/nature11003.

120. Gautier, L., Cope, L., Bolstad, B.M., and Irizarry, R.A. (2004). affy—analysis of Affymetrix GeneChip data at the probe level. Bioinformatics 20, 307–315. https://doi.org/10.1093/bioinformatics/btg405.

121. Zhang, Y., Chen, F., and Creighton, C.J. (2023). Pan-cancer molecular subtypes of metastasis reveal distinct and evolving transcriptional programs. Cell Rep. Med. 4, 100932. https://doi.org/10.1016/j.xcrm.2023.100932.

122. Cox, J., and Mann, M. (2008). MaxQuant enables high peptide identification rates, individualized p.p.b.-range mass accuracies and proteome-wide protein quantification. Nat. Biotechnol. 26, 1367–1372. https://doi.org/10.1038/nbt.1511.

123. Cox, J., Neuhauser, N., Michalski, A., Scheltema, R.A., Olsen, J.V., and Mann, M. (2011). Andromeda: a peptide search engine integrated into the MaxQuant environment. J. Proteome Res. 10, 1794–1805. https://doi.org/10.1021/pr101065j.

124. Huang, T., Choi, M., Tzouros, M., Golling, S., Pandya, N.J., Banfai, B., Dunkley, T., and Vitek, O. (2020). MSstatsTMT: Statistical Detection of Differentially Abundant Proteins in Experiments with Isobaric Labeling and Multiple Mixtures. Mol. Cell. Proteomics MCP 19, 1706–1723. https://doi.org/10.1074/mcp.RA120.002105.

125. Tyanova, S., Temu, T., Sinitcyn, P., Carlson, A., Hein, M.Y., Geiger, T., Mann, M., and Cox, J. (2016). The Perseus computational platform for comprehensive analysis of (prote)omics data. Nat. Methods 13, 731–740. https://doi.org/10.1038/nmeth.3901.

126. Corsello, S.M., Nagari, R.T., Spangler, R.D., Rossen, J., Kocak, M., Bryan, J.G., Humeidi, R., Peck, D., Wu, X., Tang, A.A., et al. (2020). Discovering the anti-cancer potential of non-oncology drugs by systematic viability profiling. Nat. Cancer 1, 235–248. https://doi.org/10.1038/s43018-019-0018-6.

127. Garnett, M.J., Edelman, E.J., Heidorn, S.J., Greenman, C.D., Dastur, A., Lau, K.W., Greninger, P., Thompson, I.R., Luo, X., Soares, J., et al. (2012). Systematic identification of genomic markers of drug sensitivity in cancer cells. Nature 483, 570–575. https://doi.org/10.1038/nature11005.

128. Seashore-Ludlow, B., Rees, M.G., Cheah, J.H., Cokol, M., Price, E.V., Coletti, M.E., Jones, V., Bodycombe, N.E., Soule, C.K., Gould, J., et al. (2015). Harnessing Connectivity in a Large-Scale Small-Molecule Sensitivity Dataset. Cancer Discov. 5, 1210–1223. https://doi.org/10.1158/2159-8290.CD-15-0235.

129. Martin, M. (2011). Cutadapt removes adapter sequences from high-throughput sequencing reads. EMBnet.journal 17, 10–12. https://doi.org/10.14806/ej.17.1.200.

130. Li, W., Xu, H., Xiao, T., Cong, L., Love, M.I., Zhang, F., Irizarry, R.A., Liu, J.S., Brown, M., and Liu, X.S. (2014). MAGeCK enables robust identification of essential genes from genome-scale CRISPR/Cas9 knockout screens. Genome Biol. 15, 554. https://doi.org/10.1186/s13059-014-0554-4.

131. Tyler, M., Gavish, A., Barbolin, C., Tschernichovsky, R., Hoefflin, R., Mints, M., Puram, S.V., and Tirosh, I. (2024). The Curated Cancer Cell Atlas: comprehensive characterisation of tumours at single-cell resolution. Preprint at bioRxiv, https://doi.org/10.1101/2024.10.11.617836 https://doi.org/10.1101/2024.10.11.617836.

132. Pelka, K., Hofree, M., Chen, J.H., Sarkizova, S., Pirl, J.D., Jorgji, V., Bejnood, A., Dionne, D., Ge, W.H., Xu, K.H., et al. (2021). Spatially organized multicellular immune hubs in human colorectal cancer. Cell 184, 4734-4752.e20. https://doi.org/10.1016/j.cell.2021.08.003.

133. Hao, Y., Hao, S., Andersen-Nissen, E., Mauck, W.M., Zheng, S., Butler, A., Lee, M.J., Wilk, A.J., Darby, C., Zager, M., et al. (2021). Integrated analysis of multimodal single-cell data. Cell 184, 3573-3587.e29. https://doi.org/10.1016/j.cell.2021.04.048.

134. Hafemeister, C., and Satija, R. (2019). Normalization and variance stabilization of single-cell RNA-seq data using regularized negative binomial regression. Genome Biol. 20, 296. https://doi.org/10.1186/s13059-019-1874-1.

135. Korsunsky, I., Millard, N., Fan, J., Slowikowski, K., Zhang, F., Wei, K., Baglaenko, Y., Brenner, M., Loh, P.-R., and Raychaudhuri, S. (2019). Fast, sensitive and accurate integration of single-cell data with Harmony. Nat. Methods 16, 1289–1296. https://doi.org/10.1038/s41592-019-0619-0.

Acknowledgments

We express our thanks to all the members of the Davoli lab and Cell Biology Program of NYU Grossman School of Medicine for their discussions, help and support. We also thank Dr. Susan Smith, Dr. Eva Hernando, Dr. Richard L. Possemato, Dr. Evgeny A. Nudler, Dr. David Fenyö, and other colleagues at NYU Grossman School of Medicine for helpful comments and insights during the completion of the project. We are grateful to Dr. Liam Holt (NYU Grossman School of Medicine) for providing RPE1 and hPNE cells, and Dr. Jason Sheltzer (Yale University School of Medicine) and Dr. Zuzana Storchová (TU Kaiserslautern) for the aneuploid clones generated using MMCT and their near-diploid controls. We thank Alcida Karz (NYU Grossman School of Medicine) for providing the control shRNA and Dr. Eli Rothenberg for providing the PARP1 template plasmid. We thank NYU Grossman School of Medicine's Genome Technology Center and Proteomics Laboratory for help with experiments. We appreciate data accessibility provided by TCGA Research Network (https://www.cancer.gov/tcga), Human Protein Atlas (proteinatlas.org), Depmap portal (depmap.org) and Gene Expression Omnibus (https://www.ncbi.nlm.nih.gov/geo/). This research was supported by grants from the Cancer Research UK Grand Challenge, the Mark Foundation for Cancer Research (C5470/A27144), NIH R37 R37CA248631, R01 R01HG012590, R01 R01DK135089, the MRA Young Investigator Award, the Breast Cancer Alliance Young Investigator Award and a NFCR (National Foundation for Cancer Research) collaborative grant to Dr. Teresa Davoli, and by the Cancer Center Support Grant P30CA016087 at the Laura and Isaac Perlmutter Cancer Center to NYU Langone's Genome Technology Center (RRID:SCR_017929) and Proteomics Laboratory (RRID:SCR_017926). Biorender was used for some panels in Figures 1, S1, 5, 6 and S6.

List of Supplementary Materials

Supplementary Materials:

Figs. S1 to S6
Tables S1 and S6

Main Figures

Figure 1

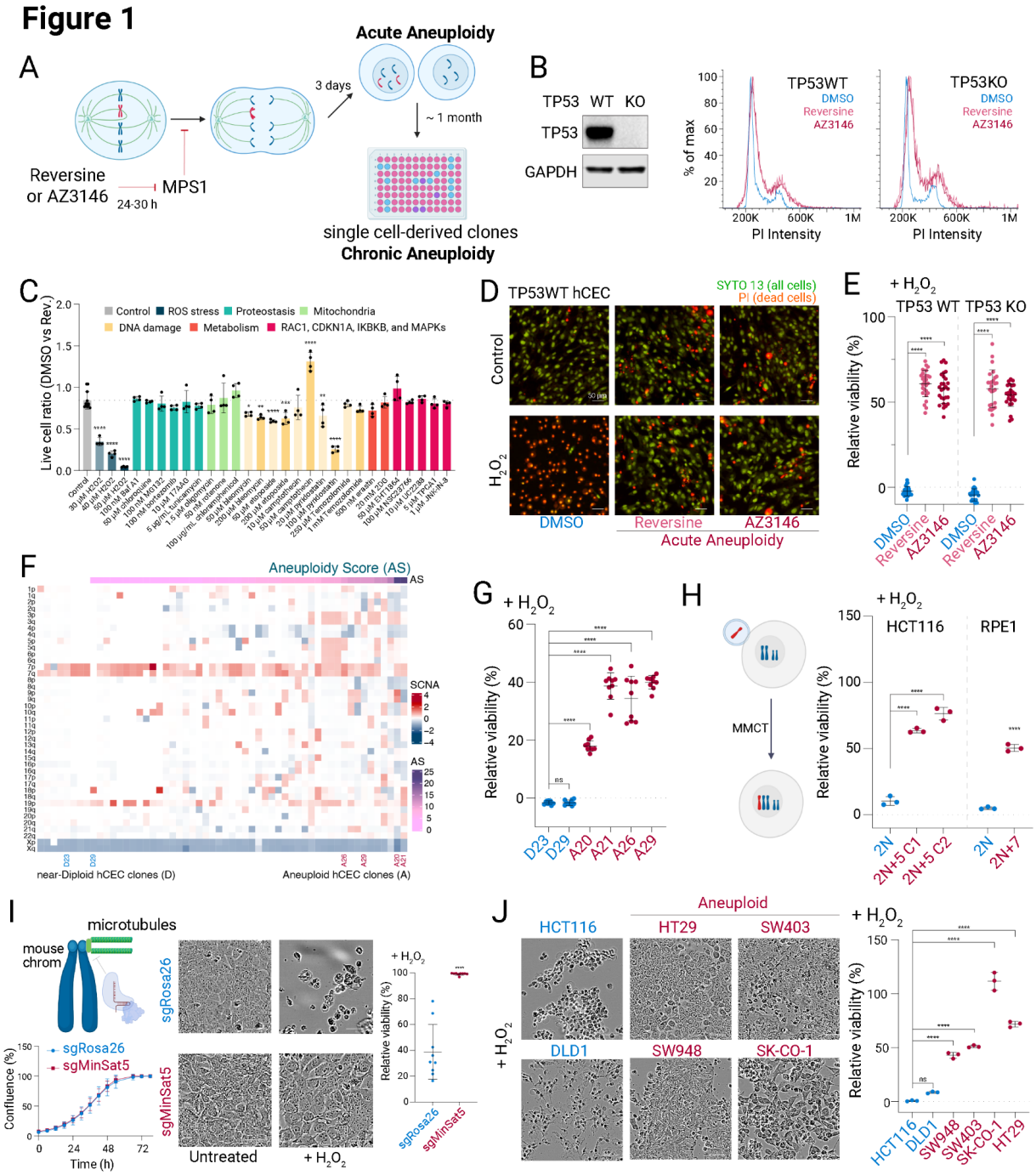

Figure 1. Aneuploidy renders cells resistant to oxidative stress, independent of TP53 status, altered chromosomes, or cell lineage

(**A**) Generation of acute and chronic aneuploidy models via transient MPS1 inhibition and subsequent single-cell clone expansion, respectively. (**B**) Comparison of DNA content in diploid and aneuploid hCECs with wild-type TP53 or TP53 knockout. Western blot shows TP53 status (left); flow cytometry histograms of propidium iodide (PI) staining after 24-30h MPS1 inhibitor treatment (0.5 μM reversine or 5 μM AZ3146) and 3-day release (right). (**C**) Viability of diploid (DMSO, labeled with GFP) and aneuploid (reversine, unlabeled) TP53WT hCECs exposed to various stressors for 24h. Data show mean ± SD (n=4). One-way ANOVA with Dunnett's test. (**D**) Representative fluorescent images of diploid (DMSO) and aneuploid (reversine or AZ3146) TP53WT hCECs after H_2O_2 treatment (75 μM, 24h). Green: SYTO 13 (all cells); red: PI (dead cells). (**E**) Viability of diploid (DMSO) and aneuploid (reversine or AZ3146) hCECs after H_2O_2 treatment (75 μM, 24h). Data shown mean ± SD of 9 fields/replicate, n=3 replicates from representative experiment of >3. One-way ANOVA with Dunnett's test. (**F**) Heatmap of arm-level somatic copy number alterations (SCNA) in TP53KO hCEC clones. D: near-diploid clones, A: aneuploid clones. (**G**) Viability of near-diploid and aneuploid hCEC clones after H_2O_2 treatment (50 μM H_2O_2 for 1h + 24h release, brief H_2O_2 exposure used to control for cell cycle differences). Mean ± SD of 9 fields from representative experiment of >3. One-way ANOVA with Tukey's test. (**H**) Viability of MMCT-generated near-diploid and aneuploid HCT116 or RPE1 clones with H_2O_2 treatment (4mM and 100 μM, respectively, 24h). Mean ± SD from triplicates, representative of ≥2 experiments. One-way ANOVA with Dunnett's test (HCT116) or unpaired t-test (RPE1). (**I**) Aneuploid mouse KP lung cancer cells were generated by the KaryoCreate method. Proliferation curves of aneuploid KP cells (sgMinSat5) and diploid control cells (sgRosa26), Mean ± SD (bottom left panel). Representative images of diploid and aneuploid KP cells with H_2O_2 treatment (2 mM, 24h) (middle panel). Viability of diploid and aneuploid KP cells after H_2O_2 treatment (2 mM, 24h). Mean ± SD of 9 fields, representative of >3 experiments. Unpaired t-test (right panel). (**J**) Representative images and viability quantification of near-diploid (HCT116 and DLD1) and high-aneuploidy (HT29, SW403, SW948 and SK-CO-1) colon cancer cells with H_2O_2 treatment (4 mM, 24 h). Mean ± SD from triplicates, representative of >3 experiments. One-way ANOVA with Tukey's test (right panel). ns, $p>0.05$; *$p<0.05$; **$p<0.01$; ***$p<0.001$; ****$p<0.0001$. Scale bar, 50 μm.

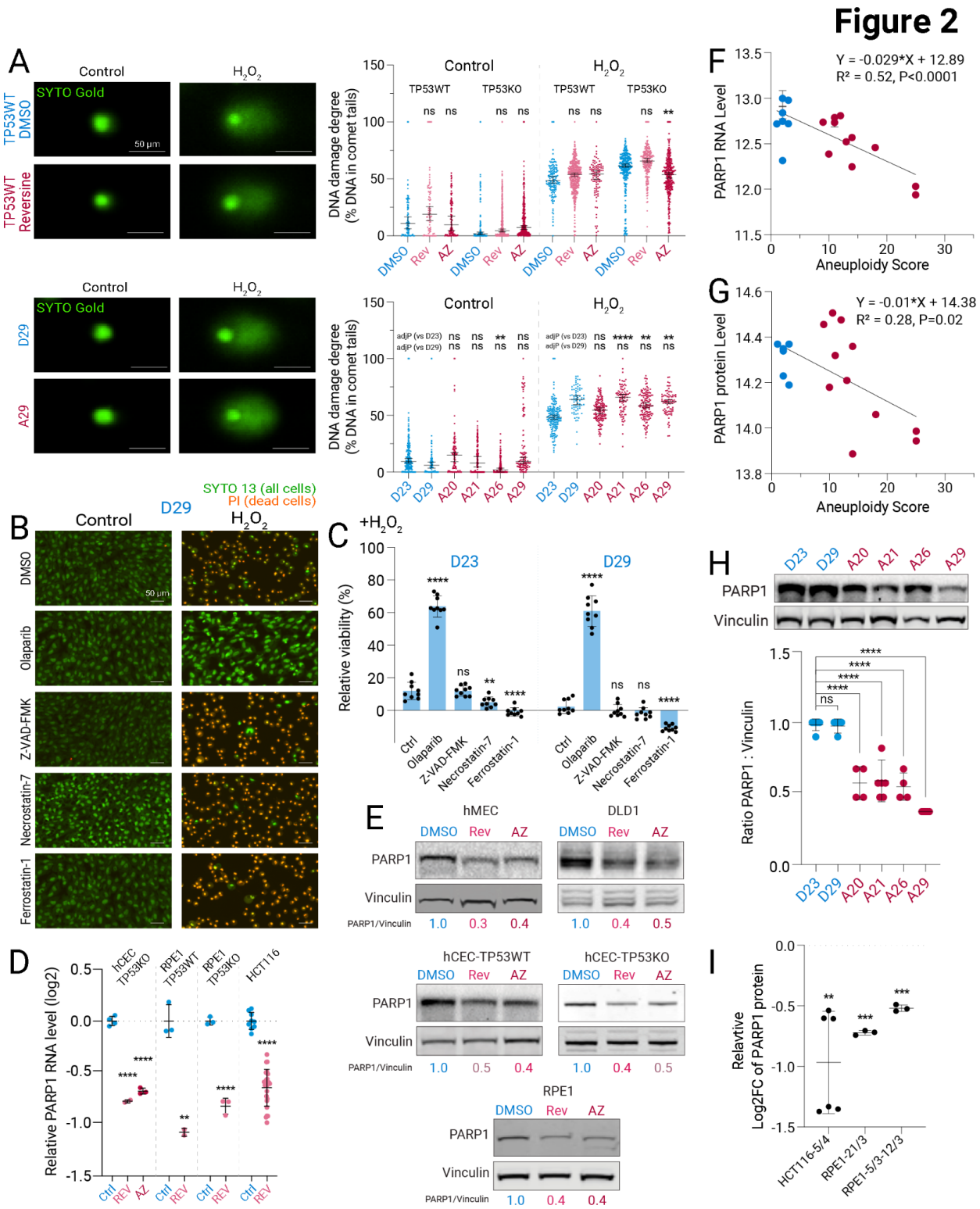

Figure 2. PARP1, which is required for ROS-induced cell death, is suppressed in aneuploid cells

(**A**) DNA damage assessment by alkaline comet assay in diploid and aneuploid hCECs with H_2O_2 treatment (50 µM, 1h). Left: representative images of SYTO Gold-stained DNA. Right: quantification

2231 of relative DNA content in comet tails. Medians with 95% CI from representative experiment of ≥2.
2232 Kruskal-Wallis one-way ANOVA with Dunnett's test. (**B**) Representative fluorescent images of
2233 diploid hCECs (D29) with H_2O_2 treatment (50 μM, 1h) in the presence of cell death inhibitors (pre-
2234 treated for 2h and post-treated for 24h). (**C**) Viability of the near-diploid hCEC clones under
2235 conditions described in (B). Mean ± SD of 9 fields from representative experiment of ≥2. One-way
2236 ANOVA with Dunnett's test. (**D**) Relative RNA levels of PARP1 (Log2) between aneuploid (reversine
2237 or AZ3146) and diploid (DMSO) hCEC, RPE1, TP53KO RPE1, and HCT116 cells. Mean ± SD, n=2-24.
2238 One-way ANOVA with Dunnett's test (hCEC); unpaired t-test (RPE1, TP53KO RPE1, and HCT116).
2239 (**E**) Representative western blot of PARP1 protein levels in diploid (DMSO) and aneuploid (reversine
2240 or AZ3146) cells. (**F-G**) Correlation between aneuploidy degree and PARP1 RNA (F) or protein levels
2241 (G) in hCEC clones. Linear regression is included to fit the data. (**H**) PARP1 protein levels in hCEC
2242 clones. Top: representative western blot. bottom: quantification of PARP1 protein level normalized
2243 to Vinculin protein level. Mean ± SD, n≥2. One-way ANOVA with Tukey's test. (**I**) Relative PARP1
2244 protein levels between aneuploid clones and their diploid controls in HCT116 and RPE1 cells using
2245 data from Stingele et al., 2012. Mean ± SD, n=3-6. One sample t-test against zero. HCT116-5/4 (four
2246 copies of chromosome 5), RPE1-21/3 (three copies of chromosome 21), RPE1-5/3-12/3 (three
2247 copies of chromosome 5 and 12). ns, $p>0.05$; *$p<0.05$; **$p<0.01$; ***$p<0.001$; ****$p<0.0001$. Scale
2248 bar, 50 μm.

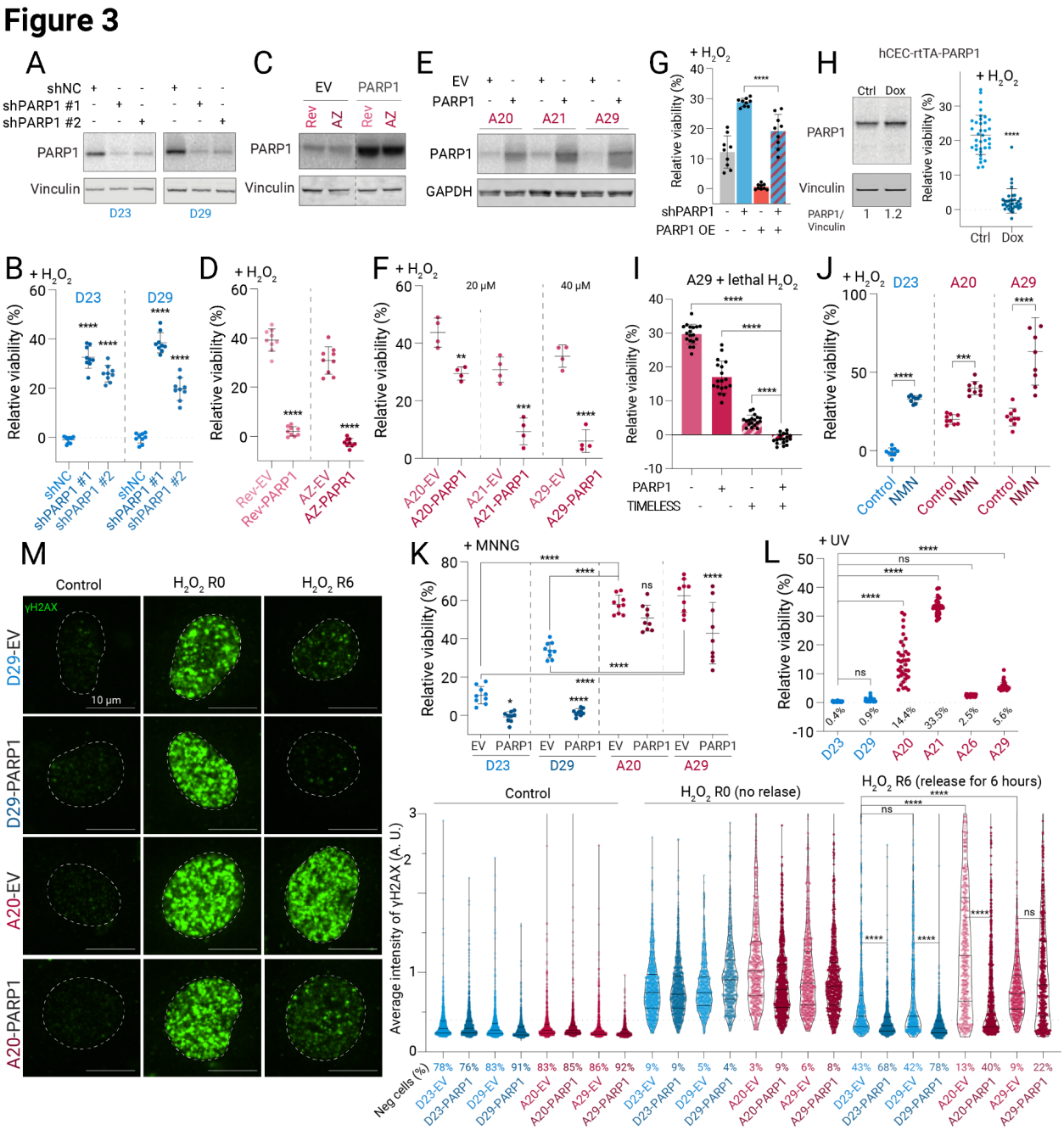

Figure 3. Cell death and DNA repair mediated by PARP1 are suppressed in aneuploid cells by PARP1 downregulation

(**A**) Representative western blot of PARP1 protein levels in near-diploid hCEC clones expressing control (shNC) or PARP1-targeting shRNAs. (**B**) Viability of near-diploid hCECs with PARP1 knockdown after H_2O_2 treatment. Mean ± SD of 9 fields from representative experiment of ≥2. One-way ANOVA with Dunnett's test. (**C**) Representative western blot of PARP1 protein levels in the acute aneuploidy hCEC model (TP53WT) with PARP1 overexpression. (**D**) Viability of the acutely aneuploid hCECs (TP53WT) with PARP1 overexpression after H_2O_2 treatment. Mean ± SD of 9 fields. Unpaired t-test. (**E**) Representative western blot of PARP1 protein levels in aneuploid hCEC

2259 clones with PARP1 overexpression. (**F**) Viability of control (empty vector) and PARP1-
2260 overexpressing aneuploid hCEC clones after H_2O_2 treatment. Mean ± SD of 4 fields from
2261 representative experiment of ≥2. Unpaired t-test. (**G**) Viability after H_2O_2 treatment with PARP1
2262 knockdown (3'UTR-targeted), PARP1 overexpression (shRNA-resistant cDNA), or both. Mean ± SD
2263 of 9 fields from representative experiment of ≥2. One-way ANOVA with Tukey's test. (**H**) Western
2264 blot of PARP1 protein expression (left) and quantification of H_2O_2-induced cell viability changes
2265 (right) in hCECs with doxycycline-inducible PARP1 overexpression. Mean ± SD from 9
2266 fields/replicate, n=4 replicates from representative experiment. Unpaired t-test. (**I**) Viability after
2267 H_2O_2 treatment (40 μM) with PARP1 overexpression, TIMELESS overexpression, or both. Mean ±
2268 SD from 9 fields/replicate, n=2 replicates from representative experiment. One-way ANOVA with
2269 Tukey's test. (**J**) Viability after H_2O_2 treatment in hCEC clones with NMN pretreatment (180 μM,
2270 24h). Mean ± SD of 9 fields from representative experiment of ≥2. One-way ANOVA withTukey's
2271 test. (**K**) Viability after MNNG treatment (62.5 μM, 24 hours) in near-diploid and aneuploid hCEC
2272 clones with control or PARP1 overexpression. Mean ± SD of 9 fields from representative experiment
2273 of ≥2. One-way ANOVA with Tukey's test. (**L**) Viability after UV treatment (50 J/m^2 + 5-day release)
2274 in near-diploid and aneuploid hCEC clones. Mean ± SD of 36 fields from representative experiment
2275 of ≥2. One-way ANOVA with Tukey's test. Average viability is indicated below the dashed line. (**M**)
2276 The dynamics of DNA damage degree (indicated by γH2AX intensity) before and after H_2O_2
2277 exposure (50 μM, 1h) in near-diploid (blue) and aneuploid (red) hCEC clones, with or without PARP1
2278 overexpression. Left: representative fluorescent images of γH2AX (scale bar, 10 μm). Right: violin
2279 plots showing median and quartiles of γH2AX intensity (>460 cells/condition). R0/R6: 0 or 6h post
2280 H_2O_2 exposure. Kruskal-Wallis one-way ANOVA with Dunnett's test. For clarity the p-values of all
2281 comparisons are included in Table 3. γH2AX-negative threshold set at ~80% for untreated clones;
2282 percentages shown below X-axis. ns, $p>0.05$; *$p<0.05$; **$p<0.01$; ***$p<0.001$; ****$p<0.0001$.

Figure 4

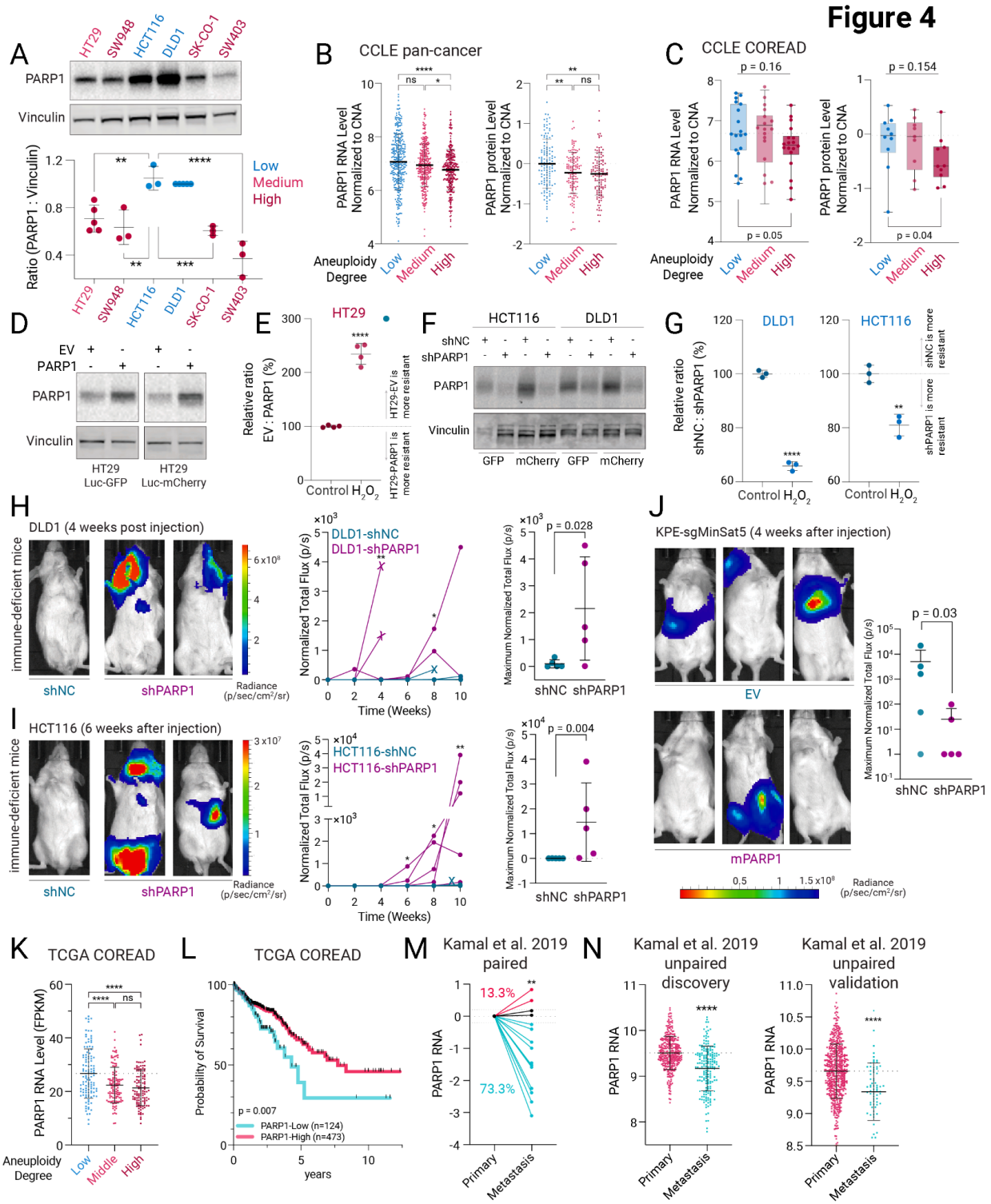

2283

Figure 4. PARP1 suppression promotes metastasis of aneuploid colorectal cancer cells

(**A**) Western blot of PARP1 protein levels in near-diploid (HCT116 and DLD1, blue) and high-aneuploidy (HT29, SW948, SW403, and SK-CO-1, red) colon cancer cell lines. n≥3, mean±SD, One-way ANOVA with Tukey's test. (**B**) SCNA-normalized PARP1 RNA levels (left, n=942) and protein levels (right, n=365) in pan-cancer cell lines with different aneuploidy degrees. Mean ± SD. One-way ANOVA with Tukey's test. (**C**) SCNA-normalized PARP1 RNA levels (left, n=54) and protein levels (right, n=29) in colon cancer cell lines with different aneuploidy degrees. Boxplots show median with first/third quartiles. Kruskal-Wallis test, followed by one-tailed t-test comparing low vs high aneuploidy groups. (**D**) PARP1 protein levels in high-aneuploidy HT29 cells with and without PARP1 overexpression. (**E**) Relative viability of HT29-mCherry-EV to HT29-GFP-PARP1 when co-cultured together, with and without 2 mM H_2O_2 treatment for 24 hours. Mean ± SD of 4 replicates from representative experiment of ≥2. Unpaired t-test. (**F**) PARP1 protein levels in near-diploid HCT116 and DLD1 cells with and without PARP1 knockdown. (**G**) The relative cell number ratio of DLD1-mCherry-shNC (or HCT116-mCherry-shNC) to DLD1-GFP-shPARP1 (or HCT116-GFP-shPARP1) when co-cultured together, with and without 2 mM H_2O_2 treatment for 24 hours. Mean ± SD of 4 replicates from representative experiment of ≥2. Unpaired t-test. (**H-I**) Left: representative bioluminescence images (BLI) of NSG mice with near-diploid DLD1 or HCT116 expressing control or PARP1 shRNA. Quantification of the total flux signal over time (middle) and maximum values (right) (n=5 mice/group). Mean ± SD. Two-tailed Mann-Whitney test. Crosses indicate endpoints. (**J**) Left: representative BLI of immune-intact mice (B6 Albino mice) with aneuploid mouse KP lung cancer cells (transduced with sgMinSat5) overexpressing empty or PARP1 cDNA. Right: quantification of the maximum total flux signal (n=5 mice/group). Mean + SD. One-tailed Mann-Whitney test. (**K**) PARP1 RNA levels in TCGA COREAD patients without PARP1 SCNA (absolute SCNA value < 0.05). n=352. Mean ± SD. One-way ANOVA with Tukey's test. (**L**) Kaplan-Meier survival analysis of TCGA COREAD patients stratified by PARP1 expression. Log-rank (Mantel-Cox) test. PARP1 expression threshold was optimized for statistical significance. (**M**) PARP1 RNA levels in primary COREAD tumors and their paired metastases (n=15 patients, GSE131418). One Sample Wilcoxon signed-rank test. (**N**) PARP1 RNA levels in unpaired primary tumors versus metastases of COREAD patients: discovery cohort (MCC dataset with 333 primary tumors and 184 metastases) and validation cohort (Consortium dataset with 545 primary tumors and 72 metastases) from GSE131418. Mean ± SD. Unpaired t-test. ns, p>0.05; *p<0.05; **p<0.01; ***p<0.001; ****p<0.0001.

Figure 5

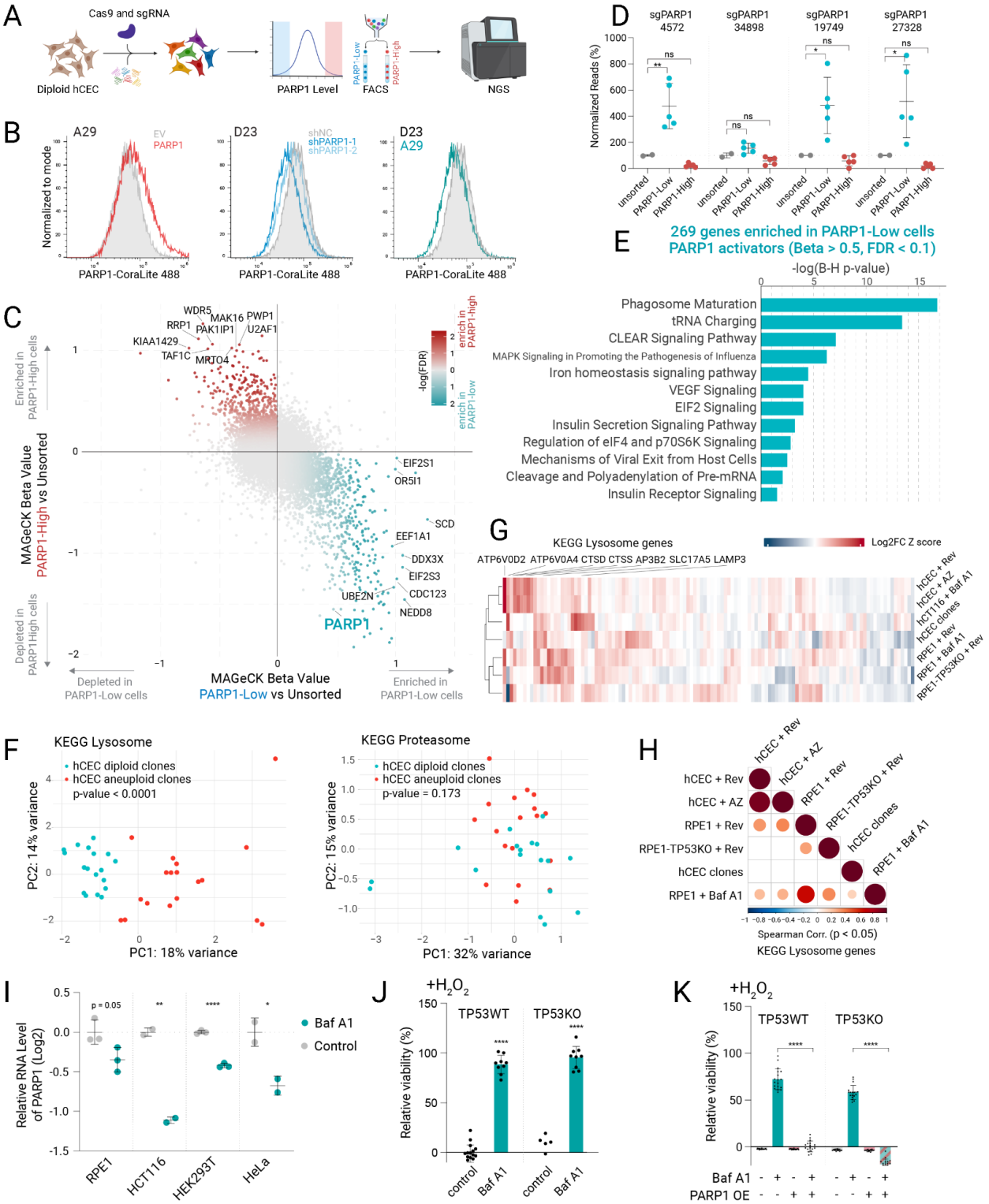

Figure 5. Genome-wide CRISPR screen reveals lysosomal stress as a mediator of PARP1 downregulation in aneuploid cells

(**A**) Workflow of FACS-based whole-genome CRISPR screen to identify regulators of PARP1 expression. (**B**) Validation of PARP1 antibody sensitivity and specificity using flow cytometry with intracellular staining in hCECs with PARP1 overexpression (left) and PARP1 knockdown (middle), and representative near-diploid versus aneuploid hCEC clones (right). (**C**) The enrichment and depletion of sgRNAs in sorted PARP1-low and PARP1-high samples compared to unsorted samples. Positive and negative MAGeCK beta values indicate enrichment and depletion, respectively. (**D**) Normalized sgPARP1 read counts in sorted PARP1-low and PARP1-high samples compared to unsorted samples. Mean ± SD. One-way ANOVA with Dunnetts' test. (**E**) Pathway analysis of 269 PARP1 activators identified by CRISPR screen (enriched in PARP1-low cells, beta value > 0.5 and FDR < 0.1). Pathways with adjusted p-values < 0.1 are shown. (**F**) Principal component analysis (PCA) of lysosomal (left) and proteasomal (right) gene expression in near-diploid (blue) and aneuploid (red) hCEC clones. Statistical significance of group separation was assessed by permutation test (n=10,000) using Euclidean distances in PC1-PC2 space. (**G**) Heatmap showing log2FC z-score of KEGG lysosomal genes in aneuploid cells and Bafilomycin A1 (Baf A1)-treated cells. (**H**) Spearman correlation of lysosomal gene expression changes in aneuploid cells and Baf A1-treated RPE1 cells. Circle color intensity represents correlation coefficient strength ($p < 0.05$ shown). (**I**) PARP1 mRNA levels (Log2) in Baf A1-treated cells and their controls. Mean ± SD. Unpaired t-test. (**J**) Viability of hCECs pre-treated with Baf A1 (5 nM, 24h) followed by H_2O_2 treatment (200 μM, 24 h). Mean ± SD of 9 fields from representative experiment of ≥2. Unpaired t-test. (**K**) Viability after H_2O_2 treatment in hCECs with or without Baf A1 pre-treatment or PARP1 overexpression. Mean ± SD of 9 fields from representative experiment of ≥2. One-way ANOVA with Tukey's test. ns, $p>0.05$; *$p<0.05$; **$p<0.01$; ***$p<0.001$;****$p<0.0001$.

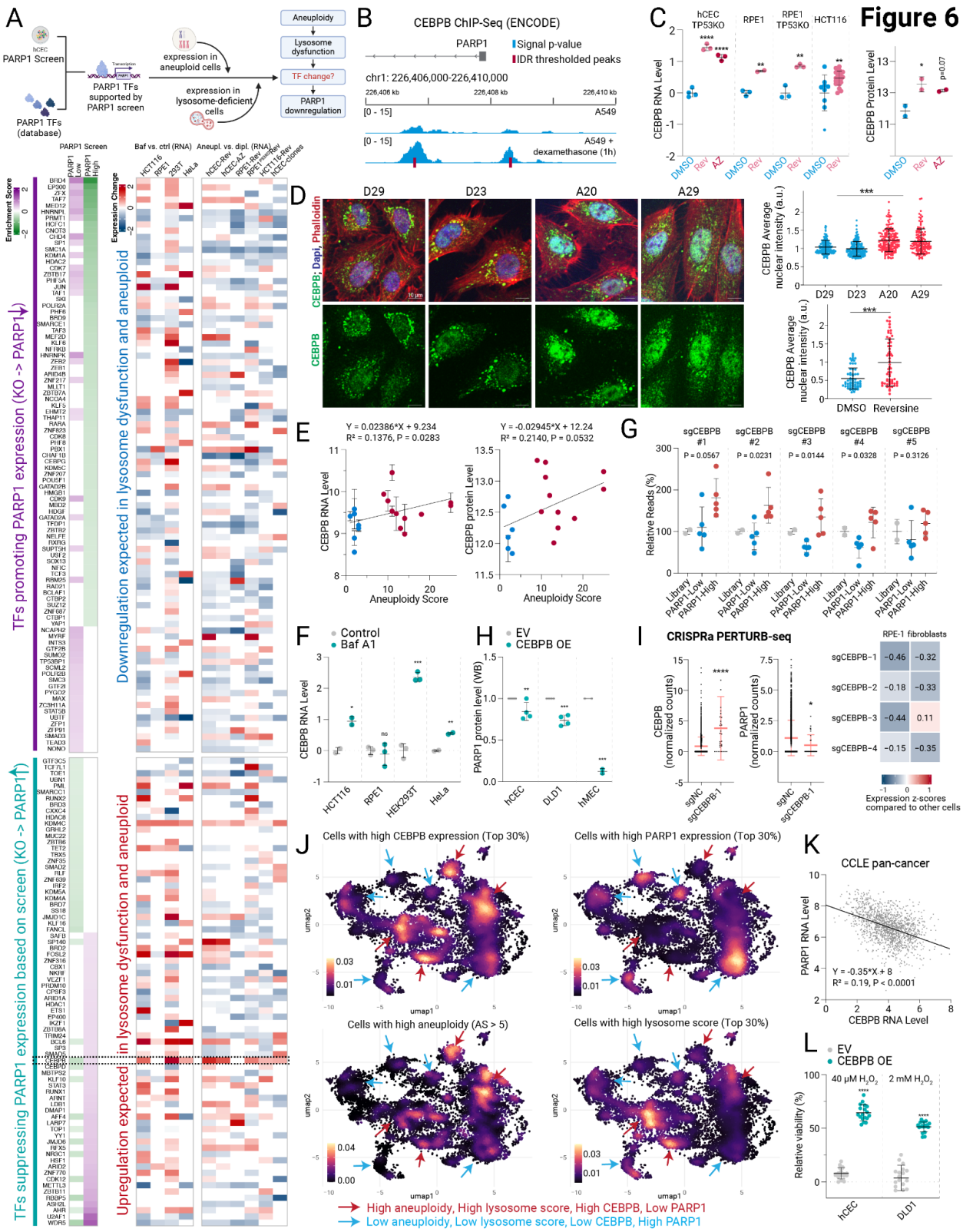

Figure 6. Aneuploidy-activated CEBPB transcription factor suppresses PARP1

(**A**) Transcription factors (TFs) regulating PARP1 expression. Top: Strategy to identify transcription factors (TFs) regulating PARP1 expression in aneuploid cells, which integrates PARP1 CRISPR screen results, TF databases, and expression profiles of aneuploid and lysosome-deficient cells. Bottom: Heatmap showing PARP1-promoting TFs (enriched in PARP1-low samples or depleted in PARP1-high samples) and PARP1-suppressing TFs (enriched in PARP1-high samples or depleted in PARP1-low samples), along with expression changes of these TFs across lysosome-deficient and aneuploid models. Purple/green: enriched/depleted in CRISPR screen, red/blue: upregulation/downregulation. $p<0.05$. (**B**) CEBPB ChIP-Seq data (ENCODE) showing binding near the PARP1 transcription start site. Top: genomic location; bottom: ChIP-Seq signal p-value (blue) and IDR thresholded peaks (red). (**C**) CEBPB RNA and protein levels in acute aneuploidy models. Mean ± SD. n=2-24. One-way ANOVA with Dunnett's test (hCEC) or unpaired t-test (RPE1, RPE1-TP53KO and HCT116). (**D**) Nuclear CEBPB signal in hCECs with acute and chronic aneuploidy. Left: representative immunofluorescence images of CEBPB (green), Phalloidin (red), and DAPI (blue) staining in near-diploid (D23, D29) and aneuploid (A20, A29) hCECs (scale bar, 10 μm). Right: quantification of nuclear CEBPB in near-diploid and aneuploid hCECs using the acute and chronic model. Mean ± SD, n>50 cells per condition. P-value from Two-tailed Mann-Whitney test comparing aneuploid and near-diploid cells. (**E**) CEBPB RNA (left) and protein (right) correlation with aneuploidy score in chronic aneuploid clones. Linear regression is included to fit the data. (**F**) CEBPB RNA levels in control versus Baf A1-treated cells. Mean ± SD, n= 2-3; unpaired t-test. (**G**) Normalized sgCEBPB read counts in sorted PARP1-low and PARP1-high samples compared with unsorted samples. Mean ± SD. One-way ANOVA. (**H**) PARP1 protein levels after CEBPB overexpression (OE) versus empty vector (EV) by Western Blot. Mean ± SD, n= 2-4; unpaired t-test. (**I**) CRISPR activation (CRISPRa) Perturb-Seq analysis of PARP1 regulation by CEBPB. (Left) Normalized read counts of CEBPB and PARP1 in cells with CEBPB CRISPRa using sgCEBPB-1 compared to control cells with non-targeting sgRNAs (sgNC). Mean ± SD. unpaired t-test. (Right) Heatmap showing expression z-scores of PARP1 in RPE-1 cells and Hs27 fibroblast cells following CEBPB activation across four different sgRNAs. (**J**) Single-cell RNA-seq analysis of malignant colorectal cancer cells. UMAP plots displaying cell density for cells with top 30% of CEBPB expression (upper left), top 30% of PARP1 expression (upper right), aneuploidy score >5 (lower left), and top 30% of KEGG lysosome signature score (lower right). Cell density is weighted by the respective scores. Cell populations with high CEBPB expression, high aneuploidy, and high lysosomal activity (red arrows) overlap but are distinct from populations with high PARP1 expression (blue arrows). (**K**) CEBPB and PARP1 RNA level correlation in pan-cancer cell lines (CCLE dataset). Linear regression is included to fit the data. (**L**) Viability after H_2O_2 treatment in CEBPB-OE versus EV cells (40 μM for TP53-KO hCEC, 2 mM for DLD1, 24h). Mean ± SD from 9 fields/replicate, n=2 replicates from representative experiment of ≥3. Unpaired t-test. ns, $p>0.05$; *$p<0.05$; **$p<0.01$; ***$p<0.001$; ****$p<0.0001$.